Characterization of Snow-Pack Properties on Mt. Rainier, WA
With Multi-Spectral Remote-Sensing Data

Estimation of Water Temperature From Airborne and Satellite
Thermal-Infrared (TIR) Remote-Sensing Data

Jennifer Elizabeth Kay

A thesis submitted in partial fulfillment of the requirements for the degree of

Master of Science

University of Washington

2002

Program Authorized to Offer Degree: Geological Sciences

University of Washington
Graduate School

This is to certify that I have examined this copy of a master's thesis by

Jennifer Elizabeth Kay

and have found that it is complete and satisfactory in all respects,
and that any and all revisions required by the final
examining committee have been made.

Committee Members:

Alan Gillespie

Stephen Warren

Stephen Burges

Date: 6/3/02

TABLE OF CONTENTS

LIST OF FIGURES

LIST OF FIGURES CONTINUED

LIST OF FIGURES CONTINUED

LIST OF FIGURES CONTINUED

LIST OF TABLES

Acknowledgements

Thanks to Alan Gillespie, Steve Warren and Steve Burges for guidance, support, and patience as my advisors; to the EPA Science to Achieve Results (STAR) Program (Grant R827675-01-0) for funding my research and the MASTER over flights; to Gary Hansen for assistance with DISORT and helpful comments; to Rebecca Handcock for input and support; to Anne Nolin for helpful suggestions on the Mt. Rainier analysis; to Alison Anders, Meg Smith, and Chris Fuller for ground-truth assistance at Mt. Rainier; to Bill Gustafson for technical assistance; to Nir Naveh and Keith Cherkauer for input and ground-truth data; to Don Sabol for helping acquire the FLIR data; to Rob Elleman and UW Atmospheric Sciences for MM5 output; to Gail Anderson for assistance with MODTRAN; to Tom Grenfell for lending me the Kipp Radiometer; and to Amit Mushkin, Christine Woodward, Amy Gaffney, Heidi Guetschow, Hans Schwaiger, Rob Elleman, Sarah Albano, Paul Bedrosian, and Meg Smith for being supportive friends.

Dedication

To my parents, Robert and Suzanne Kay, for their encouragement and love

Chapter I. Characterization of Snow-Pack Properties on Mt. Rainier, WA With Multi-Spectral Remote-Sensing Data

ABSTRACT:

Relating cryosphere change to climate change requires estimation of radiative fluxes on snow-covered surfaces. The distribution of, and relationship between, snow-pack properties that affect radiative balance can be estimated with high-resolution remote-sensing data. MODIS/ASTER airborne simulator (MASTER) data were collected at Mt. Rainier to reveal spatial patterns of, and correlations between, snow contaminant content, grain size, and temperature. The visible and near-infrared (VNIR: 11 bands, 0.4-1.0 μm) and the short-wave infrared (SWIR: 14 bands, 1.6-2.4 μm) data are processed to bi-directional reflectance (BDR) and albedo, by removing atmospheric effects and by normalizing to Solar irradiance and incidence angle. VNIR BDR and albedo are used as a proxy for snow contaminant content. Physical and optical grain size are estimated by comparing SWIR BDR and albedo to modeled and measured spectra, and ground-truth measurements. The thermal infrared data (TIR: 10 bands, 8-13 μm) are processed to temperature by removing emissivity and atmospheric effects. In combination, the VNIR, SWIR, and TIR data reveal a distinct pattern of contaminants, grain size, and temperature related to a recent snowfall and the end-of-the-summer melting season. At lower elevations, the surface accumulation of dirty lag deposits resulted in snow with very low visible albedo (20-30%), large physical and optical grain radii (500-1500 μm, 200 μm), and temperatures near the melting point. At higher elevations, the recent snowfall left snow with low contaminant content, and a higher visible albedo (60-90%). However, a region near the summit with smaller physical and optical grain radii (400 μm, 100 μm), and temperatures below the melting point, is distinguished from a middle elevation region with grain sizes and temperatures similar to the lower region. Contaminants reduce VNIR albedo and significantly enhance absorption of incoming solar radiation. The spatial correlation between temperature and grain size supports the idea that rapid, destructive metamorphism occurs when snow

temperatures are at the melting point.

1. Motivation:

The global retreat of alpine glaciers (IPCC, 2001, p. 129), and a reduction in northern hemisphere snow-cover extent (Robinson, 1997), offer discernable evidence of climate warming, and have motivated global monitoring of snow and ice [e.g., GLIMS (http://wwwflag.wr.usgs.gov/GLIMS/glimshome.html), WGMS (http://www.geo.unizh.ch/wgms/)]. However, relating the response of the cryosphere to climate change requires a detailed understanding of radiative balance, and climatic variables such as temperature, precipitation, and cloud cover. While local surface energy balance parameters are best measured in the field, remotely sensed data and interpretations are important because they provide a link between detailed ground-based measurements, and the spatial monitoring of snow and ice. Relating satellite observations of cryosphere change to global climate change requires validation of remote interpretations with concurrent ground truth, and higher spatial and spectral resolution remote-sensing data. This study shows how high-resolution multi-spectral remote-sensing data coupled with ancillary ground, model and laboratory measurements, can robustly estimate and correlate surface energy balance parameters over Mt. Rainier.

2. Introduction:

More than 88 km^2 of permanent snow and ice cover Mt. Rainier, the tallest of the Cascade volcanoes (Figure 1). In the contiguous United States, Mt. Rainier's Emmons Glacier has the largest surface area (11.1 km^2) whereas the Carbon Glacier has the lowest terminus elevation (1,000 m), the longest extent (9.2 km) and the thickest ice (210 m). Spectral changes in Mt. Rainier's snow and ice can be used to monitor their extent, solid impurity content, granularity, temperature, and liquid content.

On August 26, 2001 at 14:30 PDT, MODIS/ASTER Airborne Simulator (MASTER) data (Hook et al., 2000) were collected over Mt. Rainier's extensive snow and ice system. MASTER's high spatial resolution (nadir pixel size ~10 m) and

broad spectral coverage (50 bands, 0.4-13 μm), make it an ideal sensor for recovering snow and glacier properties (Table 1). The visible and near-infrared data (VNIR: 11 bands, 0.4-1.0 μm) are used to examine surface impurity content, the short-wave infrared data (SWIR: 14 bands, 1.6-2.4 μm) are used to estimate snow grain size, and the thermal infrared data (TIR: 10 bands, 8-13 μm) are used to estimate skin temperature (Figure 2). Liquid water percentage was not estimated because accurate recovery requires high spectral resolution at 1.1 μm or microwave data (A. Nolin, personal communication, 2001). Remnants of a 3-day-old snowfall coupled with the late season timing of the over flights left an interesting distribution of contaminants, grain sizes, and temperatures. Although many researchers have estimated surface energy balance parameters with remote-sensing data, MASTER data provides an opportunity to test inversion techniques, and a new look at the spatial correlation between these variables at high spatial resolution. The following objectives were developed for the MASTER Mt. Rainier data:

1) Make quantitative estimates of solar (0.4-2.6 μm) bi-directional reflectance (BDR) and albedo, and skin radiant temperature with MASTER data and field measurements.

2) Estimate snow contaminant content and snow grain size by comparing MASTER BDR and albedo measurements to field measurements, discrete-ordinates radiative transfer model estimates of BDR and albedo [DISORT, (Stamnes et al., 1988)], and laboratory measurements of albedo (Salisbury et al., 1994).

3) Quantify the spatial relationships between contaminant content, grain size, and the thermal state of the snow pack and explain these relationships in the context of the recent snowfall and end of melt season.

3. Background:

At visible wavelengths (0.4-0.7 μm), ice weakly absorbs radiation; as a result, snow has a very high albedo (~90%). However, snow albedo at visible wavelengths is very sensitive to impurities (e.g., soot, dust, vegetation fragments). Models show that small highly absorbing particles in concentrations as low as 50 ppb can

decrease visible albedo (Warren and Wiscombe, 1980). Higuchi and Nagoshi (1975) measured a perennial snow patch to show that as particulate matter concentrations increased from 10^2 to 10^3-10^4 µg/ cm^3, albedo exponentially decreased from 60% to 20%. In general, the thickness of contaminant cover determines their effect on radiative balance. If contaminants are thin or distributed in the snow pack, they enhance melting by increasing the absorption of Solar radiation. However, if contaminants form a thick-enough layer [~2 mm for ash-covered glaciers (Driedger, 1981)], they serve to insulate the snow from solar irradiance and reduce the melting rate.

Whereas snow has a high albedo at visible wavelengths, an increase in the absorption coefficient of ice causes a steep drop-off of albedo in the NIR/SWIR (1.1 - 2.5□m) (Warren, 1984). Unlike visible wavelengths, ice itself is the dominant absorber and therefore contaminants have little effect on albedo (Warren and Wiscombe, 1980). Instead, a tradeoff between absorption by the ice and scattering at snow-grain surfaces determines albedo. Wiscombe and Warren (1980) used Mie theory and a radiative transfer model to demonstrate that the SWIR albedo of snow decreases as grain size increases. This grain size effect is especially prominent at 1.1, 1.3, 1.8, and 2.2 µm, corresponding to local minima in the absorption coefficient of ice.

Quantitative estimates of snow grain size for the near-surface snow layer have been made using SWIR remote-sensing data. Using AVIRIS data of Mammoth Mountain and DISORT, Nolin and Dozier (1993) related image-derived surface reflectance to snow grain size. Building on this work, Nolin and Dozier (2000) used DISORT to relate the area of the ice absorption feature at 1.03 µm to the optically equivalent effective snow grain size. This work demonstrated that with an atmospherically corrected, near-infrared image of surface reflectance and knowledge of the illumination and viewing geometries, quantitative estimates of grain size can be made.

Remote sensing in the TIR atmospheric window (8-14 µm) has been used to estimate temperatures in many settings (e. g., sea surface temperature). If the emissivity (ε) is known, the surface or skin temperature of an object can be estimated

using Planck's equation and a measurement of emitted thermal radiance (TIR). Modeled values of snow ε are above 99% (Dozier and Warren, 1982). Although variations in ε caused by density, liquid water, and grain size were unimportant, low angles of emission introduced errors as large as 3K. Measured snow reflectance data (Salisbury et al., 1994) [related to ε with Kirchhoff's law (ε =1-reflectivity)] show that snow reflectivity increases with increasing particle size and increased packing, and decreases with the presence of melt water. However, measured values show that ε was greater than 95% for all snow types examined. As snow is opaque at very small depths, the underlying surface does not contribute to the thermal emission. Thus, even for snow a few millimeters thick, TIR estimates of temperature will be for the top micrometers of the surface.

4. Data and Methods:

MASTER Data Processing:

Radiometric, geometric, and atmospheric corrections were applied to the raw MASTER data to obtain land-leaving radiance (L_g). The MASTER data were radiometrically calibrated to at-sensor radiance (L_s) by engineers at the NASA Airborne Simulator Facility. Visual inspection of data quality revealed several noisy bands (17, 25, 26, 27, and 34) that were excluded from further processing or analysis. Using 80 ground-control points, the L_s data were geometrically registered to a 10-m USGS DEM derived from 7.5' topographic maps (Figure 3). Although the RMS errors were relatively large (~5 pixels), these misfits were localized in regions of extreme topography, and large deviations from nadir (up to 40°). Atmospheric absorption, emission, and scattering were removed using MODerate resolution TRANsmission (MODTRAN) [(Ontar Corporation, 2001); (Anderson et al., 1998)] supplemented by radiosonde data taken in Enumclaw (20 km NW of Mt. Rainier) one hour after data acquisition. Logarithmic functions were fit to MODTRAN's predictions for variations in atmospheric transmissivity (τ) and path radiance (L_p) as a function of viewing geometry (0°, 20° and 40° deviation from nadir) and elevation (7 elevations

from Louise Lake at 1.4 km to the summit at 4.3 km) (Figure 4a&b, Appendix A). These regressions, along with the DEM and flight path geometry metadata, were interpolated, and applied as a pixel-by-pixel correction to L_s to obtain L_g (Equation 1).

$$L_g = \frac{L_s - L_p}{\tau} \quad (1)$$

where:

L_g = land-leaving radiance ($Wm^{-2}\mu m^{-1}sr^{-1}$)

L_s = sensor radiance ($Wm^{-2}\mu m^{-1}sr^{-1}$)

L_p = path radiance ($Wm^{-2}\mu m^{-1}sr^{-1}$)

τ = transmissivity (unit less)

After the data were processed to obtain L_g, bi-directional reflectance (BDR) and albedo were estimated for ten regions of interest (Figure 5). BDR was estimated by normalizing the L_g to the solar irradiance (S) predicted by MODTRAN, and the cosine of the incidence angle (Equation 2).

$$BDR = \frac{\left(L_g\right)}{S * \cos\theta_i} \quad (2)$$

where:

BDR = surface bi-directional reflectance (sr^{-1})

L_g = land-leaving radiance ($Wm^{-2}\mu m^{-1}sr^{-1}$)

S = Solar irradiance ($Wm^{-2}\mu m^{-1}$)

θ_i = incidence angle (^{o})

Albedo, the ratio of the flux reflected over the incident flux, can be found by integrating BDR over the entire hemisphere of viewing angles (Equation 3)

$$A = \int_0^{2\pi} \int_0^{\frac{\pi}{2}} BDR(\theta_i, \theta_v, \phi_i - \phi_v) \cos\theta_v \sin\theta_v d\theta_v d\phi_v \quad (3)$$

where:

A= surface albedo (unit less)

BDR = surface bi-directional reflectance (sr^{-1})

θ_V = viewing or emission zenith angle (º)

ϕ_V = viewing or emission azimuth angle (º)

As measurements of BDR for only one emission angle can be obtained from the MASTER data, albedo was calculated by assuming that BDR is independent of viewing angle (Equation 4).

$$A = BDR * \pi \quad (4)$$

where:

A = surface albedo (unit less)

BDR = surface bi-directional reflectance (sr^{-1})

Equation (4) is a good approximation when snow is fine-grained and illuminated from zenith. However, for large grains and large incidence angles, snow is strongly forward scattering (i.e., not diffuse or Lambertian) (Warren et al., 1998). Given this limitation, BDR and albedo were estimated in regions where incidence angles were less than 50º, and could be accurately predicted from the DEM (Figure 5).

We identified significant sources of measurement and calculation error and used a first moment approach for uncorrelated sources of error to investigate their impact on our estimations (Equation 5).

$$E(BDR) = E(L_s) * \frac{1}{\bar{\tau} * \bar{S} * \overline{\cos\theta_i}} + E(\tau) * \frac{\overline{L_s}}{\bar{S} * \overline{\cos\theta_i} * \bar{\tau}^2} + \ldots$$
$$E(S) * \frac{\overline{L_s}}{\bar{\tau} * \overline{\cos\theta_i} * \bar{S}^2} + E(\cos\theta_i) * \frac{\overline{L_s}}{\bar{\tau} * \overline{\cos\theta_i}^2 * \bar{S}} \quad (5)$$

where:

E(BDR) = estimated error in BDR (sr^{-1})

E(Ls) = estimated error in sensor radiance ($Wm^{-2}\mu m^{-1}sr^{-1}$)

$\overline{L_s}$ = average value of sensor radiance ($Wm^{-2}\mu m^{-1}sr^{-1}$)

$E(\tau)$ = estimated error in transmissivity (unit less)

$\bar{\tau}$ = average value of transmissivity (unit less)

E(S) = error in solar irradiance ($Wm^{-2}\mu m^{-1}$)

$\bar{S}$ = average value of solar irradiance ($Wm^{-2}\mu m^{-1}$)

$E(\cos\theta_i)$ = error in the cosine of the incidence angle (º)

$\overline{\cos\theta_i}$ = average value of the cosine of the incidence angle (º)

Measurement errors are limitations of the detector, while calculation errors result from inaccuracies in radiative transfer modeling. For MASTER, measurement errors are primarily schott noise in the detector. On the other hand, calculation error encompasses the radiometric calibration of detector DN, the estimation of τ, L_p and S with MODTRAN, and errors in the incidence angle derivation from inaccuracies in and poor registration with the DEM.

We estimated radiant temperature in the ten TIR bands using Planck's equation and the measured spectral ε of medium snow (Salisbury et al., 1994) (Equation 6).

$$T_k(x,\lambda) = \frac{c_2}{\lambda \ln\left[\frac{c_1 \varepsilon}{\pi \lambda^5 L_g(x,\lambda)} + 1\right]} \quad (6)$$

where

$c_1 = 3.74151*10^8$

$c_2 = 1.43879*10^4$

λ = band effective center wavelength (μm)

L_g = land-leaving radiance ($Wm^{-2}\mu m^{-1}sr^{-1}$)

MASTER Data Analysis:

In order to facilitate comparison, simple statistics were calculated to describe snow pack properties revealed by the MASTER data (Table 2). In the VNIR, the average albedo in bands 1-11 was used to approximate impurity content. In the SWIR, two proxies were calculated to represent grain size: a normalized difference ratio (NDR) between absorption peaks [b15 (1.78 μm), b23 (2.26 μm)] and troughs [b19 (1.98μm), b20 (2.08μm)] (Equation 7), and an absorption ratio (AR) representing the relative strength of exponential absorption in b15 and b23 versus b19 and b20 (Equation 8).

$$NDR = \frac{(b15 + b23) - (b19 + b20)}{(b15 + b23) + (b19 + b20)} \quad (7)$$

$$AR = a\log\left(\frac{(b15 + b23)}{(b19 + b20)}\right) \quad (8)$$

In the TIR, radiant temperature was calculated as the average of b42 (8.28 μm), b43 (8.71 μm), b44 (9.18 μm), and b46 (10.26 μm). The other TIR bands were excluded to avoid strong atmospheric and potential emissivity effects. To examine spatial

correlation between the variables, the data were masked to include only snow-covered pixels that were co-registered to the DEM and had albedos less than 1. Color composites, and calculated image statistics were then used to discern spatial patterns and relationships in contaminant content, grain size and temperature.

Ground truth at the Muir Snowfield:

Snow grain size and broadband solar albedo were measured along a 500-m transect at the Muir Snowfield concurrent with the MASTER overpass (Figure 5). Visual estimates of snow grain size were made with a grain size card. Solar albedo was estimated with a Kipp Radiometer [thermopile covered by a filtering dome (0.3-3.0 μm)], connected to a voltmeter. The radiometer was held one meter above and parallel to the snow surface slope. I estimated albedo by taking the ratio of outgoing to incident voltage.

Grain-size Estimation using DISORT:

A Mie scattering algorithm (Wiscombe, 1980) and radiative transfer model (DISORT) were used to model the BDR of a snow pack of ice spheres for specific regions of interest (ROI) in the MASTER data (Figure 5, Table 2). Using the optical constants (n, k) for warm ice [(Kou et al., 1993), (Warren, 1984)], Mie theory was used to calculate optical cross-sections of individual spherical ice grains ranging in radii from 50 μm to 2000 μm. For each ROI, incidence, emission, and phase angles were derived from the MASTER metadata, the solar azimuth and zenith, and the slope and aspect of the surface from the DEM. Next, DISORT was run using the ROI viewing geometry, and Mie output for each grain size. The modeled BDR were then compared with MASTER-estimated BDR to determine optical grain size. As optical grain sizes are modeled as equivalent spheres, optical grain size were translated to physical grain size using both published relationships between optical and physical grain size (Salisbury et al., 1994), and comparison with ground-truth data.

5. Results:

Results – Visible BDR/Albedo and Contaminants

MASTER VNIR data, and field measurements taken at the Muir Snowfield reveal a bimodal distribution, and significant natural variability in the contaminant content of Mt. Rainier's snow on August 26, 2001. In the MASTER VNIR data, an abrupt transition from high to low L_g was seen at a constant elevation of 2800 ± 100 meters (Figure 6). Image-derived BDR (Figure 7a&b) indicate that snow above the transition was highly reflective, ranging from 0.30-0.33 sr^{-1} at 0.4-0.6 μm on the Nisqually Glacier to 0.24-0.26 sr^{-1} at 0.4-0.6 μm above the Muir Snowfield. Below the transition, the image-derived BDR were spectrally flat and lower, ranging from 0.12 sr^{-1} on the Nisqually Glacier to 0.15 sr^{-1} on the Wilson Glacier. Differences in BDR between these two regions were greater than the natural variability, and estimated calculation error. Slight preferential absorption at shorter wavelengths was evident in the low BDR snow. Image-derived albedo indicate that snow above the transition was highly reflective (0.60-0.95 from 0.4-0.6 μm), while snow below the transition was less reflective (0.25-0.40 from 0.4-0.6 μm) (Figure 8). Substantial natural variability was evident in both the MASTER albedo estimates and the Kipp radiometer measurements of solar albedo (ranging from 0.26 ± 0.06 to 0.51 ± 0.06, mean 0.38 ± 0.06) (Figure 9). Pictures from ground-truth sites at the Muir Snowfield revealed the same transition from dirty to clean snow (Figure 10a), and variability in snow contaminant content on the surface (Figure 10b).

Results - Grain Size:

Linearly stretched color composites (Red: b15=1.78 μm, Green: b23=2.16 μm, Blue: b19=1.98 μm), revealed a distinct transition from high L_g to low L_g in b15 and b23 at approximately 3800 ± 300 m (Figure 11a). Normalized difference (Figure 11b), and ratio images (Figure 11c) showed that this transition to higher reflectance was more pronounced on the west side of the mountain, and extended on a shelf below Liberty Cap towards the North Mowich Glacier. When SWIR BDR spectra were extracted, peaks at 1.8 μm and 2.26 μm suggest that the snow at and

around the summit had a smaller grain size than all other regions (Figure 12a). With the exception of band 16 (1.83 μm), differences in BDR were greater than estimated calculation error (Figure 12b). Near-summit regions also showed less absorption than other clean snow spectra from 0.8-1.0 μm (Figure 7a&b). Thus, visible BDR was also consistent with the near-summit area having a smaller grain size.

Quantitative estimates of grain size were made by comparing image-derived BDR and albedo with DISORT modeling, laboratory measurements (Salisbury et al., 1994), and ground-truth data from the Muir snowfield. Optical grain radius was estimated by comparing image-derived BDR with modeled BDR. Near the summit, optical grain radii were between 50 and 100 μm (closer to 100 μm) (Figure 13a&b). At the Muir snowfield, optical grain radii were around 200 μm in both the clean and dirty snow (Figure 13c&d). Snow on the Wilson Glacier, the Emmons Glacier, the Nisqually Glacier and the Kautz Glacier all had optical grain radii around 200 μm (Table 2).

Comparing image-derived albedo spectra with measured albedo spectra allowed estimation of physical grain size (Figure 14). Grain sizes near the summit were between that of "coarse" snow (physical grain radius 500-1000 μm) and "medium" snow (physical grain radius 165-250 μm). For all other image-derived spectra, grain radii were larger than "coarse" snow. Visual inspection of snow grain radius at the Muir Snowfield suggested snow grain radii ranged in size from 500-2500 μm. Individual grain radii were as small as 500 μm while snow clumps ranged in size from 1000 to 2500 μm. The snow was wet and slushy in some places while granular and hard in others.

Results - Temperature:

The distribution of snow surface temperatures at Mt. Rainier on August 26, 2001 shows the effects of solar azimuth (north-facing sun 22º West of South), topography (shading behind ridges), and temperature lapse rate with elevation above the freezing line (Figure 15a). Temperatures below the freezing point appeared only at top of the mountain where snow temperature was not controlled by the phase change to water. The average melting line was at approximately 3940 ± 300 meters

implying that 6.8 km^2 were at a temperature below zero. Low standard deviation in calculated radiant temperature across MASTER TIR bands suggests that atmospheric and ε effects have been successfully removed from the data.

Results – Relationships between contaminants, grain size, and temperature

Histograms of temperature, grain size [ND ratio (Equation 6)], and visible albedo over the entire image indicate the degree of spatial variability of these variables (Figure 16). The majority of the snow has a temperature near the melting point, and a large grain size (i.e., small ND ratio). The albedo distribution is bi-modal, but shows significant variability (mean 0.54, std. 0.21). A color composite of radiant temperature (red), ND ratio (green), and visible albedo (blue) reveals three snow zones at Mt. Rainier on August 26, 2001 (Figure 17). Near the summit, a cyan region (Zone 1) indicates a low radiant temperature, a small grain size, and a large visible albedo. Below the summit, a maroon region (Zone 2) indicates a region of higher radiant temperature, larger grain size, and large visible albedo. The lowest elevation snow region (Zone 3) has a red/orange color indicating high radiant temperature, large grain size and low visible albedo.

Correlation statistics and 2-D scatter grams reveal the statistical and spatial correlation between visible albedo, negative ND ratio, and temperature (Figure 18a-c). Linear regression revealed a weak negative correlation between albedo and grain size (R^2 = -0.50). The 2-D scatter gram reveals that when visible albedo was low, negative ND ratio was large suggesting larger grain size (Figure 18a). However, when albedo was higher, a range in the negative ND ratio was observed suggesting a range of grain sizes. Linear regression revealed also revealed a weak and negative correlation between albedo and temperature (R^2 = -0.48). The 2-D scatter gram reveals that when temperature was high, a range of albedo was observed (Figure 18b). However, when temperature was low, only high albedo was observed. Finally, negative ND ratio and temperature are positively correlated (R^2 = 0.63). The 2-D scatter gram shows that when temperature was high, negative ND ratio was larger suggesting large grain size (Figure 18b). However, when temperature is low, negative ND ratio was small suggesting smaller grain sizes. Areas with larger grain

size and low temperature were concentrated on the eastern side of Mt. Rainier. These areas were poorly modeled with the DEM and had low solar incidence angles.

6. Discussion:

The end-of-the-melting season timing and the recent snowfall created an interesting spatial distribution of impurities, grain sizes, and temperatures on Mt. Rainier. A dramatic transition from dirty to clean snow (Zone 2 to Zone 3) is interpreted as a transition between net accumulation of snow from the recent storms, and lag deposit from summer ablation (i.e., net ablation or no accumulation from the recent storms). Variability in snow albedo show that contaminants are not uniformly distributed on the surface. Visual observations of contaminant thickness suggest that contaminants in the lag-deposit snow enhanced melting. Slightly stronger absorption at shorter wavelengths indicate that weathered volcanic rocks, containing iron oxide, may have contributed to snow contamination.

On August 26, 2001, the majority of the snow on Mt. Rainier was large-grained and had temperatures near the melting point. However, snow near the summit had sub-melting point temperatures and small grain sizes. In temperate regions, new wet snow undergoes destructive metamorphism at the freezing temperature resulting in a rapid increase in grain size and rounding of grains (Colbeck, 1982). In this process, heat transfer from large to small grains increases the average snow-pack grain size. At Mt. Rainier, spatial correlation between temperature and grain size suggests that snow near the summit remained cold, and therefore experienced little destructive metamorphism. On the other hand, high albedo melting snow from the recent storm experienced significant destructive metamorphism.

This analysis demonstrates the power of remote-sensing techniques, coupled with field work and modeling, to estimate snow pack properties such as BDR, albedo, contaminant content, grain size, and skin temperature. The main limitations of this study were DEM accuracy, limited viewing geometries, atmospheric correction, and different definitions for snow grain size. Despite limitations, our methods could be extended to lower resolution multi-spectral satellite data (e.g.,

ASTER or Landsat 7).

Estimates for visible albedo were limited by inaccurate topographic modeling, and a limited range of viewing geometries. When the DEM and the MASTER data set were not co-registered, or when local topography created low solar incidence angles, estimates for albedo were physically unrealistic. As solar illumination angle become increasingly oblique, snow exhibits increasingly strong forward scattering (Warren et al., 1998). As a result, assuming that snow is a Lambertian reflector leads to error in albedo estimation, especially at off-nadir viewing geometries. Most of the variability in ROI snow albedo is attributed to differences in solar illumination angle and their effect on snow BDR. For example, Solar illumination angles greater than 40º may explain why VNIR albedo estimates for the Emmons Glacier and the Summit are lower than for other regions.

Comparison of DISORT and measured reflectance values with estimated BDR and albedo demonstrates that MASTER can be used to estimate optical and physical grain sizes of snow. However, differences in grain size definition and atmospheric correction limit precise determination of snow grain size. For the interpretation of spatial patterns and relationship to other variables, such as temperature or dirtiness, the relative difference in grain size is equally useful.

Different grain size definitions may explain some of the discrepancies between physical and optical grain size estimations. While optical grain sizes are determined by the distance between scattering opportunities (i.e., air bubbles or internal grain boundaries), grains of snow measured visually could include many scattering interfaces. This difference between optical and physical grain size will be greatest with dry, non-spherical snow grains. However, optical grain sizes should be close to physical grain sizes for rounded and wet grains for two reasons: 1) As water and ice have the same absorption coefficient, scattering is inhibited at snow-water interfaces. 2) Warm snow grains are often more spherical as they have experienced destructive metamorphism. In this study, a factor-of-two discrepancy exists between the optical and physical grain size estimates for dirty snow at the Muir Snowfield. However, this discrepancy can be explained by differing definitions; optical grain sizes were estimates of individual snow grains while physical grain size

measurements included clusters of grains. Matched laboratory and modeled values (Salisbury et al., 1994) provide a useful sample translation from optical to physical grain size.

The identified reflectance peaks are sensitive to atmospheric correction near 1.8 μm, a strong water absorption feature, and decreasing solar irradiance. These uncertainties are reduced with concurrent atmospheric parameterization, accurate measurement of the detector's spectral response, and low detector noise.

Emissivity (ε) and atmospheric correction limit the accuracy of snow surface temperature estimation. In this study, low standard deviation across bands indicates that ε and atmospheric effects were successfully removed. Temperatures above the melting point of snow could result from sub-pixel mixing of melting snow and dirt.

7. Conclusion:

MASTER VNIR, SWIR, and TIR data can be used to estimate snow contaminant content, grain size, and temperature respectively. In combination, these data reveal the surface radiative dynamics of Mt. Rainier's glacier system on a hot summer day after a recent snowfall. Whereas most of the snow was had large grains and melting point temperatures, an area near the summit had small grain size and sub-melting point temperatures. The high spatial correlation of the temperature and the grain size distribution imply that where temperatures reached the melting temperature, rapid metamorphism occurred. These results reveal the power of high spatial and spectral resolution remote sensing to estimate snow pack properties important to radiative balance.

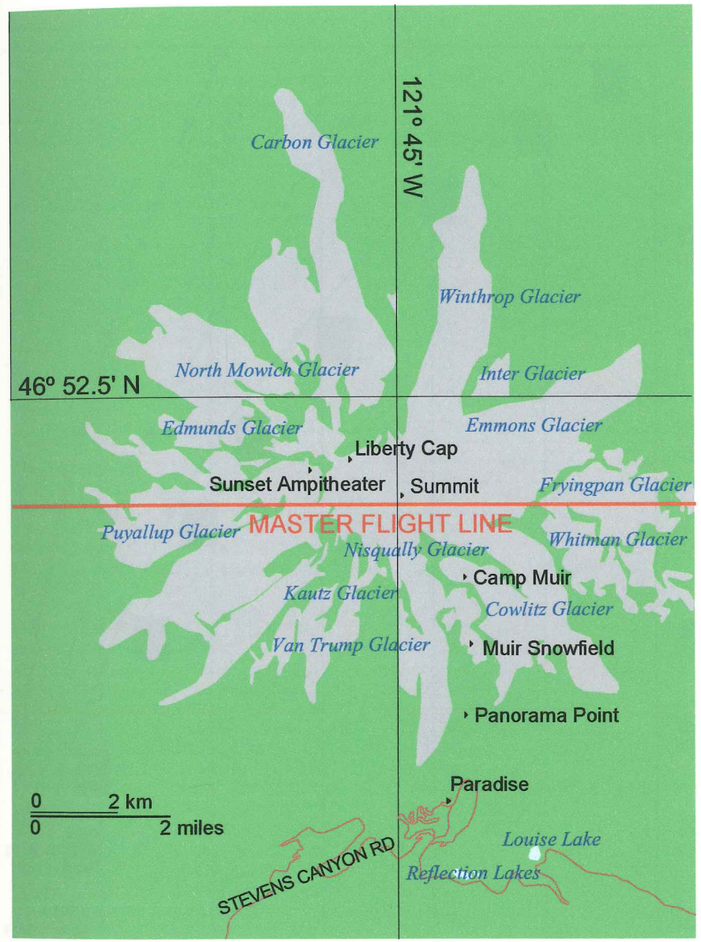

Figure 1. Map Showing MASTER Flight Line and Named Locations at Mt. Rainier, WA

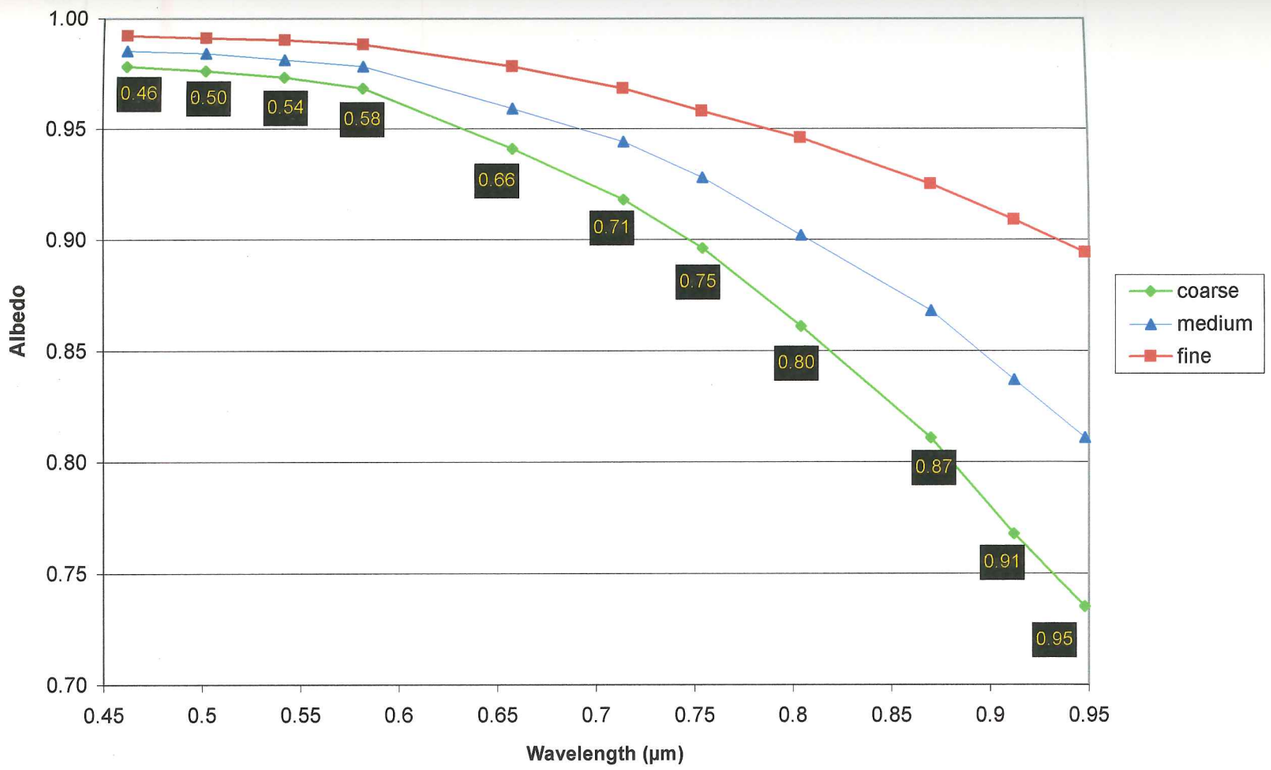

Figure 2a. Visible and Near-Infrared (VNIR) Albedo of Snow Convolved to MASTER Bands 1-11
source: http://speclib.jpl.nasa.gov/

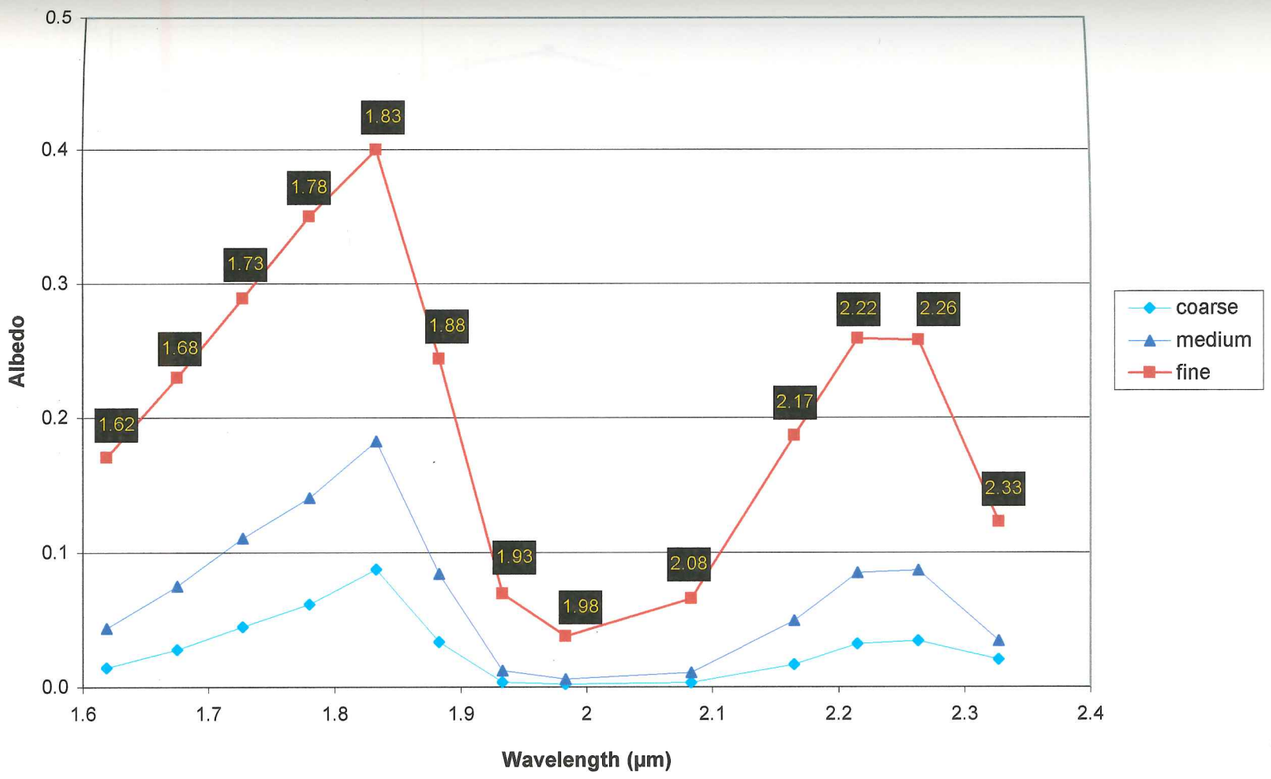

Figure 2b. Short-wave Infrared (SWIR) Albedo of Snow Convolved to MASTER Bands 12-25
source: http://speclib.jpl.nasa.gov/

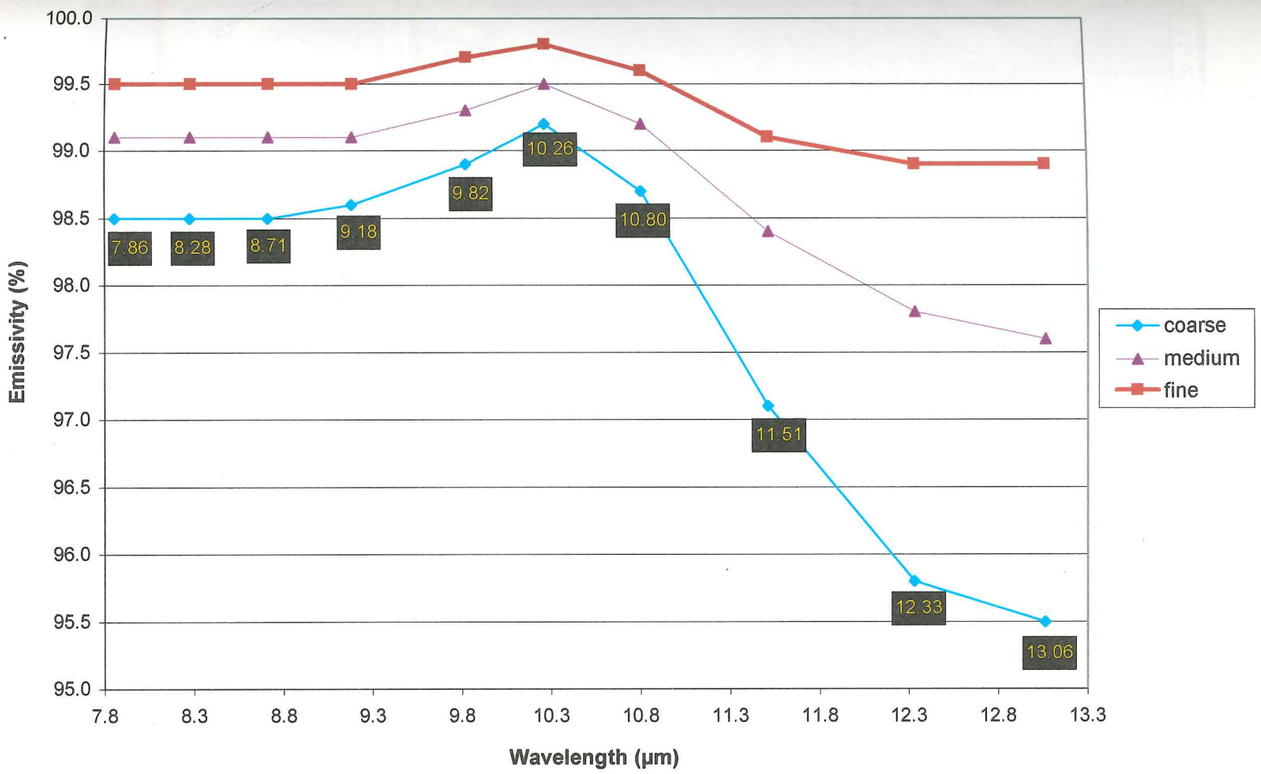

Figure 2c. Thermal-Infrared (TIR) Emissivity of Snow Convolved to MASTER Bands 41-50
source: http://speclib.jpl.nasa.gov/

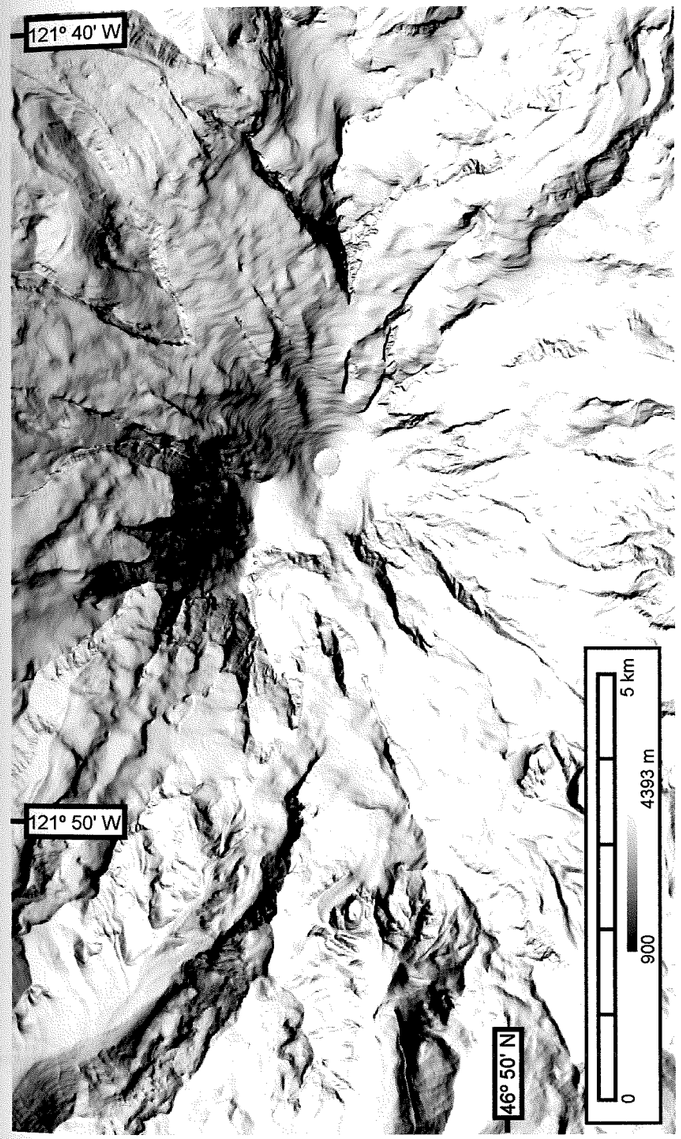

Figure 3. USGS Digital Elevation Model (DEM) Co-registered to the August 26, 2001 MASTER Flight Line

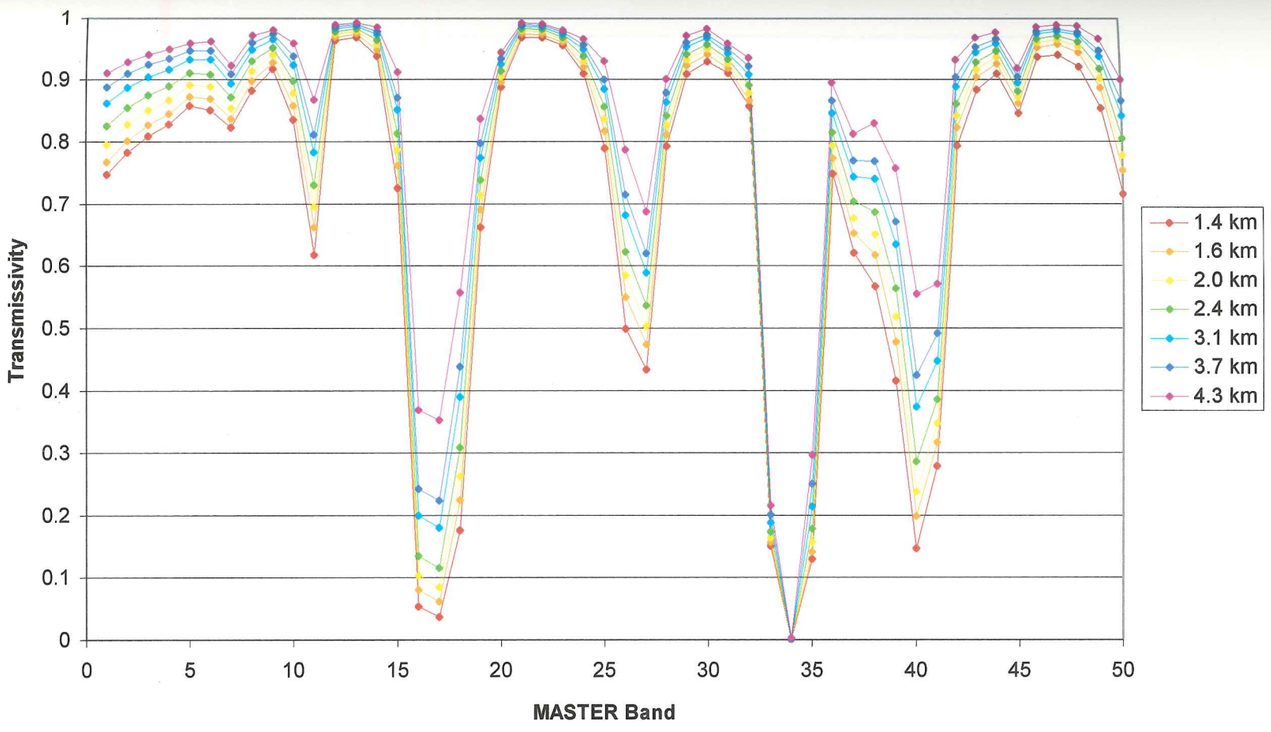

Figure 4a. MODTRAN Predictions for Transmissivity at Louise Lake (1.4 km), Paradise (1.6 km), Panorama Point (2.0 km), Kautz Glacier (2.4 km), Camp Muir (3.1 km), Sunset Ampitheater (3.7 km), and the Summit Crater (4.3 km)

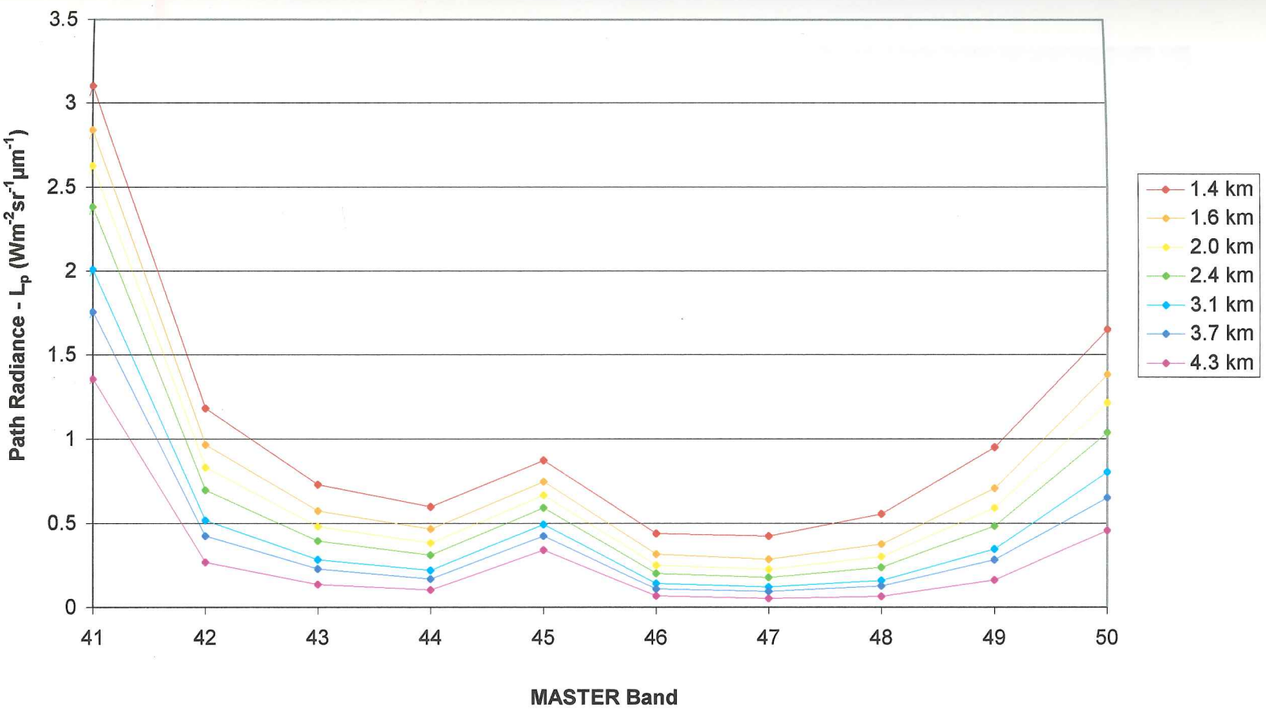

Figure 4b. MODTRAN Predictions for Path Radiance at Louise Lake (1.4 km), Paradise (1.6 km), Panorama Point (2.0 km), Kautz Glacier (2.4 km), Camp Muir (3.1 km), Sunset Ampitheater (3.7 km), and the Summit Crater (4.3 km)

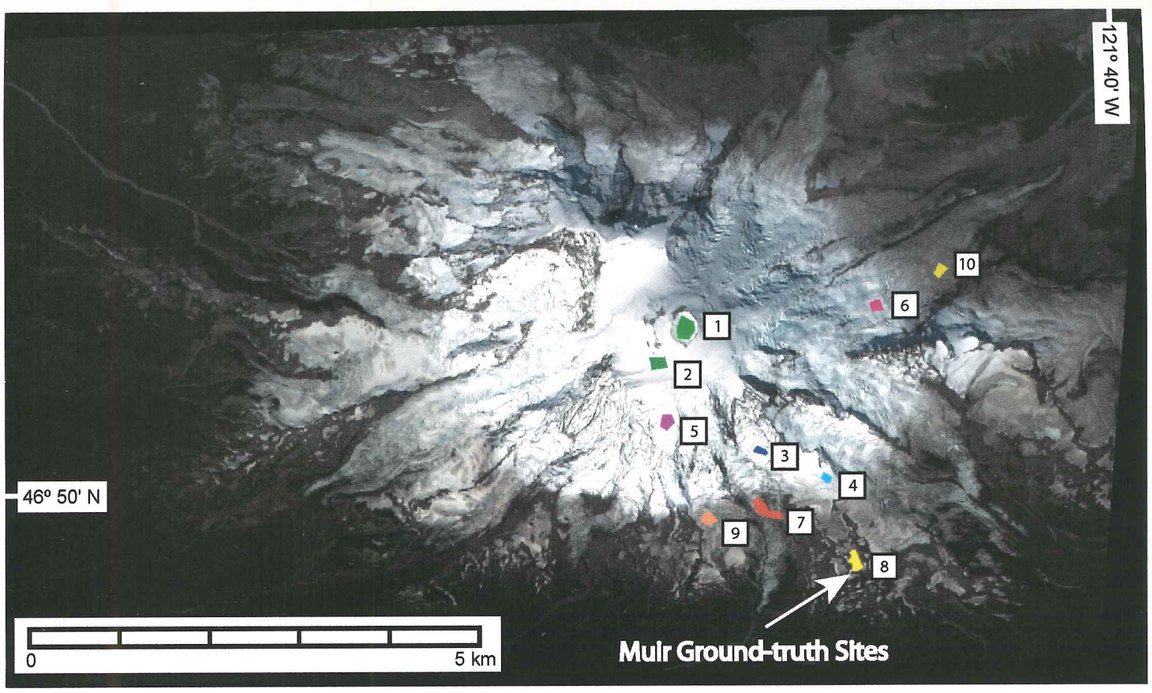

Figure 5. Location Map for Regions of Interest (ROI) and Ground-Truth Sites
Note: See Table 2 for ROI names.

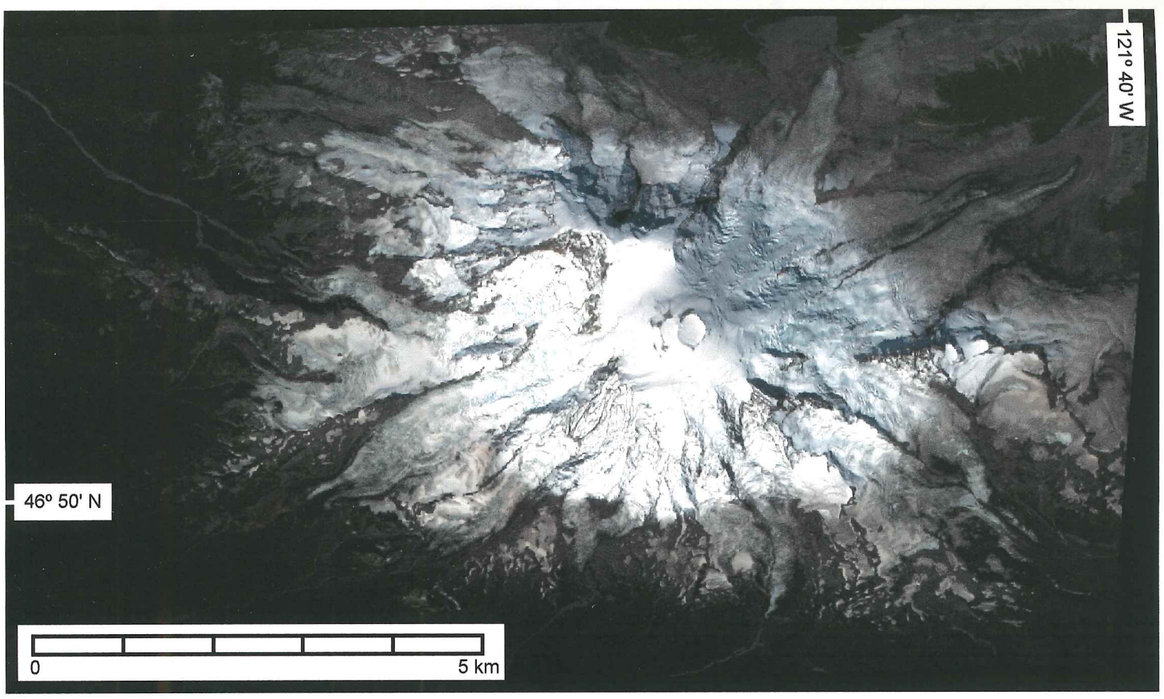

Figure 6. Visible Land-Leaving Radiance Color Composite (Red: Band 5 - 0.66 µm, Green: Band 3 - 0.54 µm, Blue: Band 1 - 0.46 µm)

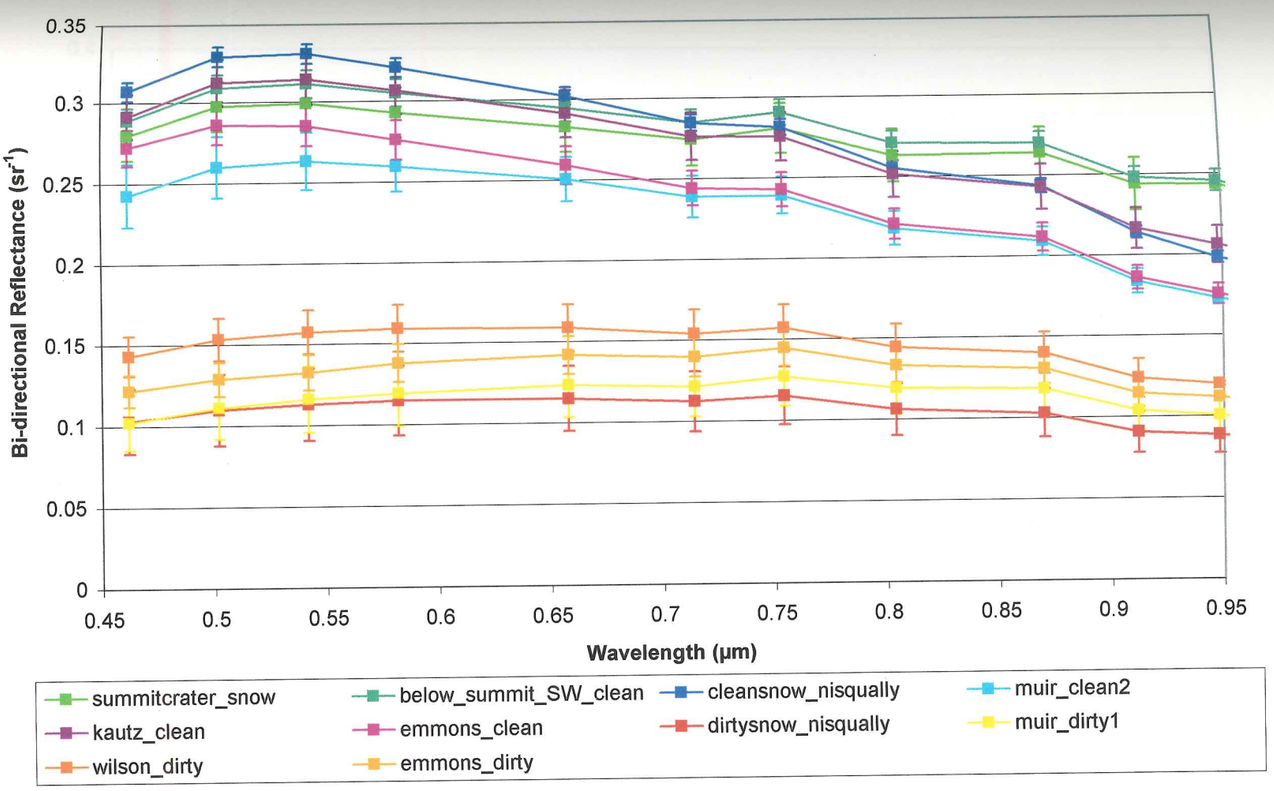

Figure 7a. VNIR Bi-directional Reflectance (BDR) Error bars represent standard deviation in measured BDR for each region of interest (ROI).

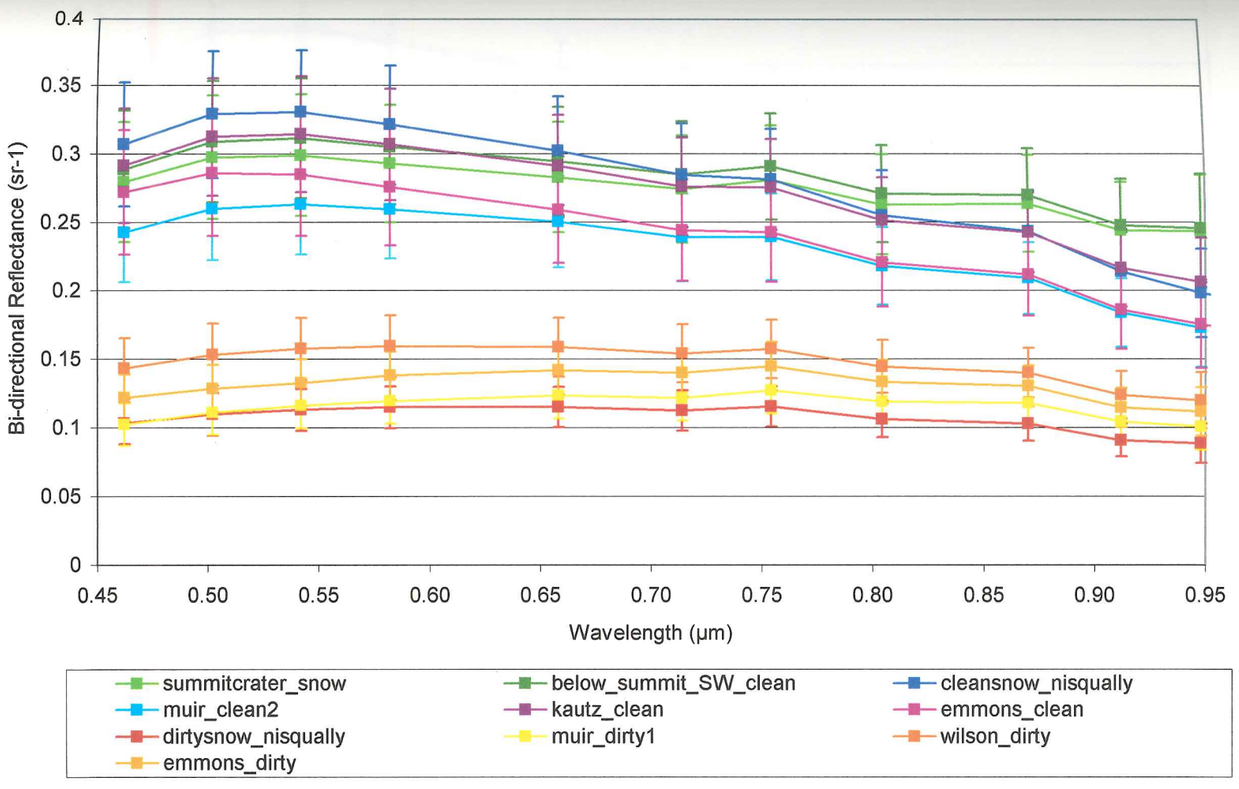

Figure 7b. VNIR Bi-directional Reflectance (BDR) Error bars represent expected calculation error (Eq. 5).

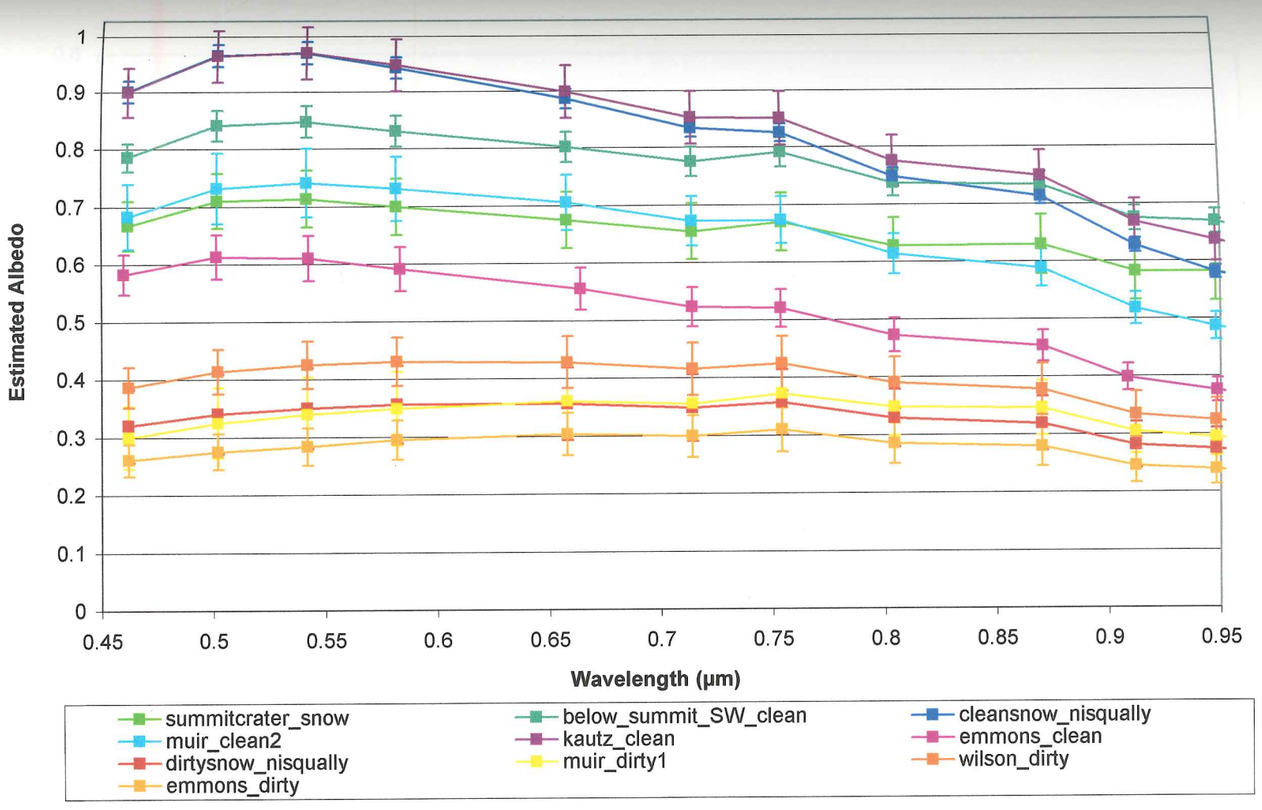

Figure 8. VNIR Albedo Error bars represent standard deviation in calculated albedo for each region of interest (ROI).

Figure 9. Broadband Solar Albedo (0.4 - 2.5 µm) at the Muir Snowfield

Figure 10a. View up to the Summit and the Nisqually Glacier from the Muir Snowfield An abrupt transition from clean to dirty snow is seen close to the summit.

Figure 10b. Variability in Snow Contaminant Content at the Muir Snowfield

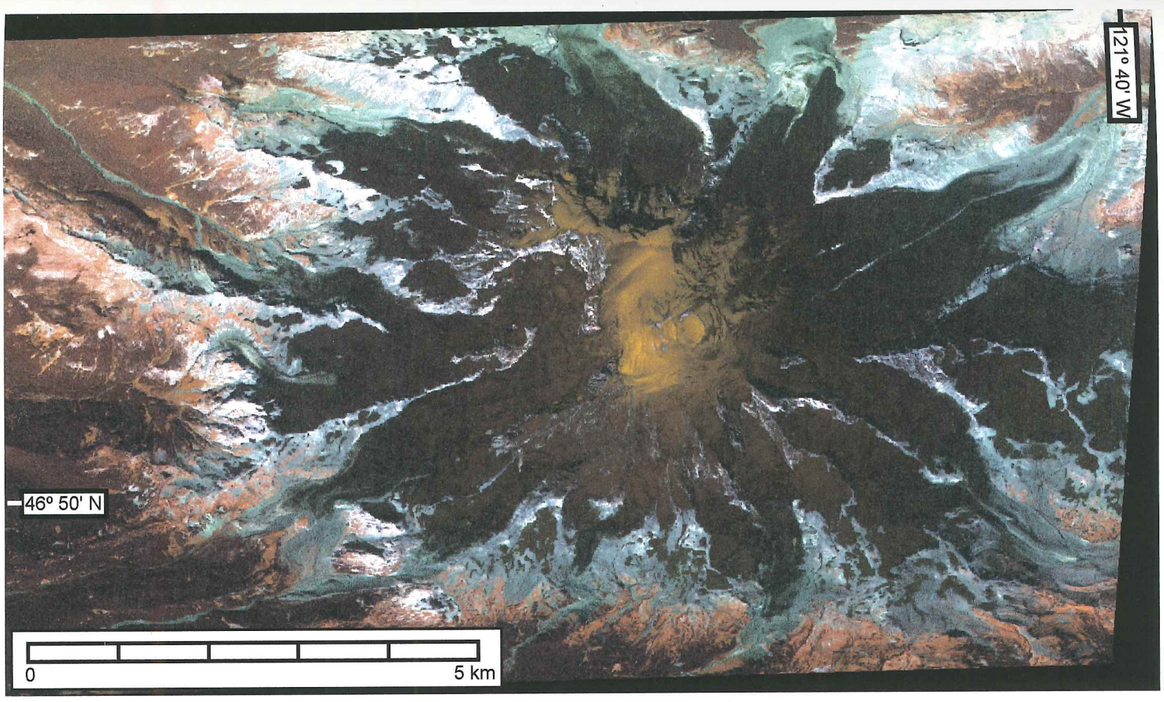

Figure 11a. SWIR Color Composite (Red: Band 15 - 1.78 µm, Green: Band 23 - 2.16 µm, Blue: Band 19 - 1.98 µm) A distinct area of higher land-leaving radiance in b15 and b23 (yellow color) indicates that regions near the summit have a smaller grain size.

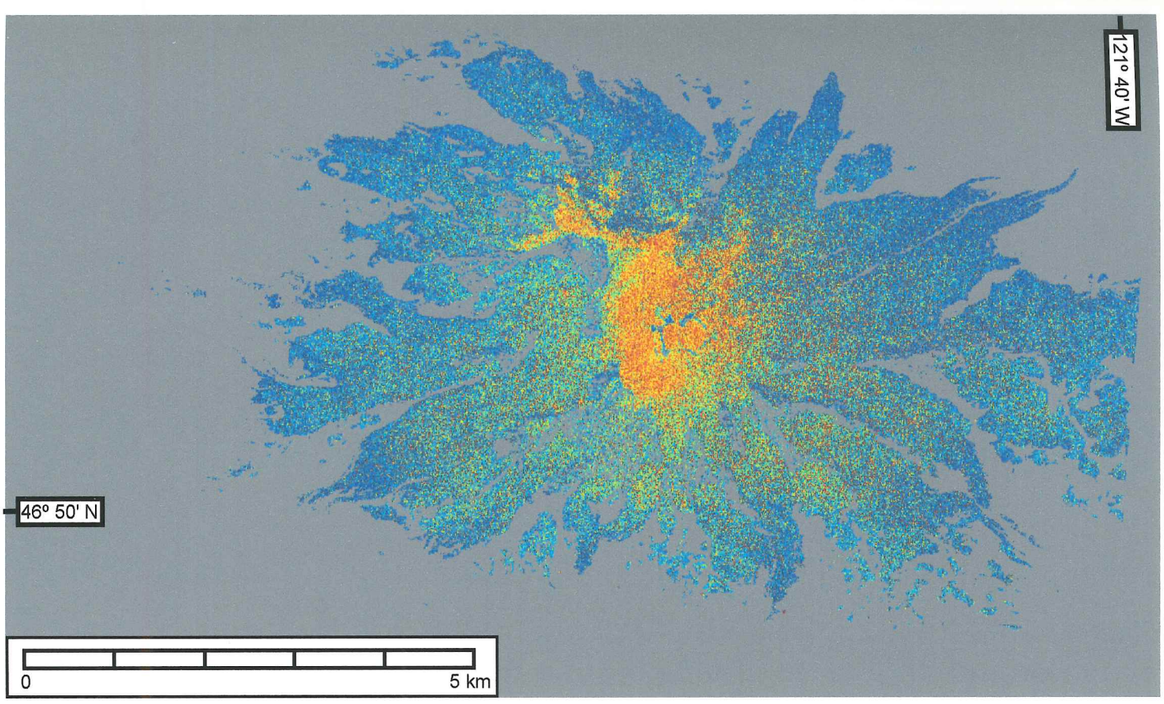

Figure 11b. Normalized Difference Ratio (NDR - Eq. 7) Image Cooler colors indicate a smaller NDR (larger grain size) while warmer colors indicate a higher NDR (smaller grain size).

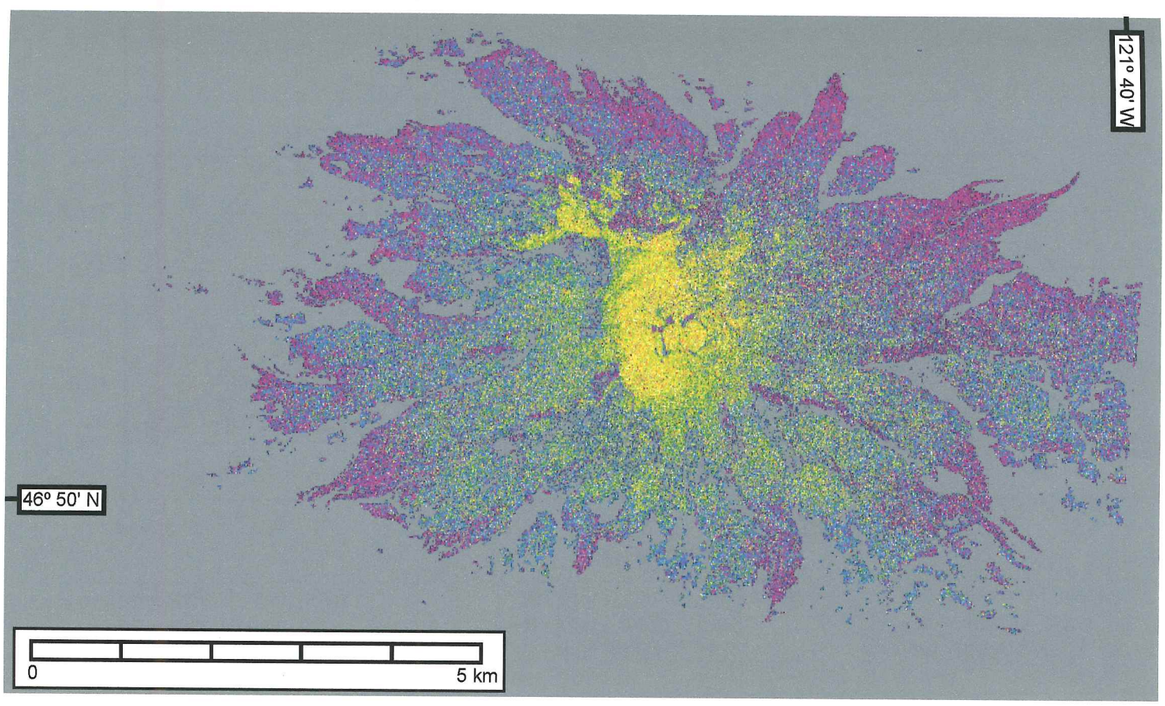

Figure 11c. Absorption Ratio (AR - Eq. 8) Image Yellow colors indicate a lower AR (smaller grain size) while purple colors indicate a higher AR (larger grain size).

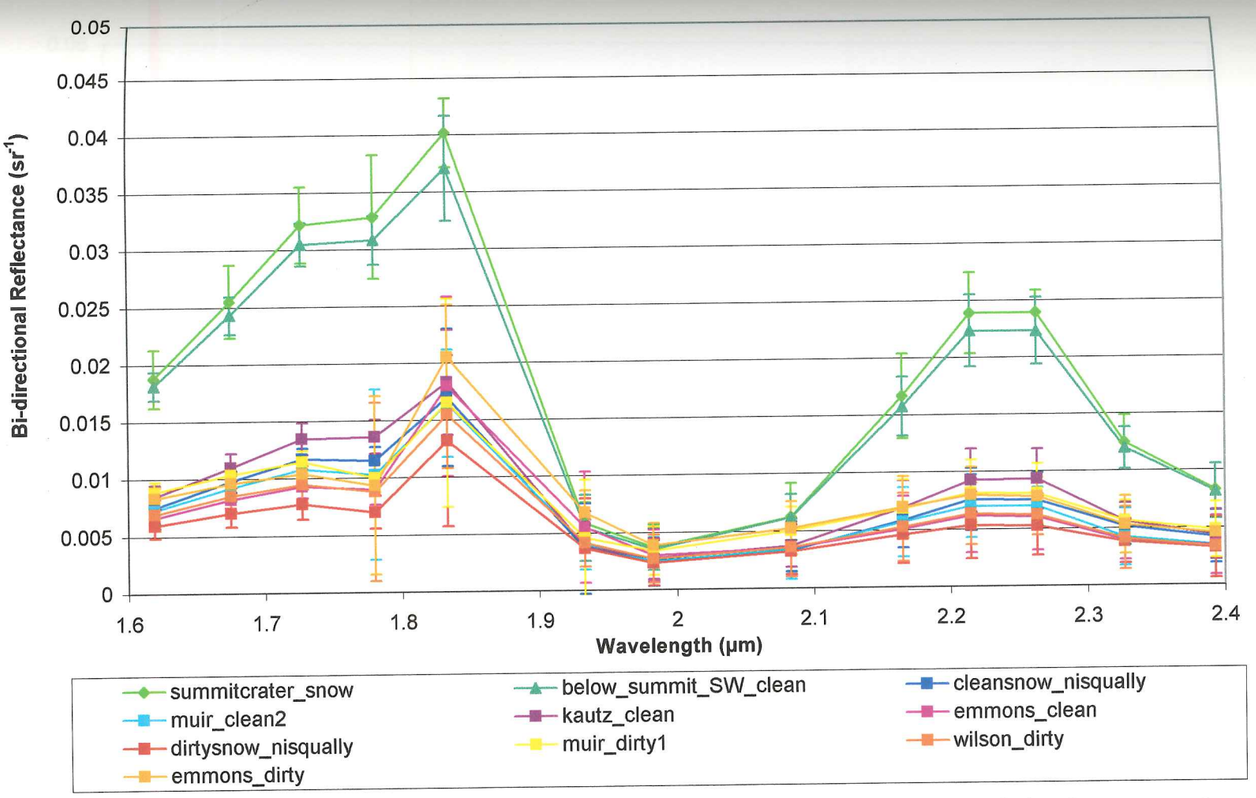

Figures 12a. SWIR Bi-directional Reflectance (BDR) Error bars represent standard deviation in measured BDR for each region of interest (ROI).

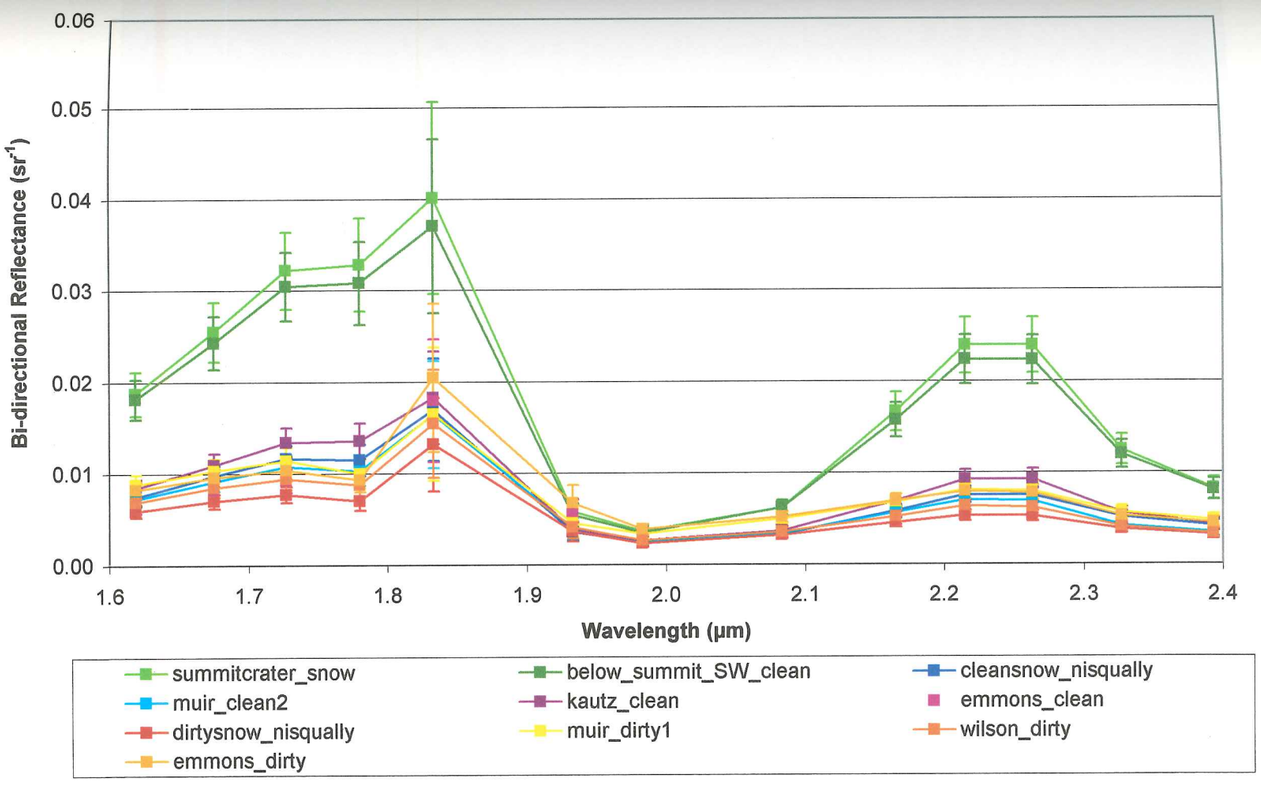

Figure 12b. SWIR Bi-directional Reflectance (BDR) Error bars represent expected calculation error (Eq. 5).

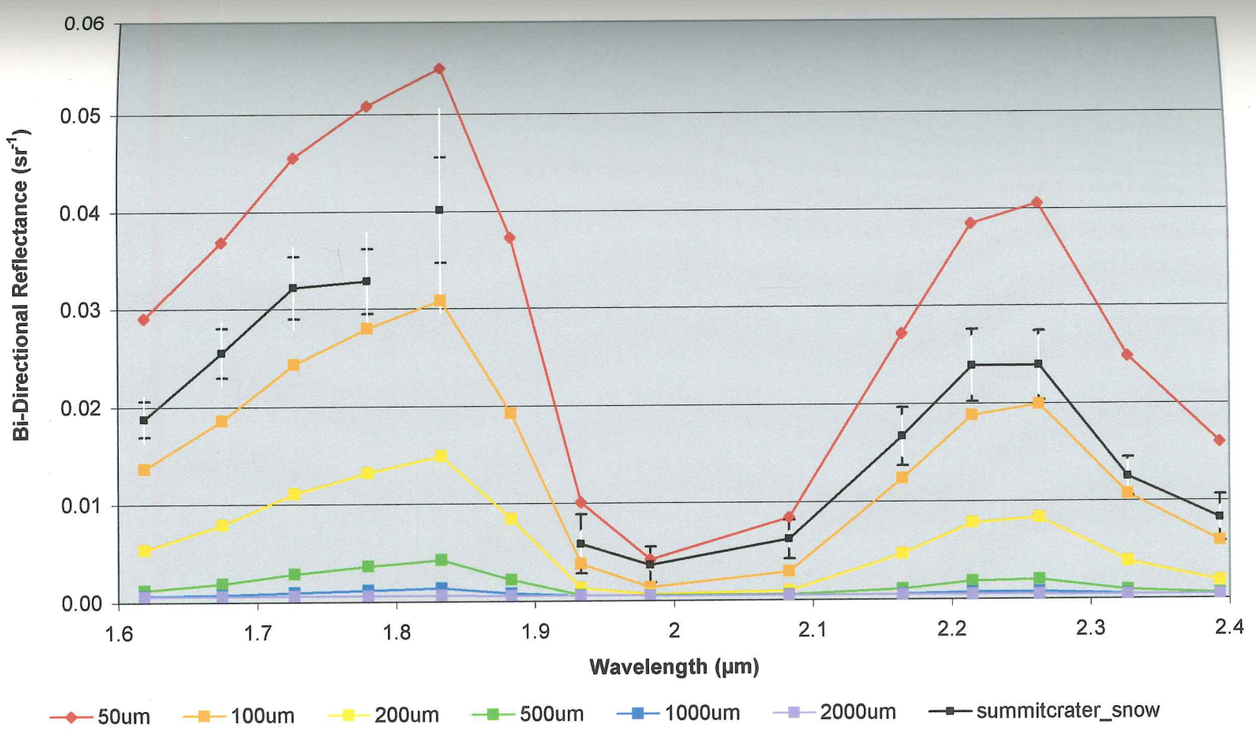

Figure 13a. Comparison of DISORT and MASTER Bi-directional Reflectance (BDR) for Summitcrater_snow Black error bars represent standard deviation in region of interest BDR while white error bars represent estimated calculation error. Dirty snow at the Muir Snowfield has an optical grain size ~75 µm.

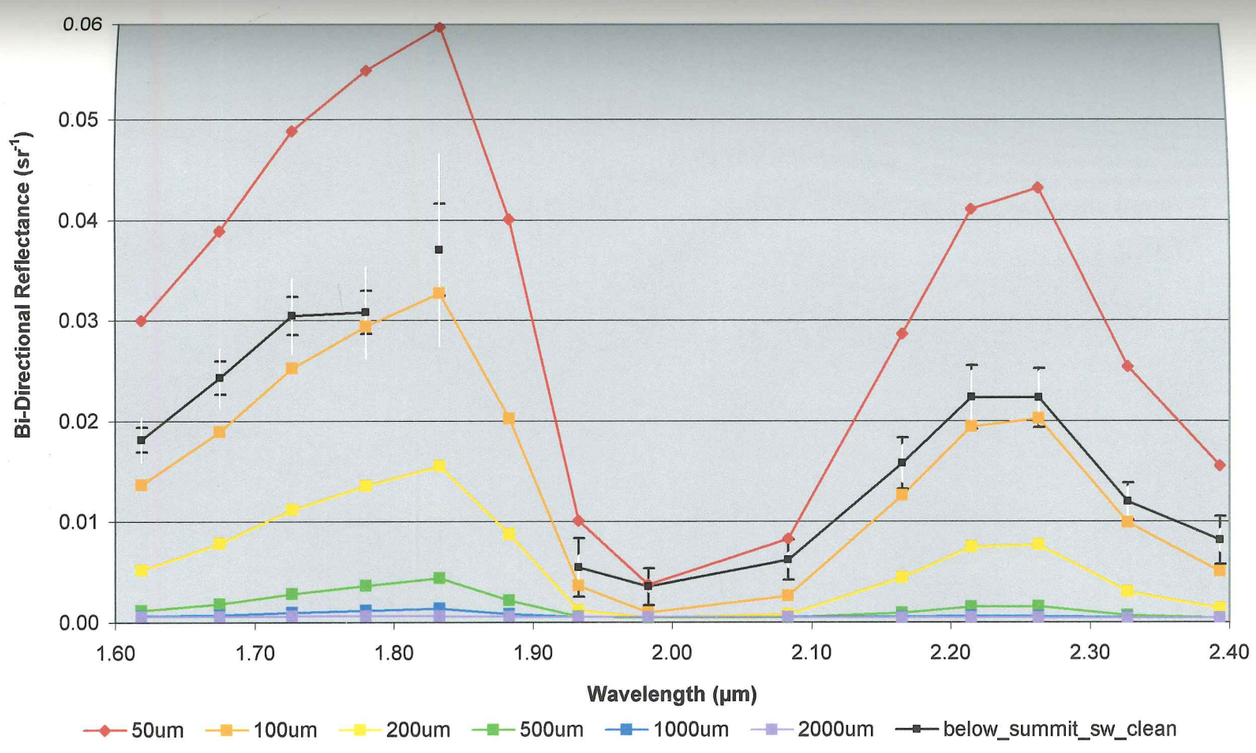

Figure 13b. Comparison of DISORT and MASTER Bi-directional Reflectance (BDR) for Below_summit_sw_clean Black error bars represent standard deviation in region of interest BDR while white error bars represent estimated calculation error. Clean snow beneath the summit crater has an optical grain size ~75 µm.

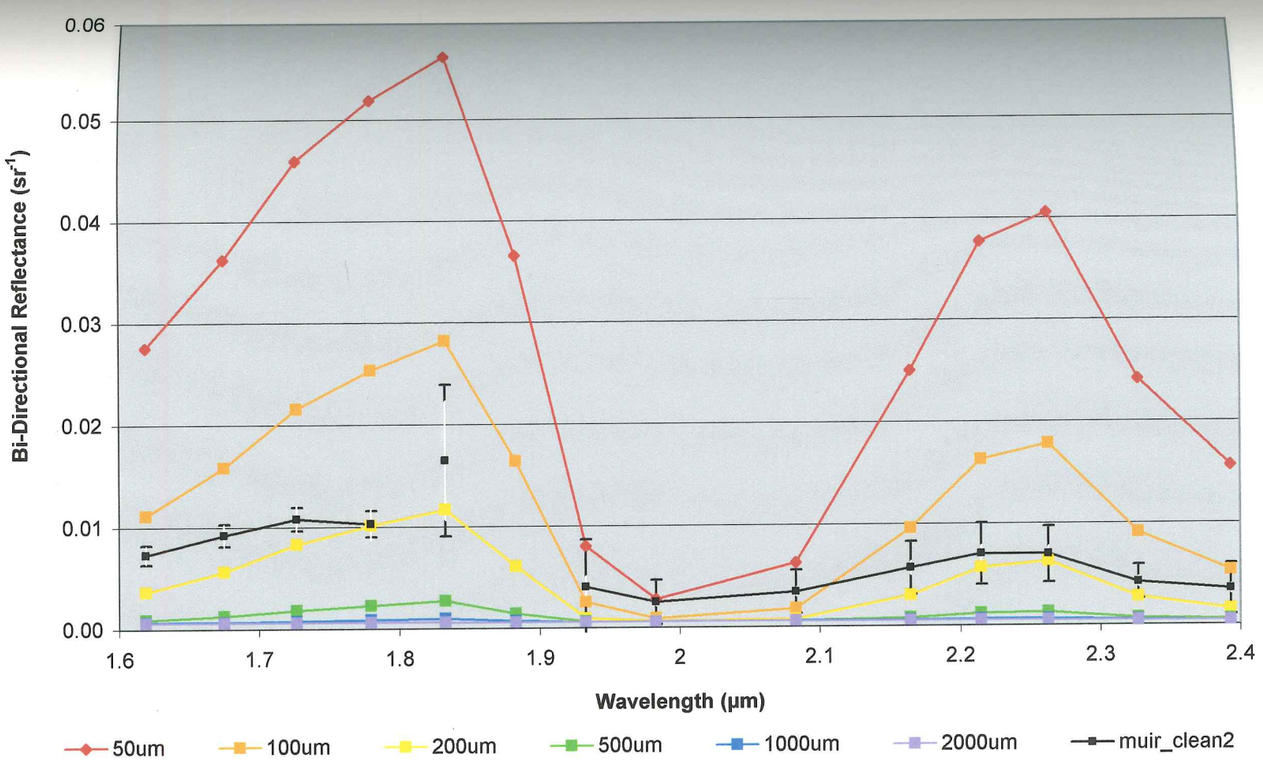

Figure 13c. Comparison of DISORT and MASTER Bi-directional Reflectance (BDR) for Muir_clean2 Black error bars represent standard deviation in region of interest BDR while white error bars represent estimated calculation error. Dirty snow at the Muir Snowfield has an optical grain size ~200 µm.

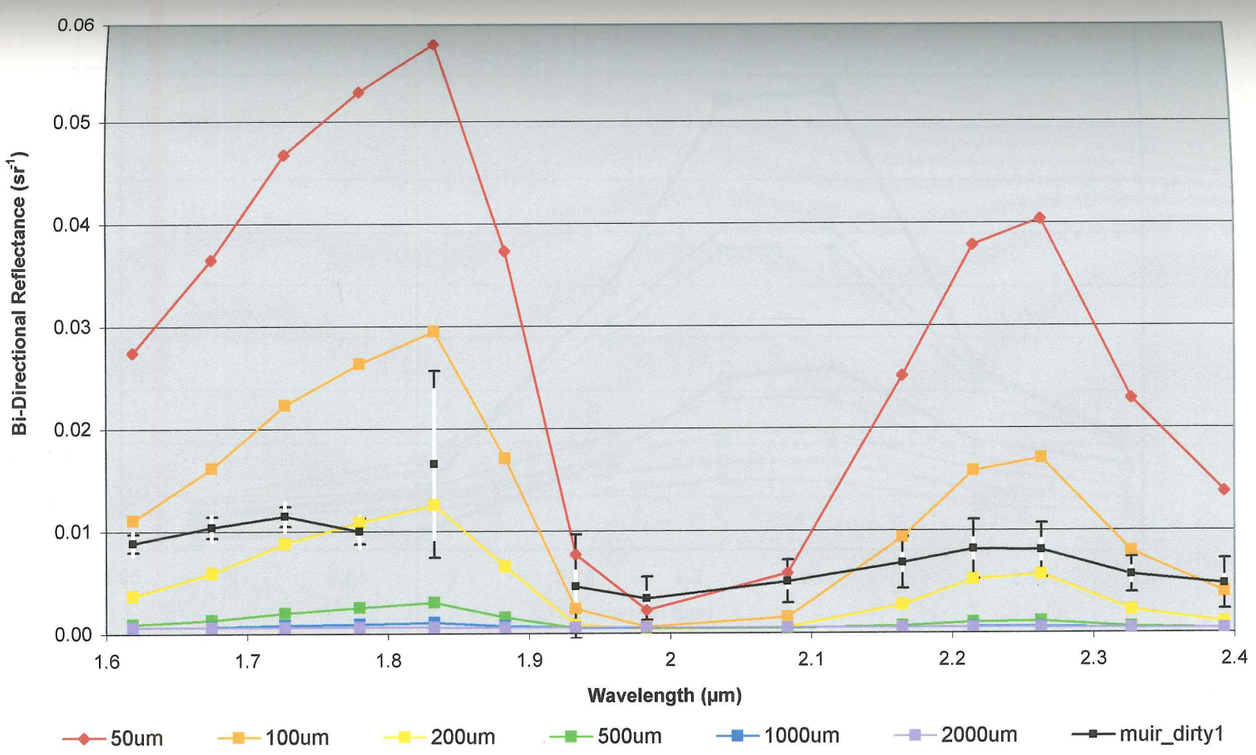

Figure 13d. Comparison of DISORT and MASTER Bi-directional Reflectance (BDR) for Muir_dirty1
Black error bars represent standard deviation in region of interest BDR while white error bars represent estimated calculation error. Dirty snow at the Muir Snowfield has an optical grain size ~200 µm.

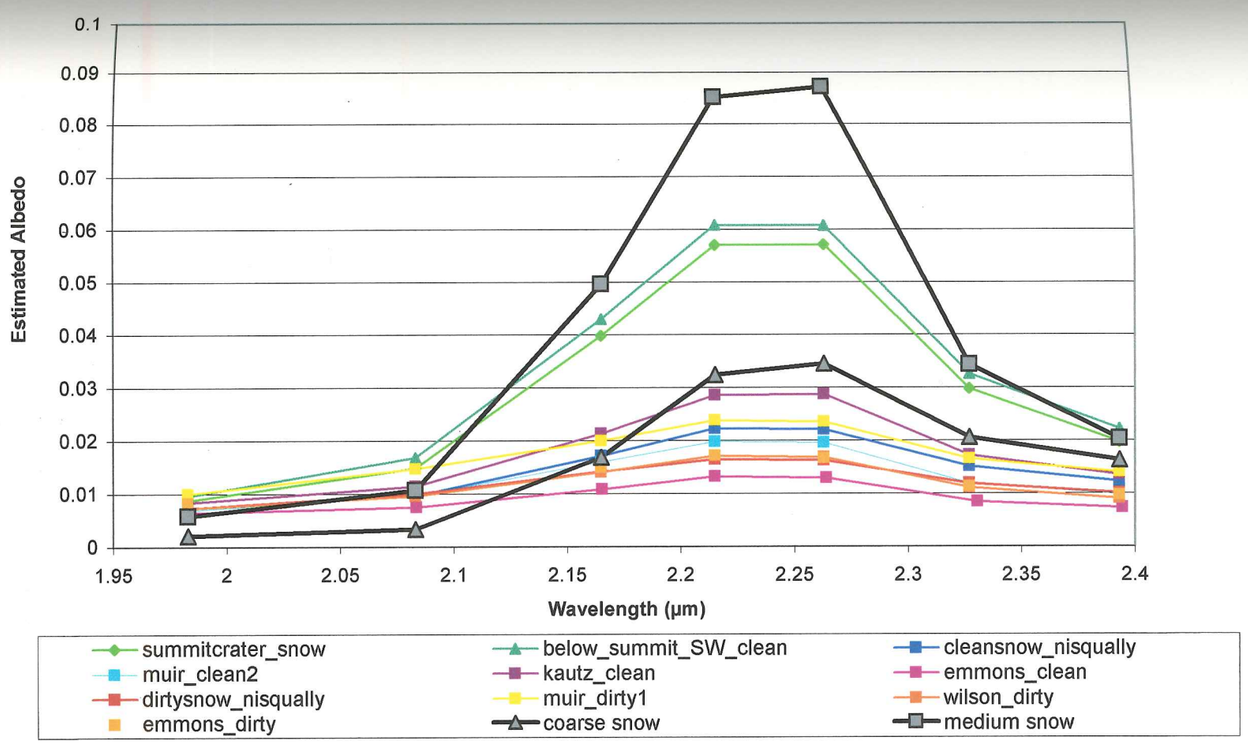

Figure 14. Comparison of MASTER-estimated and measured SWIR albedo for measured physical grain radii *[Salisbury et al., 1994]* Summitcrater_snow and below_summit_SW_clean have physical grain radii between medium snow (165-250 μm) and coarse snow (500-1000 μm). All other regions of interest (ROI) have physical grain radii greater than coarse snow.

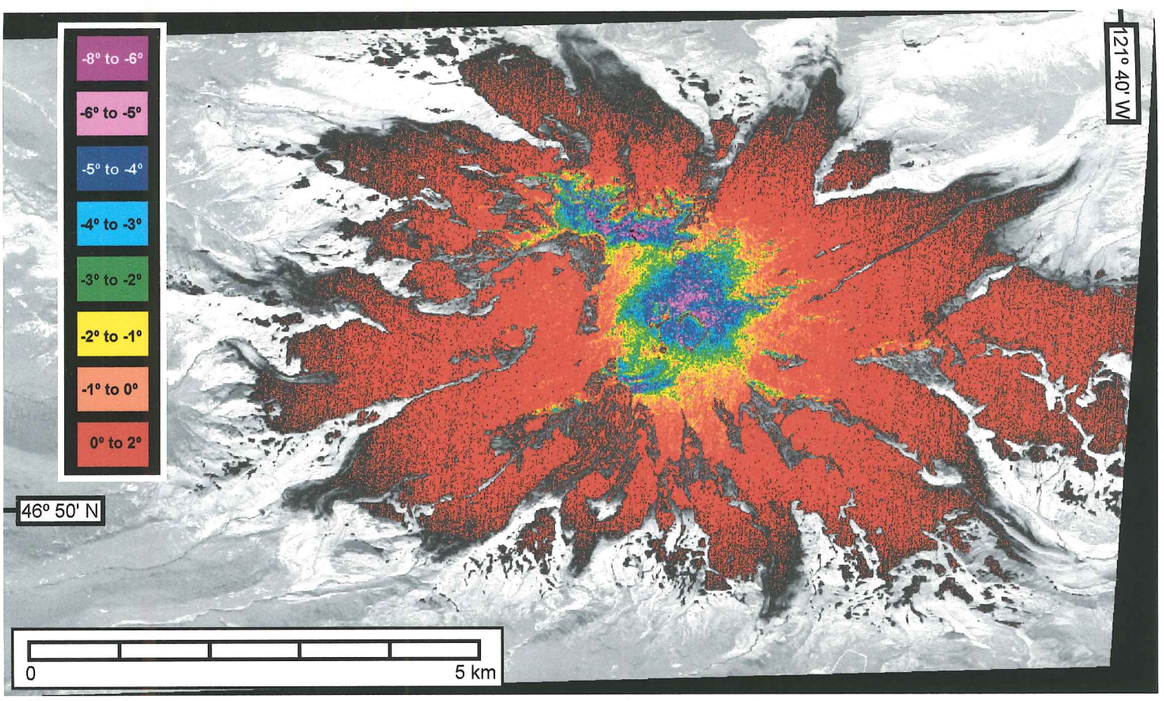

Figure 15. Average Radiant Temperature - MASTER Bands 42 (8.28 µm), 43 (8.71 µm), 44 (9.18 µm) & 46 (10.26 µm)

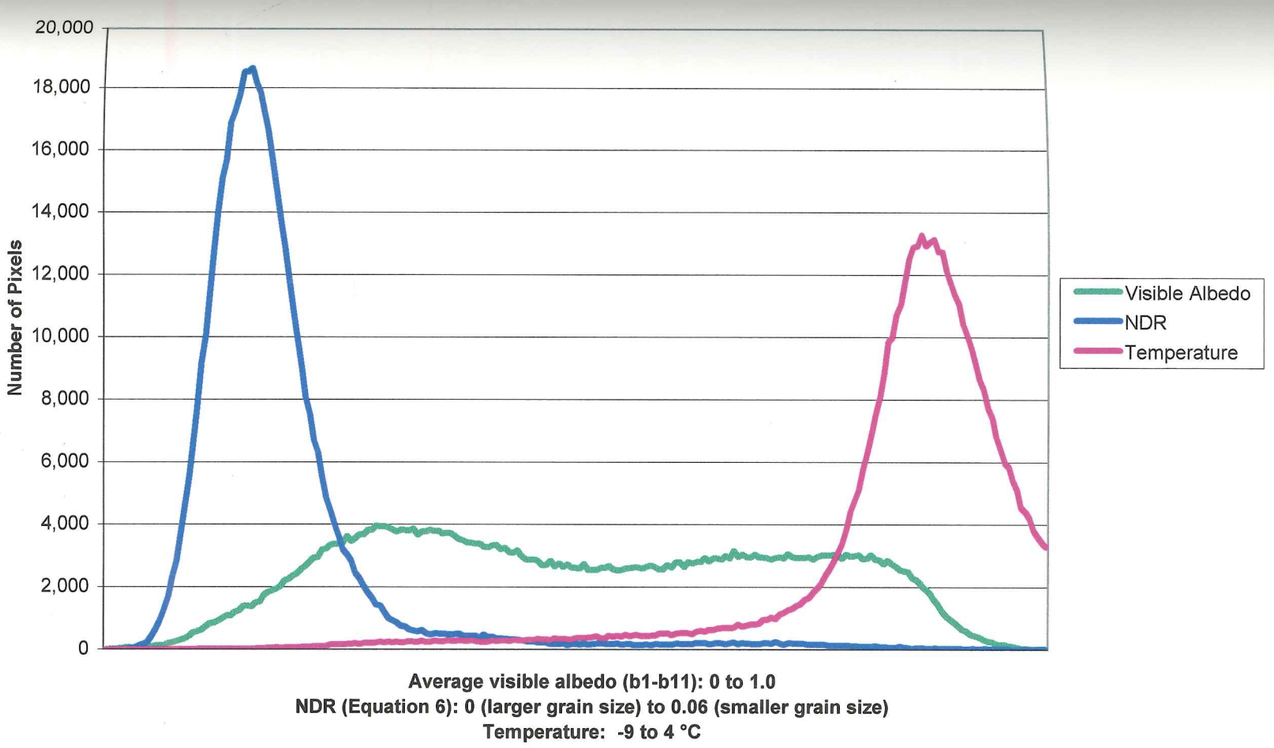

Figure 16. Histogram of Snow-Pack Properties for Masked Snow Pixels The majority of the snow at Mt. Rainier on August 26, 2001 was larger grained and melting (i.e., temperature at the melting point). The snow had a bi-modal distribution of visible albedo.

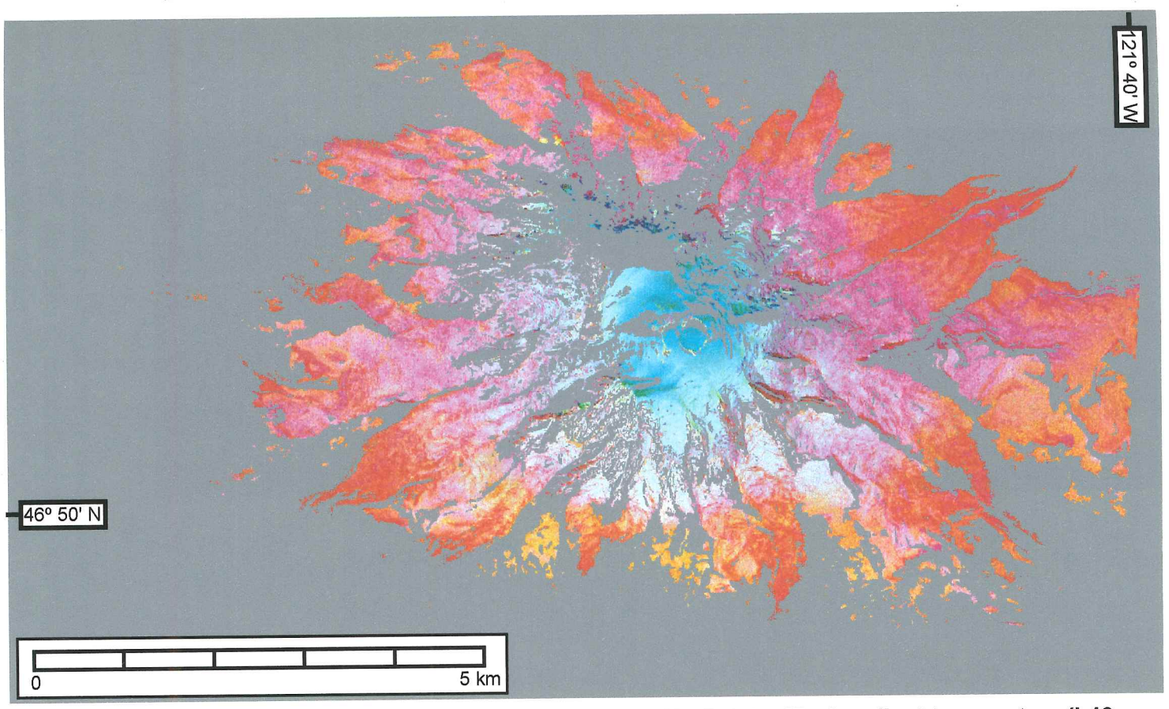

Figure 17. Color Composite Showing Three Snow Zones on Mt. Rainier [Red: radiant temperature (b42, b43, b44 & b46), Green: grain size proxy (NDR - Equation 7), Blue: visible albedo (b1-b11)]

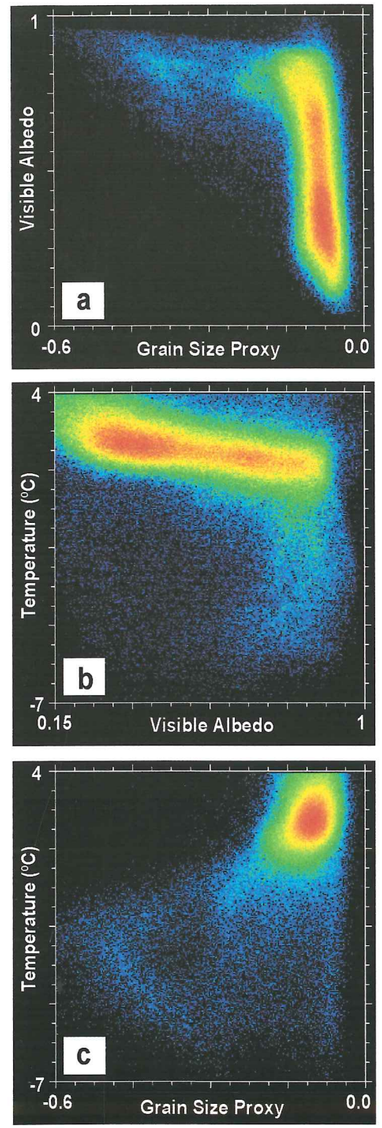

Figure 18a-c. Two-dimensional scatter grams of visible albedo (b1-11), grain size proxy (negative NDR - Equation 6), and radiant temperature (b42, b43, b44, & b46) for masked snow pixels

Chapter II. Estimation of Water Temperature From Airborne and Satellite Thermal-Infrared (TIR) Remote-Sensing Data

ABSTRACT:

Emitted thermal infrared radiation (TIR, λ=8-14 μm) can be used to monitor the surface temperature (top ~100 μm) of streams and lakes that have important environmental and economic value. However, before TIR data can be used with confidence by regulators and hydrology modelers, the accuracy of recovered temperatures must be evaluated. As ground-truth data and extensive processing time and skills are not always available, constraining the accuracy of both raw and processed data is essential. I use multi-spectral airborne scanner data (MASTER), multi-spectral satellite data (ASTER), and single-band satellite data (LANDSAT 7) to evaluate the corrections required to estimate spatially resolved water temperatures in TIR data. Emissivity, atmospheric absorption and emission, and surface effects (e.g., wind, multiple scattering) are evaluated. Although water is often approximated by a blackbody in the TIR, laboratory measurements of water reflectance (~1-2 %) suggest that this assumption could lead to underestimation of radiant temperatures by ~0.8 °C. Quantitative removal of atmospheric effects to obtain absolute radiant temperature requires radiative-transfer modeling [e.g., MODerate resolution TRANsmission (MODTRAN)]. Using MODTRAN, I illustrate how the magnitude of atmospheric correction varies with total column water (TCW), sensor elevation and target temperature. Three criteria are used to select and evaluate emissivity and atmospheric corrections on TIR data: 1) comparison with temperature and atmospheric ground-truth 2) the spectral shape of recovered temperatures 3) consistency across flight lines. After correction, 90% of remotely sensed lake temperatures are within 1 °C of persistent and concurrent radiant and surface kinetic ground-truth temperatures. Recovered stream temperatures deviate from gage measurements by up to 2.3 °C due to surface and sub-pixel mixing effects. This work has important implications for the future of TIR platform design for environmental monitoring (i.e. band placement, spectral and spatial resolution). In

addition, it provides evaluation of the limitations of MODTRAN, a standard atmospheric correction tool for terrestrial remote sensing.

1. Introduction:

Monitoring of stream and lake temperatures is important for water quality management, land-use monitoring, and hydrological studies. Elevated temperatures threaten the ecological integrity of many water habitats, especially in the summer when critical thresholds (e.g., 16°C in streams for coldwater fish) are exceeded. Although debate exists about the effect of urbanization on stream temperature [e.g., Larson and Larson (1996), Beschta (1997)], land-use change can elevate temperatures through two mechanisms: 1) the removal of riparian vegetation increasing direct Solar radiation 2) an increase in impervious land-surface allowing warmer surface run-off to overpower cooler groundwater (Poole and Berman, 2001). Human modification of groundwater dynamics, riparian vegetation, and channel morphology, should be addressed in water temperature management planning (Poole and Berman, 2001). A spatial distribution of 'skin' water temperature can serve as a boundary condition for hydrological models [e.g., (Schott et. al., 2001)]. Although point measurements reveal temporal variation in water temperature, the benefit of TIR remote sensing over field-based measurements is a quantitative spatial understanding of temperature distribution. Temperature gradients can be used to identify the location of ground and surface water inputs in watersheds. For all of these applications, water surface temperature should be accurate within 1 °C.

TIR remote sensing has been used to estimate sea-surface temperatures (SST) [e.g., Smith et. al. (1998), Emery and Yu (1997)] and lake temperatures [e.g., LeDrew and Franklin (1992), Schott (2000)]; however, less work has been done with streams and rivers because they are often unresolved in remotely sensed data. Torgerson [2001] evaluated the accuracy of remotely sensed stream temperature measurements using very high-resolution imagery (0.2-0.4 m) obtained with a low-flying helicopter. Although several sources of error were identified (reflected long-wave radiation, thermal boundary layer effects at the water surface, and vertical thermal stratification), comparison with in-situ measurements suggested that

remotely sensed temperatures were accurate within 0.5 °C, and provided an effective way of determining spatial patterns at a resolution and extent previously unattainable through in-stream data recorders.

The successful development of high spatial resolution and multi-spectral detectors, such as NASA's MODIS/ASTER Airborne Simulator (MASTER) [Hook et al., 2000], Advanced Space borne Thermal Emission and Reflection Radiometer (ASTER) on the EOS-Terra platform and Landsat 7, has increased the utility and availability of TIR imagery (Table 3). These sensors provide new opportunities for remote recovery of stream and lake temperatures. MASTER's high spatial resolution (5-15 m) and 10 thermal infrared (TIR) bands (7.94-13.05 μm) make it an ideal sensor for evaluating the ability of remote sensing to estimate water temperatures. While satellite data have lower spatial and spectral resolution in the TIR, they are more widely available. ASTER has 5 TIR bands (8.3 – 11.3 μm) at 90 m resolution, while Landsat 7 has only one thermal band (11.3 μm effective center) at 60 m resolution.

Before TIR data are widely used to estimate water temperature, the accuracy radiant temperatures obtained from fully resolved stream and lake pixels must be evaluated. I use MASTER (5 and 15 m spatial resolution), ASTER, and Landsat7 TIR data to compare radiant temperatures of fully resolved lakes and streams to concurrent radiant and kinetic temperature ground-truth. I develop strategies to remove emissivity, atmospheric, and surface effects that satisfy simple physical tests such as comparison with ground-truth data, consistency across flight lines, and consistency across detector bands. I then place limits on the influence of these effects on our data, and provide recommendations for the use of TIR data to monitor regional water temperatures.

2. Background

Radiant temperature estimation from TIR remote sensing:

The radiance measured at a remote sensor [$L_s(x,\lambda)$] includes transmitted land-leaving radiance, composed of target-emitted radiance $L_g(x,\lambda)$ and reflected down-welling sky radiance, and up-welling radiance emitted by the atmosphere $L_p(x,\lambda)$. Fortunately, thermal reflectivities of water are low (1-2%) (http://speclib.jpl.nasa.gov/) so unless air temperatures are much higher than water temperatures, land-leaving radiance is relatively insensitive to down-welling sky radiance. The attenuation of the land-leaving radiance by atmospheric gases is modeled by a multiplicative transmissivity $\tau(x,\lambda)$. Thus, water-emitted radiance can be recovered at a specific location (x) at a particular wavelength (λ) using Equation 1.

$$L_g(x,\lambda) = \frac{L_s(x,\lambda) - L_p(x,\lambda)}{\tau(x,\lambda)} \quad (1)$$

where:

L_g = land-leaving radiance ($Wm^{-2}\mu m^{-1}sr^{-1}$)

L_s = sensor radiance ($Wm^{-2}\mu m^{-1}sr^{-1}$)

L_p = path radiance ($Wm^{-2}\mu m^{-1}sr^{-1}$)

τ = transmissivity (unitless)

If emissivity (ε) can be estimated, Planck's equation can be used to relate the radiance emitted by a stream or lake to its radiant temperature (Equation 2).

$$T_k(x,\lambda) = \frac{c_2}{\lambda \ln\left[\frac{c_1\varepsilon}{\pi\lambda^5 L_g(x,\lambda)} + 1\right]} \quad (2)$$

where:

$c_1 = 3.74151*10^8$

$c_2 = 1.43879*10^4$

λ = band effective center wavelength (μm)

L_g = land-leaving radiance ($Wm^{-2}\mu m^{-1}sr^{-1}$)

If atmospheric and emissivity effects are removed, the radiant temperature recovered from remotely sensed data is equivalent to the kinetic temperature of the top ~100 μm of the water surface. Where sub-pixel mixing occurs, spectral un-mixing (e.g., with ASTER or Landsat 7's higher resolution bands) can be used to isolate the fraction of the land-leaving radiance attributed to streams or lakes (Gillespie, 1992).

Emissivity:

Significant errors in remotely sensed temperatures can result from not accounting for the spectrally variant target emissivity. While water is often assumed to be a blackbody (ε=1), its emissivity has spectral variability, and may change with surface roughness, and sediment/vegetation load. Rough water surfaces, especially at off-nadir viewing geometries, may have a higher emissivity and appear slightly warmer than placid water surfaces at the same temperature (Torgerson, 2001). Laboratory measurements of reflectivity (related to ε by Kirchhoff's Law) show that suspended sediment in water can influence emissivity (Salisbury and D'Aria, 1992). While these measurements showed limited spectral contrast for small particles near the water's surface, larger grains brought to the surface by currents, or the accumulation of wind-blown sediment, decreased emissivity by 0.01. In addition, suspended quartz grains with distinct reststrahlen bands had a greater effect on reflectivity than suspended clay-rich soil (Salisbury and D'Aria, 1992).

Atmospheric Correction (AC):

Accurate estimation of temperatures from thermal infrared (TIR) remote-sensing data requires thorough consideration and removal of atmospheric effects.

As shown in Equation (1), AC is accomplished with a multiplicative transmissivity (τ) term that accounts for attenuation of land-leaving radiation due to absorption and scattering by atmospheric gases (primarily water vapor but also ozone and carbon dioxide), and an additive path-radiance term (L_p) that accounts for up-welling atmospheric emitted radiance. Simple sensitivity studies demonstrate the importance of AC for remotely sensed temperature estimates. Assuming typical mid-latitude summer conditions, either a 1.2% increase in τ or a 0.11 $Wm^{-2}sr^{-1}\mu m^{-1}$ increase in L_p resulted in approximately a 1 °C decrease in calculated temperature.

In general, AC coefficients (τ, L_p) are a function of two main factors: path length from the target to the detector, and horizontal and vertical variability in atmospheric temperature and composition. Path length is determined by sensor height, target elevation and view angle off nadir. While ozone has an absorption feature between 9-10 μm and carbon dioxide has strong absorption features on the edges of the atmospheric window (<8 μm, >13 μm), water is the primary absorber in the atmospheric window. For most cases, atmospheric variability is much greater vertically than it is horizontally. Thus, in the TIR, AC coefficients are primarily determined by path length and the locally invariant vertical structure of atmospheric water vapor and temperature.

As atmospheric compensation is essential to most remote-sensing studies, the remote-sensing community has developed numerous empirical and direct AC methods that incorporate physically based radiative-transfer models, ground-truth data, and in-scene information. For spectral analysis, techniques that rely on in-scene radiance differences to predict and remove relative atmospheric effects are often adequate [e.g., Johnson (1998), Young (1998)]. Although radiative-transfer models are used to set the absolute magnitude of atmospheric effects, these techniques use in-scene regressions to predict the spectral shape of the correction. For quantitative temperature estimation, removing relative atmospheric effects refines precision across bands, but does not provide accuracy. Thus, radiative-transfer modeling, or deriving empirical relationships to ground-truth temperatures, is required to estimate temperatures. For example, sea-surface temperature (SST) recovery schemes use split-window or multi-window atmospheric-correction

techniques (Kidder and Vonder, 1995). In these techniques, atmospheric effects are removed using empirical relationships with in-situ buoys, and brightness temperature differences between “dirty” (strong absorption) and “clean” (weaker absorption) bands. Limitations of these techniques include high sensitivity to system noise and errors in spectral emissivity, and the requirement of a ground-truth temperature network (Palluconi et al., 1999). To get around these limitations, many researchers [e.g., Schott (2001), Palluconi et al. (1999)] use the radiative-transfer model MODerate resolution TRANsmission (MODTRAN) (Anderson et al., 1998) to predict and remove atmospheric effects. However, effective removal of atmospheric effects using MODTRAN requires adequate atmospheric control and detailed knowledge of the detector spectral response function.

While carbon dioxide and ozone absorb radiation in the TIR, water vapor is the strongest absorber in the TIR atmospheric window. Therefore, estimates of the vertical distribution of water vapor and temperature are important inputs to any radiative-transfer calculation for AC of TIR remote-sensing data. Ground-based measurements and numerical weather models can constrain MODTRAN simulations and help remove atmospheric effects. Radiosondes measure the vertical distribution of water vapor and temperature. Data from NOAA operational radiosondes provide useful estimates of temperature and water-vapor distribution when they are temporally concurrent and close to the location where remote-sensing measurements were taken. Microtops II (microtops), developed by Solar Light Co., estimates total column water (TCW) in cm using differential absorption between radiance measurements that experience strong (0. 940 μm) and weak (1.020 μm) water absorption.

Numerical weather simulations are an important, generally available, source of estimated water-vapor and temperature profiles. Forecasts are often assimilated with atmospheric observations (e.g., satellite sounder data, radiosonde, surface measurements) to produce physically consistent re-analysis data. NCAR has two models available: the 209 km resolution NCEP re-analysis product and the 40-km resolution Eta-29 mesoscale model. In the Pacific Northwest, forecasts from the Penn State/NCAR mesoscale model (MM5) maintained by the National Center for

Atmospheric Research, Mesoscale and Microscale Meteorology Division (NCAR/MMM), are produced twice daily at the University of Washington Department of Atmospheric Sciences (http://www.atmos.washington.edu/mm5rt/). This research-oriented model estimates TCW and vertical distributions of water vapor and temperature every hour, at 4-km spatial resolution.

Gao and Goetz [1990] promoted the idea that the relative absorption between a weak and strong water absorption band can be used to estimate water-vapor content, and atmospherically correct remote-sensing data without concurrent ground truth. Many in-scene AC algorithms are based on this idea that in-scene information can be used to predict atmospheric conditions. However, it should be noted that in the end, all of these methods still require a radiative-transfer model to estimate the magnitude of AC. Atmospheric CORrection Now (ACORN) (http://www.aigllc.com/acorn/intro.asp) and AAC [Gu et al., 2000] are examples of in-scene techniques that use radiances to predict water-vapor content, and remove atmospheric effects with MODTRAN. ACORN can be used on hyper-spectral or multi-spectral data between 0.35 μm and 2.5 μm, while AAC is designed to correct hyper-spectral data in the TIR. ACORN is available as a plug-in to the widely used image-processing software ENVI (Research Systems Inc., 2001). For hyper-spectral data, ACORN uses full spectral water-vapor fitting at the 0.94 μm or 1.14 μm water-absorption bands to estimate water-vapor amounts. For multi-spectral data (e.g., Landsat 7), limited spectral coverage and resolution limit ACORN's spectral water-vapor fitting technique, so water-vapor amount must be specified by the user. After water-vapor amount has been determined, the user must specify a model atmosphere and visibility. Then, a MODTRAN correction is selected from a look-up table and the data are compensated. Autonomous Atmospheric Correction (AAC) [Gu et al., 2000] uses a strong water absorption feature at 11.73 μm to define two atmospheric index parameters (transmittance ratio and path-radiance difference) that measure the strength of atmospheric transmission and emission. An empirical relationship of these parameters with MODTRAN simulations is then used to select a MODTRAN radiative-transfer calculation for AC.

Before AC can be applied to remote-sensing data, MODTRAN's predictions for transmission and emission must be spectrally convolved to the filter function of each TIR band. As atmospheric absorption features are discrete and wavelength dependent, accurate description of the filter function of the detector is important. Small shifts in a detector's filter function may result in large changes in the spectrally resampled MODTRAN output. In general, accurate filter function calibration might be a fundamental barrier to AC of hyper-spectral TIR data with line-by-line radiative-transfer models.

Surface Effects:

Surface effects can have significant effects on the radiant temperatures of streams and lakes. These effects include multiple scattering (radiation emitted and scattered multiple times by adjacent scene elements), wind-driven evaporative cooling, and preferential heating of the surface skin in stagnant water. For TIR observations of water, multiple scattering can artificially increase radiant temperatures at grazing viewing geometries and will be especially important where the forest canopy overhangs the bank of a stream or lake. For example, Kay et al. (2001) estimated the radiance attributable to this path with a theoretical radiosity thought experiment. With a geometrical argument, they show that no more than 25% of the radiation emitted by adjacent vegetation will reach the water's surface. By assuming emissivities for water and vegetation from the ASTER spectral library laboratory spectra and typical summer radiant temperatures for adjacent vegetation and the stream, they calculate a 0.11 $Wm^{-2}sr^{-1}\mu m^{-1}$ increase in land-leaving radiance and a corresponding 0.4 °C increase in calculated radiant temperature.

3. Data and Methods:

In August 2001, MASTER, ASTER, and Landsat7 data were collected over the Green River and several near-by lakes south of Seattle, WA, USA (Figure 19, Table 4). These data provide radiant temperature measurements of lakes and streams at a variety of viewing geometries and atmospheric conditions. Concurrent microtops observations, kinetic ($T_{kinetic\text{-}surface}$) and radiant ($T_{radiant\text{-}surface}$) surface

temperature measurements, and a network of in-stream and in-lake gages ($T_{kinetic-gage}$) provided control for MODTRAN simulations, and water temperatures. Stream and lake ground-truth data was screened for inconsistencies and variability. Where only a single measured value was taken, or measurements were more than 10 minutes away from remote sensing data collection, these values were flagged as "questionable". Where measured values varied by more than a degree within 30 minutes, these values were flagged as "variable". In the end, only persistent (varying by < 1 °C in 30 minutes) and concurrent (within 10 minutes of overpass) were used for emissivity correction (EC) and atmospheric correction (AC) evaluation. Error was attributed to measurements in using a subjective, but consistent, methodology. If the measurement was taken concurrent with data collection and showed persistence within a degree, estimated error was the sum of the detector sensitivity (0.1 °C for $T_{kinetic-surface}$, 0.5 °C for $T_{radiant-surface}$) and the standard deviation in the measurements. If the measurement was not taken concurrent with data collection, the closest possible time was selected and the estimated error was the sum of the detector sensitivity and the largest deviation over the observation period.

The reflectance of distilled water (http://speclib.jpl.nasa.gov/) was related to the emissivity using Kirchoff's Law (e=1-r) and convolved to each sensor's spectral response function. The convolved emissivities for each band were then applied as an emissivity correction (EC) (Figure 20).

Atmospheric correction was accomplished with TIR radiative-transfer calculations from a PC version of MODTRAN [PcModWin 4.0 (Ontar Corporation, 2001)]. As water vapor is the strongest absorber in the TIR, a wide variety of atmospheric data was assimilated including: concurrent TCW observations from Microtops, NOAA radiosonde data from Spokane and Quillayute, MM5 predictions for TCW and water-vapor/temperature profiles, and MODTRAN's standard mid-latitude summer atmosphere. MODTRAN simulations of atmospheric transmission and emission were completed with TCW ranging from 0.5 – 3.0 gm/cm^3 and profile data (Appendix B,C&D). In these simulations, ground elevation was set to either Flaming Geyser State Park (0.056 km) or Lake Sawyer/Lake Youngs (0.1524 km), while sensor elevation was set to 2 km for MASTER 5m, 6 km for MASTER 15 m,

and 100 km (top of atmosphere) for ASTER and Landsat7. MODTRAN outputs were then convolved with each sensor's filter functions to estimate band-specific τ and L_p. Simulated temperature spectra were created at a range of target temperatures to aid in the interpretation of at-sensor temperature profiles and to reveal which MASTER and ASTER bands are most sensitive to EC and AC. Then, EC and AC were applied to MASTER/ASTER/Landsat7 data for regions of interest (ROI) on Lake Youngs, Lake Meridian, Lake Sawyer, and along on the Green River near Flaming Geyser State Park using equation (1). Finally, remotely sensed radiant temperature (T_{rs}) was calculated with equation (2) using no correction, EC only, and EC and a range of AC.

T_{rs} estimates were then evaluated for each flight line on each day using four physically based criteria. First, the MODTRAN atmospheric parameterization had to be in reasonable agreement with the atmospheric ground-truth. Second, image-derived radiant temperatures should be consistent with in-situ ground-truth data ($T_{radiant\text{-}surface}$, $T_{kinetic\text{-}surface}$, and $T_{kinetic\text{-}gage}$). Third, after removal of atmospheric and emissivity effects, all bands should predict similar temperatures within the noise and radiometric calibration errors ("spectral flatness"). As the bands on the edges of the atmospheric window are most affected by absorption, the raw data often show a concave-downward shape across wavelength. Over-compensating for absorption leads to a concave-upward shape across the TIR window. Thus, although bands sensitive to EC and AC are not used for estimation of temperature, they aid in evaluation of EC and AC. Finally, the AC selected for each scene must be consistent with other flight lines flown at similar viewing geometries at similar times.

The Hybrid Atmospheric Correction (HAC) method, developed from ISAC [Johnson, 1998; Young, 1998] by Kay et al. (2001), was used to test the utility of relative corrections for temperature recovery. The underlying assumption of HAC is that atmospheric conditions derived from an in-scene technique may better reflect the relative difference in atmospheric effects than a radiative-transfer model. However, the radiative-transfer model is still required to set the absolute magnitude of the correction. The in-scene portion of the HAC method makes two assumptions. First, a scene must contain a material with both a known emissivity (preferably a gray

or black body) and a distribution of brightness temperatures. Kay et al. suggest vegetation as it can be approximated as a blackbody in the TIR (Salisbury and D'Aria, 1992) and its variability in shading will provide the necessary distribution of brightness temperatures. Second, the HAC method assumes that if atmospheric effects and emissivity are removed, Planck's equation will predict the same temperature in all bands (within the noise equivalent change in temperature - NEΔT).

Given these assumptions, the HAC method can be implemented. Bands that are visibly noisy or of known poor quality are excluded. Grey or black body region of interest (ROI) pixels are selected. Then, for each ROI pixel, TIR radiance is used to calculate a brightness temperature for all bands. Next, the ROI brightness temperatures in each band are used as a reference to describe the relative atmospheric effects in all other bands. Three steps are required to make these relative predictions for every reference band: 1) For each pixel, the brightness temperatures of the reference band are used to predict radiance in all other bands. 2) For every combination of non-reference bands, the predicted radiance for all ROI pixels (dependent variable) is plotted against the observed radiance for all ROI pixels (independent variable). The slope and offset of these regression lines correspond to the relative τ and L_p for the two plotted non-reference bands. 3) Combining these regressions, one can plot the relative transmissivities and path radiances versus wavelength for all non-reference bands based on each reference band. Finally, the curves from each reference band are shifted and averaged to define one curve that describes how AC varies across bands. The HAC method only describes the relative differences between bands, not the magnitude of actual atmospheric coefficients. Thus, a radiative-transfer model is used to fix the magnitude of the AC.

Multiple scattering and wind effects were estimated with ground-based radiant temperature measurements of the surface of water bodies. To assess the effects of multiple scattering in the near-bank environment of streams, I used a ground-based FLIR (Forward Looking Infrared Radiometer) to take thermal images (1 band, 10.149-11.449 μm) of the Green River at Flaming Geyser State Park (near GR4). Our main objective was to investigate how multiple scattering of near-bank radiation affected the observed radiant temperature of the water. Radiometric

calibration was achieved by taking thermal images of targets with measured radiant temperatures. Linear regressions were then used to relate measured values to emitted radiance. To assess the effects of wind on radiant temperatures, relative wind observations were taken during all lake $T_{radiant-surface}$ measurements.

4. Results:

Simulated MODTRAN Temperatures for a range of TCW and target temperatures:

Example recovered temperatures in MASTER and ASTER bands were simulated for a range of TCW and the emissivity of distilled water (Figure 21,22,&23). These plots reveal MODTRAN's predictions for the interplay between additive and multiplicative corrections at different sensor elevations, target temperatures, and wavelengths. While increasing absorption (i.e., decreasing transmissivity), and decreasing emissivity, cause at-sensor radiant temperatures to be lower than true temperatures, increasing emission (i.e., increasing path radiance) causes at-sensor radiant temperatures to exceed true temperatures. In other words, emissivity correction (EC) will always raise uncorrected radiant temperatures, but the effect of atmospheric correction (AC) depends on the relative magnitude of absorption (transmissivity) and emission (path radiance). In 5m MASTER data (Figure 21), target temperatures determine the combined effect of EC and AC. For example, at 12 °C (Figure 21a), emitted path radiance exceeds atmospheric absorption. Therefore, the overall effect of EC and AC is a decrease in uncorrected radiant temperatures. At 16 °C (Figure 21b), the overall effect of AC is negligible as atmospheric absorption and emission are nearly balanced. Together, while AC and EC increase uncorrected radiant temperatures, this change is primarily due to EC. At 20 °C (Figure 21c), absorption dominates atmospheric effects so both AC and EC will increase uncorrected radiant temperatures. In the 15m MASTER data, absorption dominates atmospheric effects at 16 °C (Figure 22a) and 20 °C (Figure 22b), so both EC and AC increase uncorrected radiant temperatures. However, at 12 °C (Figure 22c), the sign of the combined effect of AC and EC is wavelength

dependent. The top of atmosphere MODTRAN simulations (ASTER and Landsat7) are similar to the 15m MASTER simulations, with different band placements (Figure 23a-c). Absorption dominates, leading to positive AC and EC corrections on uncorrected radiant temperatures in all but the 12 °C case.

Selection of AC from MODTRAN Runs:

Atmospheric corrections were selected from the MODTRAN output based on four criteria: 1) agreement with atmospheric assimilation data 2) agreement with radiant, surface kinetic, and gage kinetic ground-truth temperatures ($T_{radiant\text{-}surface}$, $T_{kinetic\text{-}surface}$, and $T_{kinetic\text{-}gage}$) 3) spectral flatness (i.e., low standard deviation across bands) and 4) agreement across flight lines (Table 5). The effect of EC and AC was evaluated by examining differences in mean temperature and standard deviation across bands (Figure 24a&b, Figure 25a&b). Mean temperatures were calculated in bands least sensitive to atmospheric, emissivity, and noise effects (MASTER - B43, B44, B46, B47 and B48 ASTER - B13 and B14), whereas standard deviation across bands was calculated across for bands not severely affected by instrument noise (Bands 42-48 for MASTER, B10-B14 for ASTER). EC always increases uncorrected radiant temperatures by 0.6 - 0.9 °C. While AC generally increased uncorrected radiant temperatures (max 2.0 °C), Green River temperatures in 5m MASTER data decreased (-0.2 °C). EC did not significantly change the standard deviation in temperature across bands. In all but the 5m MASTER data, AC improved standard deviation in temperature across bands.

Atmospheric Parameterization:

Though there was significant variability in all TCW estimates (Table 6), MM5 provided the most consistent and reliable predictions for local TCW. In seven direct comparisons between radiosonde and MM5 data, the average difference in TCW was 0.3 ± 0.2 cm. This suggests that MM5 is a reasonable source for TCW estimates when radiosondes data are not available. For example, on August 25, 2001, TCW estimates ranged from 1.1 to 3.4 g/cm^2 for microtops, MM5, NOAA radiosondes, and MODTRAN's mid-latitude summer standard atmosphere (Figure 26). Microtops

observations were always the lowest of all estimations of TCW. In an ASTER validation experiment in Hawaii, the University of Washington microtops gave systematically low TCW when compared with two other microtops from JPL and Los Alamos (A. Gillespie, personal communication, 2001). Deviation of microtops and MM5 TCW estimates may be explained by unconstrained microtops calibration problems. TCW from NOAA radiosondes were limited to Spokane (1.6 gcm^{-2}) and Quillayute (2.8 gcm^{-2}) at 4:00 PM PST. Regional variability in water-vapor content, and the lack of concurrent timing may explain why these data deviate from other TCW data. TCW predictions from the mid-latitude standard atmosphere exceeded all microtops, MM5, and radiosonde estimates. Thus, the mid-latitude summer standard atmosphere is a poor measure of TCW in western Washington.

August 25, 2001 - 5m and 15m MASTER

For the 5m MASTER lines flown on August 25, 2001, the two-cm TCW MODTRAN runs provided the most consistency with the four criteria. Two-cm TCW is close to the MM5 estimate for water vapor during all of these overpasses. Examples from multiple 5 m flight lines at Lake Meridian, Lake Sawyer, and the Green River show that while AC generally improved agreement between T_{rs} and ground-truth temperatures, spectral flatness was not improved. At Lake Meridian (Figure 27), the corrected T_{rs} (21.5 °C) was within 0.3 °C of concurrent ground-truth data ($T_{radiant\text{-}surface}$ = 21.5 ± 0.5 °C, $T_{kinetic\text{-}surface}$ = 21.5 ± 0.3 °C, $T_{kinetic\text{-}gage}$ = 21.2 ± 0.3 °C). Here, EC and AC increased uncorrected T_{rs} (19.7 °C) by almost 2 °C. While the standard deviation in T_{rs} across the MASTER bands decreased with EC (from 0.8 °C to 0.3 °C), it did not change with the addition of AC (to 0.4 °C). At Lake Sawyer (Figure 28), the corrected T_{rs} (20.9 °C) was more consistent with ground-truth temperatures ($T_{radiant\text{-}surface}$ 21.5 ± 2.0 °C, $T_{kinetic\text{-}surface}$ 21.4 ± 0.4 °C) than the uncorrected T_{rs} (19.2 °C). The standard deviation in T_{rs} across bands was reduced with EC (0.7 °C to 0.3 °C), but increased with AC (0.5 °C). For the Green River (e.g., GR5, Figure 29), corrected T_{rs} (15.6 °C) were higher than ground-truth ($T_{kinetic\text{-}gage}$ = 14.5 ± 0.3 °C, $T_{radiant\text{-}surface}$ = 14 ± 2.0 °C, $T_{kinetic\text{-}surface}$ = 14.8 ± 0.5 °C) temperatures.

At these temperatures, emission-dominated AC slightly reduced T_{rs}. The standard deviation in T_{rs} across bands remained the same with EC (0.4 °C), but increased slightly with EC and AC (0.6 °C).

Two-cm TCW MODTRAN runs were the preferred atmospheric correction for the 15m MASTER data collected on August 25, 2001. Two-cm TCW is close to the MM5 estimate for water vapor during all of these overpasses. Examples from Lake Youngs, Lake Meridian, and the Green River show that AC generally increased agreement between image temperatures and ground-truth temperatures, and decreased standard deviation across bands. At Lake Youngs, the corrected T_{rs} (19.7 °C) was more consistent with ground truth ($T_{kinetic\text{-}gage}$ = 19.5 ± 0.5 °C) than the uncorrected T_{rs} (17.5 °C). Standard deviation in T_{rs} across bands improved primarily as a result of AC (uncorrected 1.0 °C, AC 0.3 °C). The shape of T_{rs} spectra across bands changes from a concave-down shape for uncorrected data to a flat shape for the two-cm TCW MODTRAN runs (Figure 30). The concave-upward shape of the MM5 profile and mid-latitude summer standard atmosphere T_{rs} results from over correction for atmospheric absorption and emission. At Lake Meridian, similar agreement with ground truth and spectral flatness is seen for the two-cm TCW correction (Figure 31). The atmospherically corrected T_{rs} (22.2 °C) was more consistent with ground-truth temperatures ($T_{kinetic\text{-}gage}$ = 21.1 ± 0.3 °C, $T_{radiant\text{-}surface}$ = 21.5 ± 0.5 °C, $T_{kinetic\text{-}surface}$ = 22.4± 0.7°C) than the uncorrected T_{rs} (19.5 °C). AC results in a reduction in standard deviation in T_{rs} across bands from 1.0 °C to 0.5 °C, and a corresponding transition to a flat T_{rs} shape across bands. At the Green River gage GR5 (Figure 32), the corrected T_{rs} (18.9 °C) did not match ground truth ($T_{kinetic\text{-}gage}$ =16.7°C) and standard deviation across bands did not change with AC (no correction: 0.7 °C, EC: 0.6 °C, AC: 0.6 °C).

August 11, 2001- ASTER and Landsat7

AC with 0.75-cm TCW was selected for ASTER and Landsat 7 data collected on August 11, 2001. However, selecting an atmospheric correction that adhered to the four established criteria for all cases was difficult. TCW of 0.75-cm is less than

the microtops data (1.03 cm), and lower than any prediction for TCW for MM5 for the late August dates. However, more TCW created a concave upward temperature spectra shape in all three lakes. At Lake Meridian, AC improves agreement between corrected T_{rs} (24.1 °C) and ground-truth ($T_{kinetic\text{-}gage}$ = 23.4 ± 0.8 °C, $T_{radiant\text{-}surface}$ = 23.6 ± 0.2 °C, $T_{kinetic\text{-}surface}$ = 23.6 ± 0.7°C) for both ASTER and Landsat7 (Table 5, Figure 15). On the other hand, at Lake Sawyer and Lake Youngs, corrected T_{rs} were greater than ground-truth by up to 3 °C (Table 33). In all cases, AC significantly improved standard deviation across bands (e.g., 1.4 °C to 0.2 °C at Lake Meridian, Table 2).

August 27, 2001 – 5m MASTER and Landsat7

The two data sets collected on August 27, 2001 were: high-resolution (5 m), low-altitude (2 km) MASTER data, and low-resolution (60 m), high-altitude (700 km) Landsat 7 data. In the 5m MASTER data for the Green River, all AC (i.e., a range of TCW parameterization in MODTRAN) have the same effect on T_{rs} indicating a balance between emission and absorption for the surface temperature of approximately 16 ºC (Figure 34). The corrected T_{rs} at GR5 (16.4 °C) was greater than the gage ground-truth ($T_{kinetic\text{-}gage}$ =15.4 °C ± 0.2 °C). Lake Meridian and Lake Youngs August 27, 2001 Landsat7 temperatures were as much as 8 °C cooler than concurrent ground truth (Figure 35). At Lake Youngs and Lake Meridian, EC and AC did little to improve agreement with ground truth. While not visible in the VNIR, high cirrus clouds over the field sites may explain the extreme deviations from ground truth. While Lake Sawyer temperatures were closer to ground truth, AC was difficult to evaluate with only one TIR band and inconsistent ground-truth temperatures ($T_{radiant\text{-}surface}$ = 18.5 ± 2.0 °C, $T_{kinetic\text{-}surface}$ = 21.7 ± 0.4 °C).

Hybrid Method Test Case on Lake Youngs

A treed ridge near Lake Meridian (ridge vegetation) and a forest surrounding Lake Youngs (youngs vegetation) were selected as regions of interest for HAC regressions to predict relative differences in atmospheric absorption and emission. Although I avoided bands on the TIR atmospheric window wings, R^2 ranged from 63-

77% for the ridge vegetation and from 35-57% for youngs vegetation. In general, a range of radiant temperatures was required for statistically significant regressions. HAC predictions for T_{rs} were calculated with two-cm TCW, the best atmospheric correction from MODTRAN. HAC atmospheric correction with ridge vegetation differed from MODTRAN by as much as 0.07 for transmissivity estimates, and 0.58 $Wm^2sr^{-1}\mu m^{-1}$ for path radiance estimates (Figure 36a&b). Although the HAC method pulled out a distinct spectral shape that might reflect in-scene emissivity, the retrieved T_{rs} ($T_{HAC\text{-}ridgeveg}$ = 19.6 °C, $T_{HACyoungsveg}$ =19.6°C) were close to the MODTRAN-only corrected T_{rs} ($T_{MODTRAN}$ = 19.4°C) (Figure 37).

Surface effects:

Multiple scattering and wind effects were investigated using ground-based radiant temperature measurements. Calibrated FLIR images and visible images looking down the Green River in Flaming Geyser State Park (FGPS), west of Auburn, WA provided the opportunity to investigate multiple-scattering effects. Co-aligned FLIR and digital camera images looking down the Green River at FGSP showed evidence for multiple-scattering effects (Figure 38a&b). In the FLIR data, a 3 °C increase in the observed radiant temperature in the near-bank environment is attributed to multiple-scattering of radiation from the near-bank environment (trees, rocks) (Figure 38b). Striping patterns on the FLIR stream data are attributed to detector noise whereas patches of warmer stream temperatures in the center result from rocks or logs rising above the water surface. Ground-truth measurements taken with a hand-held radiometer were used to investigate wind effects. On August 25, 2001 at Lake Sawyer, large deviations in $T_{radiant\text{-}surface}$ measurements (up to 3.5 ºC) were observed while taking ground-truth radiant temperature measurements (Figure 39). These deviations are attributed to wind gusts; however, detector stability is poorly understood and could be an alternate explanation.

Comparison of image temperatures with concurrent ground-truth temperatures:

Comparison of corrected and uncorrected remotely sensed data with concurrent and persistent ground truth ($T_{radiant-surface}$, $T_{kinetic-surface}$, and $T_{kinetic-gage}$) supports atmospheric correction (Table 7, Table 8, and Figures 40a-f). However, consistent agreement between corrected radiant temperatures, and all gage and non-concurrent or persistent ground-truth data, is less evident.

Without correction, all remotely sensed radiant temperatures (T_{rs}) were within 3.0 ° C of concurrent and persistent ground truth, including $T_{radiant-surface}$, $T_{kinetic-surface}$, and $T_{kinetic-gage}$ measurements. $T_{kinetic-surface}$ and $T_{radiant-surface}$ ground-truth temperatures were often greater than uncorrected T_{rs}, and none were within 1°C of uncorrected T_{rs}. The average median deviation of T_{rs} and ground truth for all data (MASTER 5m, MASTER 15m, ASTER and Landsat 7) was -1.6 °C for $T_{kinetic-surface}$ ground-truth and -1.7 °C for radiant ground truth. 59% of $T_{kinetic-gage}$ measurements were within 1 °C of uncorrected T_{rs}. Along the Green River, all $T_{kinetic-gage}$ were within 1 °C of T_{rs}, while the lakes $T_{kinetic-gage}$ were all within 2.2 °C T_{rs}.

With correction (AC and EC), all T_{rs} were all within 2.5 ° C of persistent and consistent $T_{radiant-surface}$, $T_{kinetic-surface}$, and $T_{kinetic-gage}$ ground truth. While agreement of T_{rs} with $T_{radiant-surface}$ and $T_{kinetic-surface}$ ground truth generally improved, corrected T_{rs} often exceeded $T_{kinetic-gage}$. The percentage of $T_{radiant-surface}$ and $T_{kinetic-surface}$ within 1 °C of T_{rs} increased with correction from 0% to 100% (3 measurements), and 0% to 75% (8 measurements) respectively. With the exception of one measurement at Lake Sawyer, the maximum deviation of $T_{kinetic-surface}$ was 0.5 °C, while the maximum deviation for $T_{radiant-surface}$ was 0.7 °C. The percentage of $T_{kinetic-gage}$ (17 measurements) within 1 °C of T_{rs} decreased from 59% with the uncorrected T_{rs} to 47% with the corrected T_{rs}. EC and AC increased agreement between corrected T_{rs} and ground truth at Lake Meridian and Lake Youngs data, but decreased agreement at Lake Sawyer and along the Green River.

5. Discussion:

Emissivity, atmospheric, and surface effects had varying degrees of import for the data collected in this study. The impact of these effects, including important factors to consider in evaluation of future data, is summarized in Table 9. Evaluating the accuracy of remotely sensed radiant temperature measurements requires a standard for comparison. Unfortunately, accurate radiant temperature measurements are difficult to make because of changing environmental factors (e.g., wind), and the high expense of calibrating and maintaining instrumentation. In an imperfect world, where accurate radiant ground-truth is unavailable, having several independent checks on corrected remotely sensed temperatures is essential. I established four criteria to evaluate the effects of EC and AC that can be used with any set of TIR data: credible atmospheric parameterization in MODTRAN, agreement with $T_{radiant\text{-}surface}$, $T_{kinetic\text{-}surface}$, and $T_{kinetic\text{-}gage}$ ground-truth temperatures, spectral flatness (i.e., low standard deviation across bands), and agreement across flight lines.

MODTRAN predictions for atmospheric absorption and emission are limited by the accuracy of atmospheric water vapor and temperature parameterization, and the filter function of TIR detectors. Atmospheric parameterization with calibrated in-situ measurements, or from high-resolution atmospheric models is preferred. If these data are not available, climatology specific to study site should be used. In the study areas examined, using the standard mid-latitude summer atmosphere to predict atmospheric effects does more harm than good. Uncorrected temperatures were often closer to ground-truth, and had smaller standard deviation across bands, than temperatures corrected with a standard atmosphere.

Evaluation of EC and AC performance with concurrent and persistent ground-truth temperature data is important. However, if ground-truth data are of poor quality, vary wildly with environmental factors (e.g., wind), or are not surface measurements, they are not useful for evaluation of the accuracy of remotely sensed temperatures. If all radiant and kinetic ground-truth data are used for evaluation, EC and AC appear to do little to improve agreement between remotely sensed and ground-truth temperature data. However, EC and AC significantly increased

agreement between remotely sensed temperatures and persistent, concurrent, radiant and surface kinetic temperature measurements. In some cases, agreement between uncorrected radiant temperatures and gage temperatures probably resulted from compensating atmospheric and surface effects. As gages measurements are taken at depth, the water temperature a gage estimates might be cooler than a surface temperature measurement. Deviations of the 15m Green River data from gage data might be partially explained by sub-pixel mixing with rocks and vegetation. Careful selection of water-only pixels, or spectral mixing analysis might improve agreement between ground-truth and remotely sensed temperatures.

One clear advantage of multi-spectral data for temperature estimation is that spectral flatness can be used as an independent check on EC and AC. Although data in bands with large atmospheric effects were not used to calculate temperatures, they were useful for evaluating and constraining the ability of MODTRAN to simulate atmospheric absorption and emission.

TIR remote sensing is a powerful way to quantitatively estimate the spatial distributions of water temperatures. However, the limitations of remotely sensed temperature measurements for environmental monitoring and hydrological modeling depend on the required accuracy and application. Accurate remotely sensed temperatures are measurements of surface radiant temperature. They are affected by different environmental factors than bulk temperature measurements (i.e., emissivity, atmospheric absorption and emission, and surface effects such as wind or multiple scattering). In some cases, confusing compensating errors can result in agreement between ground-truth and uncorrected remotely sensed temperatures. Estimating bulk kinetic temperature with accuracy of 1 °C is only possible when remotely sensed data have minimal emissivity, atmospheric, and surface effects. In our experience, these effects require extensive processing to separate, and are difficult, if not impossible, to remove.

In the end, this research demonstrates that with EC and AC, satellite and airborne remote-sensing data can estimate the radiant and surface kinetic temperature of lakes with sub-degree accuracy. However, the lack of accurate ground-truth measurements illustrates the importance of other independent criteria

(i.e., spectral flatness) for evaluating radiant temperatures. For streams, remote sensing of temperature is more difficult. Even at 15 m resolution, sub-pixel mixing may limit the accuracy of remotely sensed radiant temperature measurements. This suggests the importance of using "pure" water pixels for temperature estimation from TIR data.

5. Conclusion:

Thermal-infrared (TIR) remote sensing can be used to estimate the radiant temperature of water bodies that have environmental and economic import. However, the accuracy of radiant temperature measurements depends on adequate compensation for emissivity, atmospheric, surface effects (e.g., wind, multiple scattering), and sub-pixel mixing. I use the emissivity of distilled water, MODTRAN simulations of atmospheric effects, and concurrent radiant, surface kinetic and gage kinetic temperatures to understand the limitations of airborne and satellite TIR data in predicting water temperatures. In addition to agreement with concurrent and persistent surface temperature measurements, spectral flatness, water-vapor ground truth, and consistency across flight lines are used as independent checks on emissivity and atmospheric corrections. After correction, the majority of remotely sensed lake temperatures were within 1 °C of radiant and kinetic ground-truth measurements. On the other hand, remotely sensed stream temperatures deviated by up to 2.3 °C from gage measurements due to surface and sub-pixel mixing effects. In summary, TIR remote-sensing data can estimate radiant water temperature with degree accuracy when emissivity and atmospheric effects have been removed, and when there are minimal surface, and sub-pixel mixing effects.

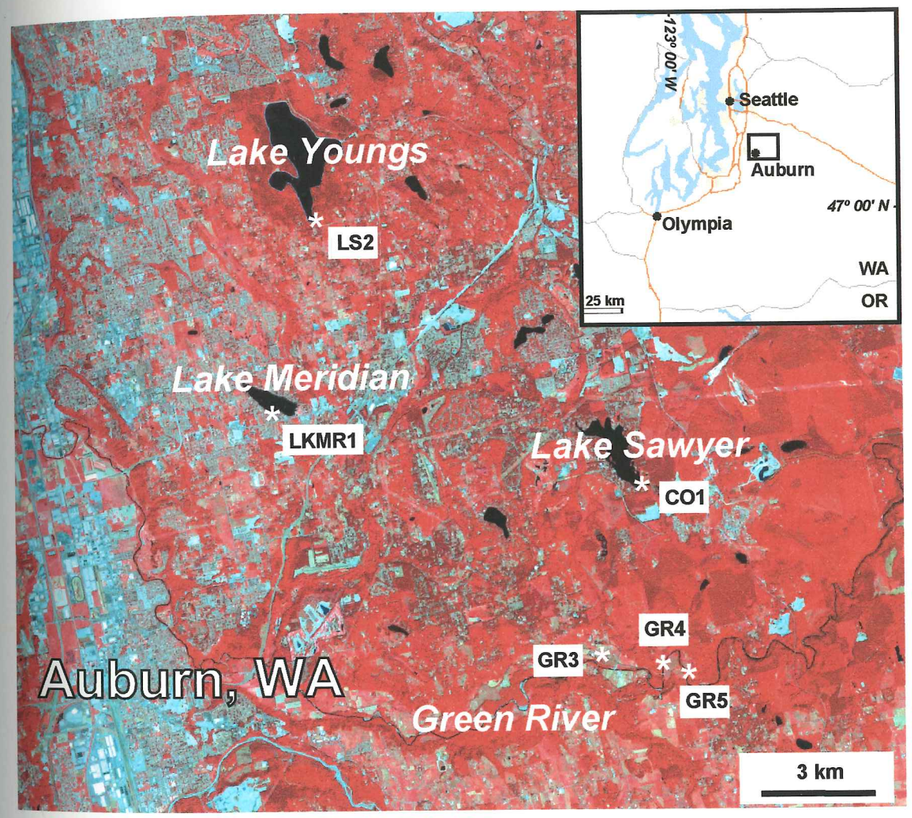

Figure 1. Location Map for TIR Lake and Stream Data

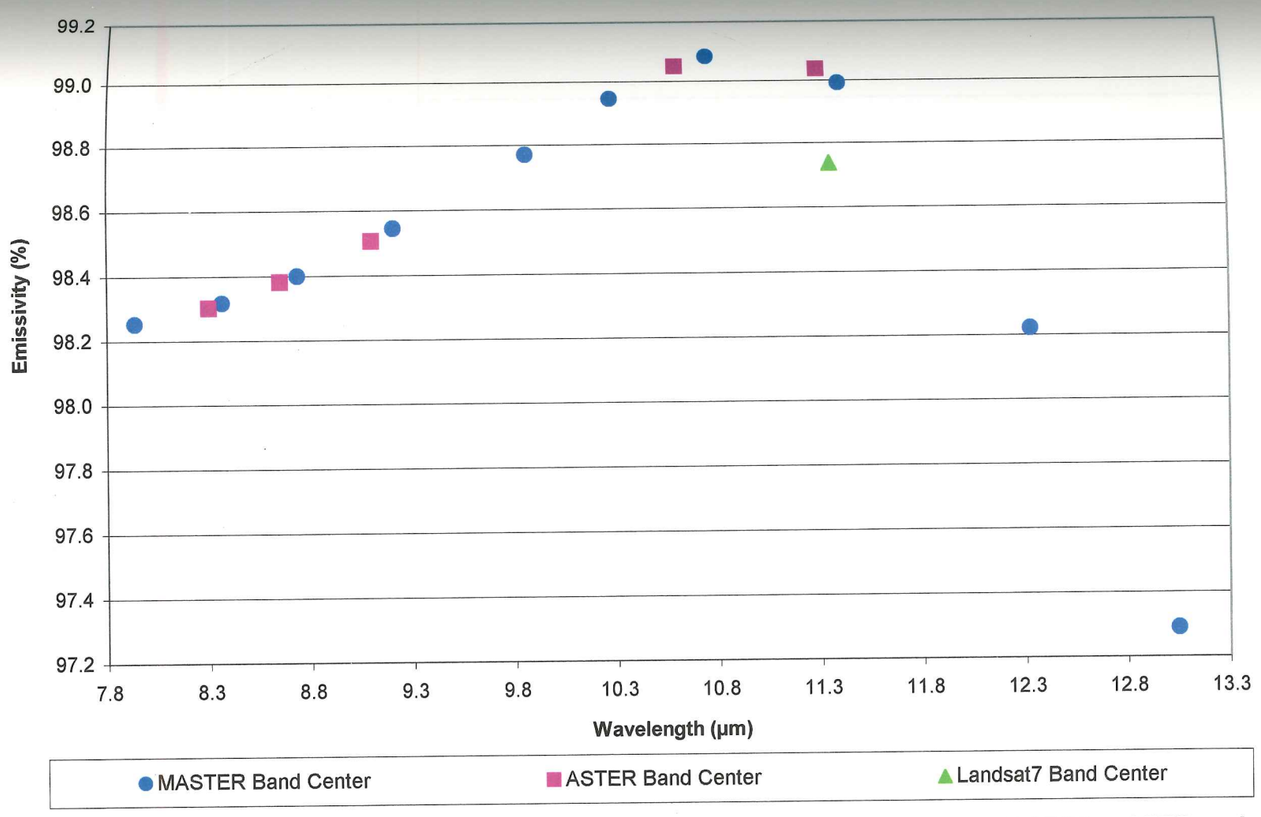

Figure 20. Emissivity of Distilled Water *(http://speclib.jpl.nasa.gov/)* Convolved to MASTER, ASTER and Landsat 7 TIR Bands

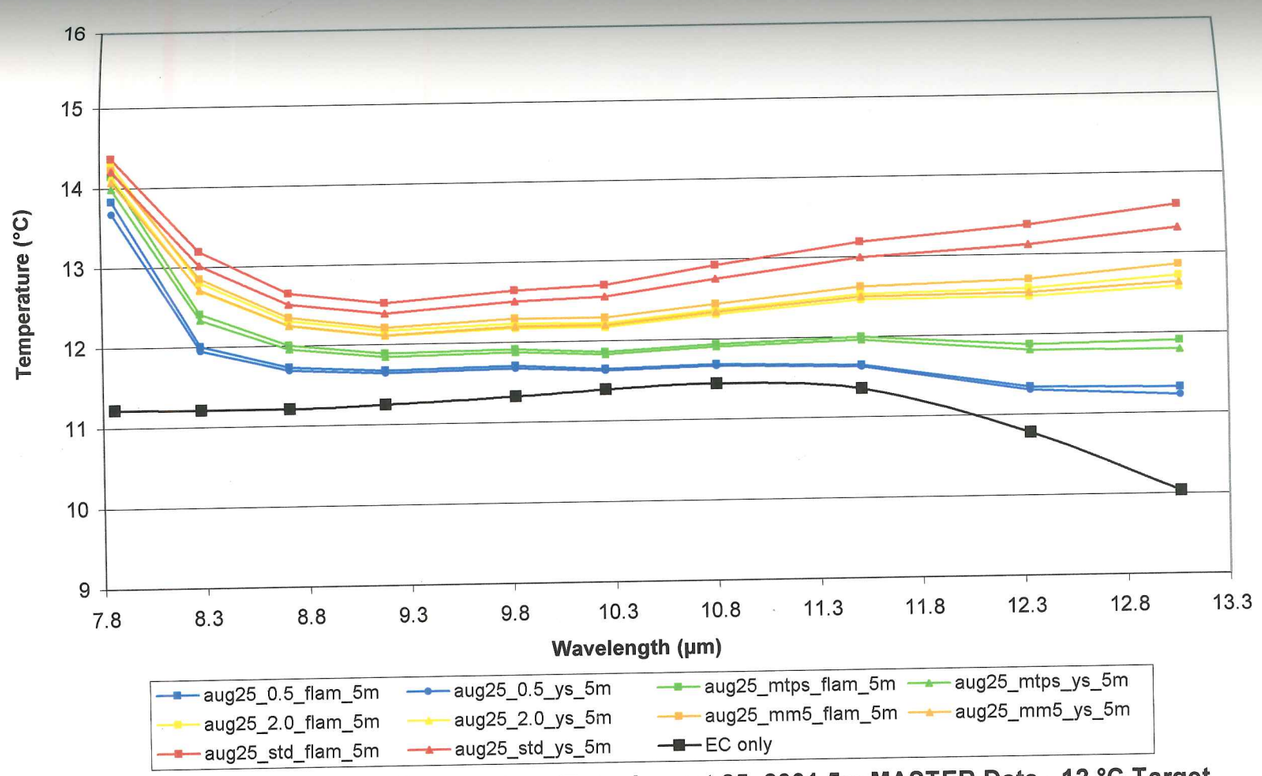

Figure 21a. Simulated At-Sensor Temperature (T_{rs}) - August 25, 2001 5m MASTER Data - 12 °C Target with EC and a Range of MODTRAN AC (Appendix I.) T_{rs} were simulated for Flaming Geyser State Park (flam) and Lake Youngs/Lake Sawyer (ys).

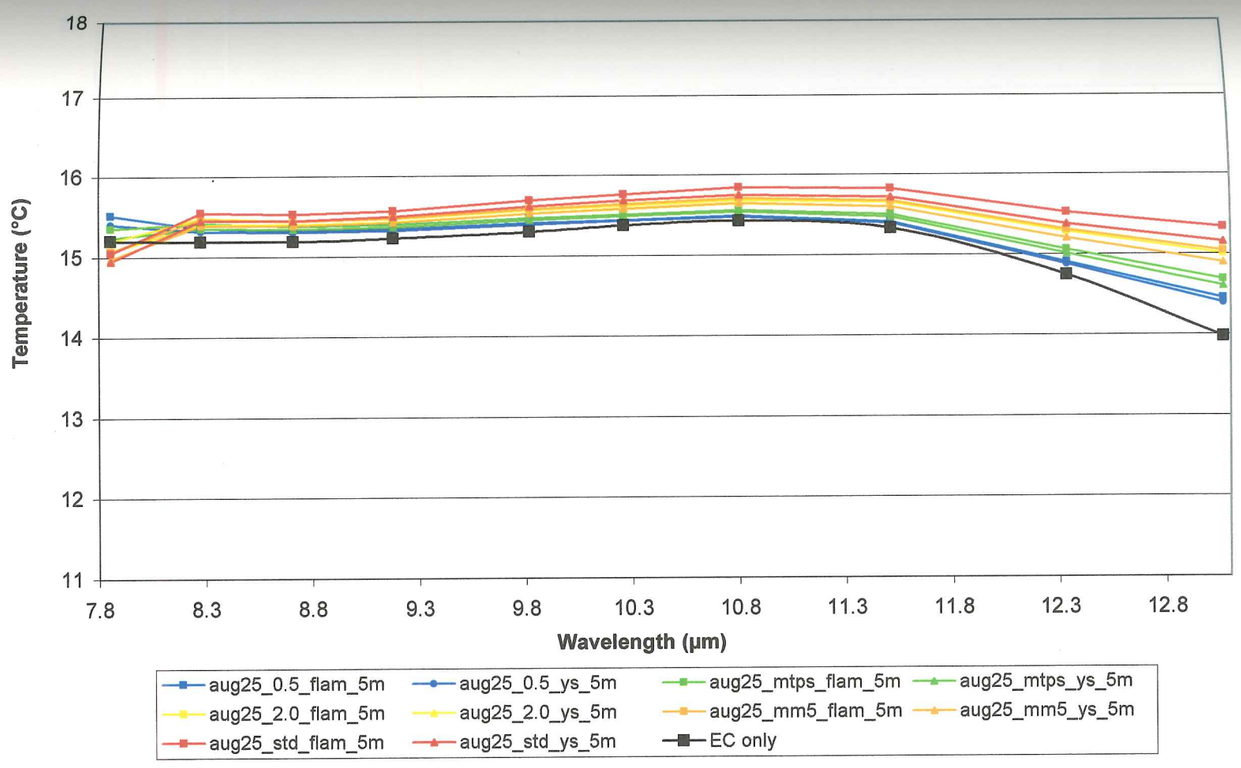

Figure 21b. Simulated At-Sensor Temperature (T_{rs}) - August 25, 2001 5m MASTER Data - 16 °C Target with EC and a Range of MODTRAN AC (Appendix I.) T_{rs} were simulated for Flaming Geyser State Park (flam) and Lake Youngs/Lake Sawyer (ys).

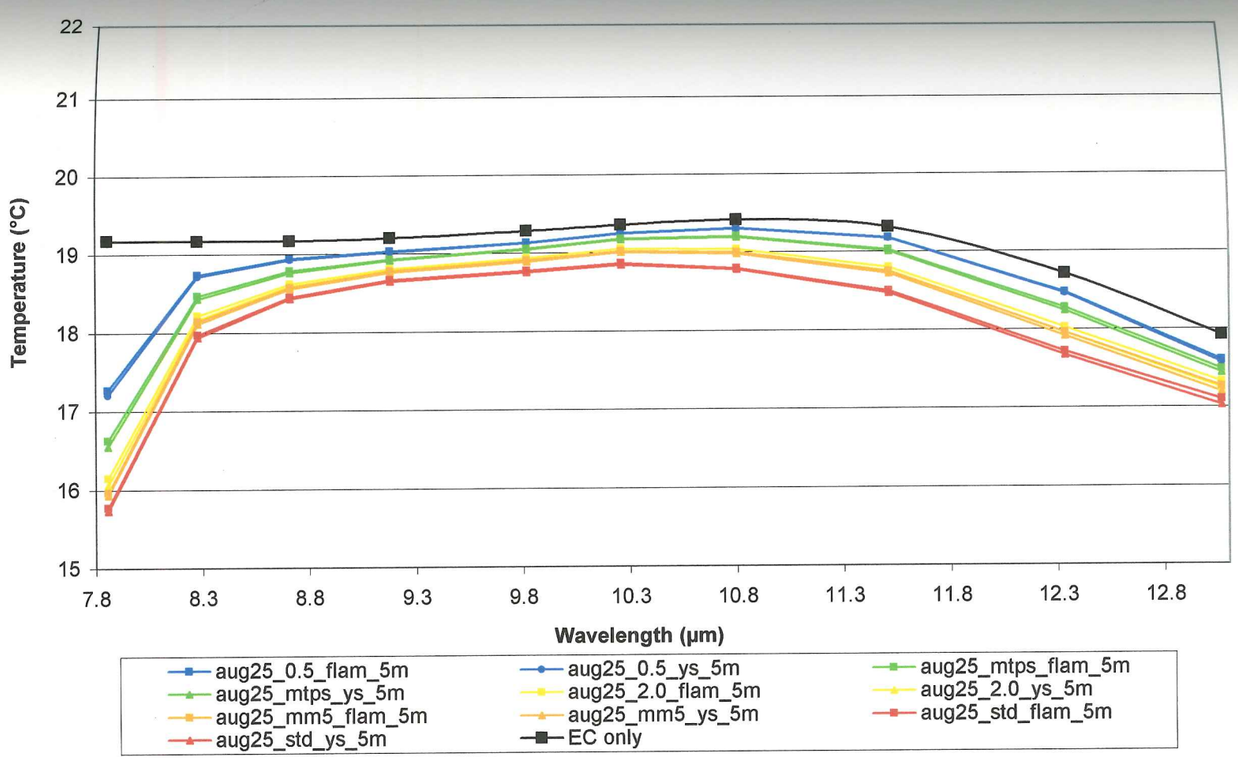

Figure 21c. Simulated At-Sensor Temperature (T_{rs}) - August 25, 2001 5m MASTER Data - 20 °C Target with EC and a Range of MODTRAN AC (Appendix I.) T_{rs} were simulated for Flaming Geyser State Park (flam) and Lake Youngs/Lake Sawyer (ys).

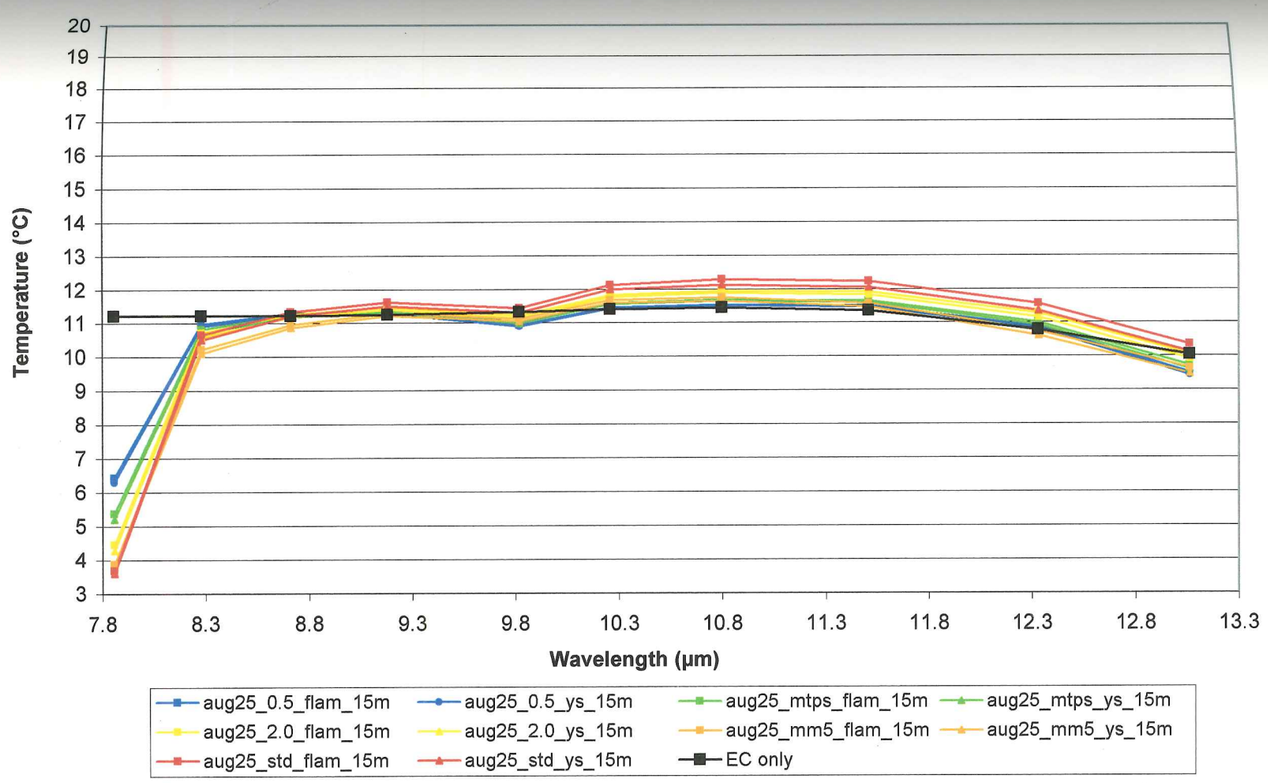

Figure 22a. Simulated At-Sensor Temperature (Trs) - August 25, 2001 15m MASTER Data - 12 °C Target with EC and a Range of MODTRAN AC (Appendix I.) T_{rs} were simulated for Flaming Geyser State Park (flam) and Lake Youngs/Lake Sawyer (ys).

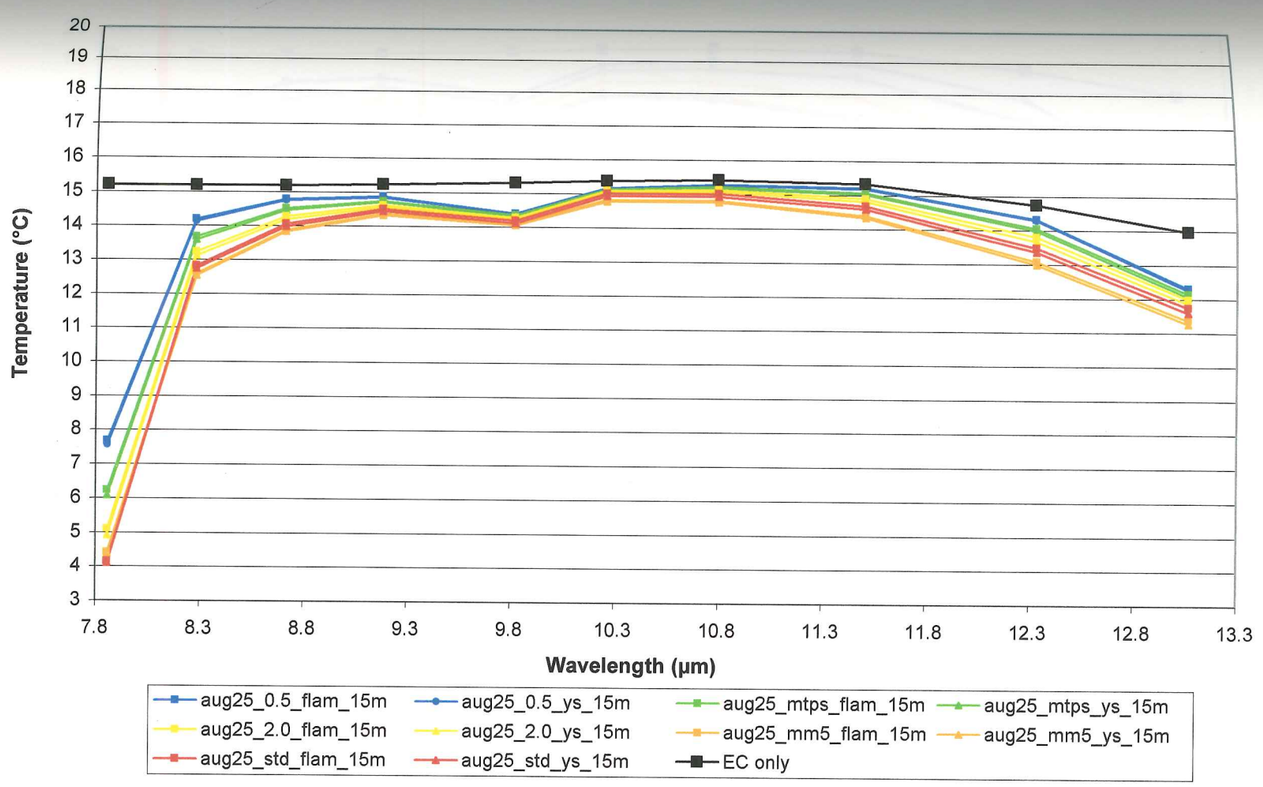

Figure 22b. Simulated At-Sensor Temperature (Trs) - August 25, 2001 15m MASTER Data - 16 °C Target with EC and a Range of MODTRAN AC (Appendix I.) T_{rs} were simulated for Flaming Geyser State Park (flam) and Lake Youngs/Lake Sawyer (ys).

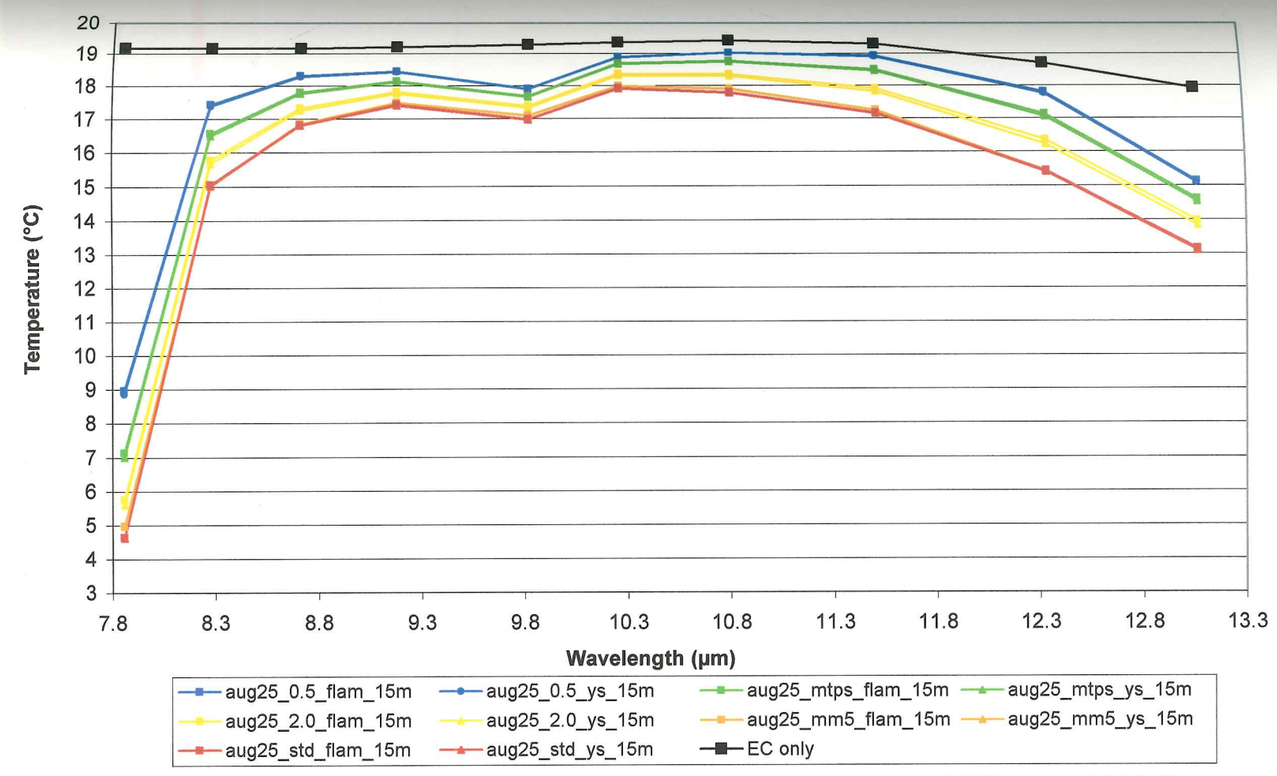

Figure 22c. Simulated At-Sensor temperature (Trs) - August 25, 2001 15m MASTER data - 20 °C Target with EC and a Range of MODTRAN AC (Appendix I.) T_{rs} is simulated for Flaming Geyser State Park (flam) and Lake Youngs/Lake Sawyer (ys).

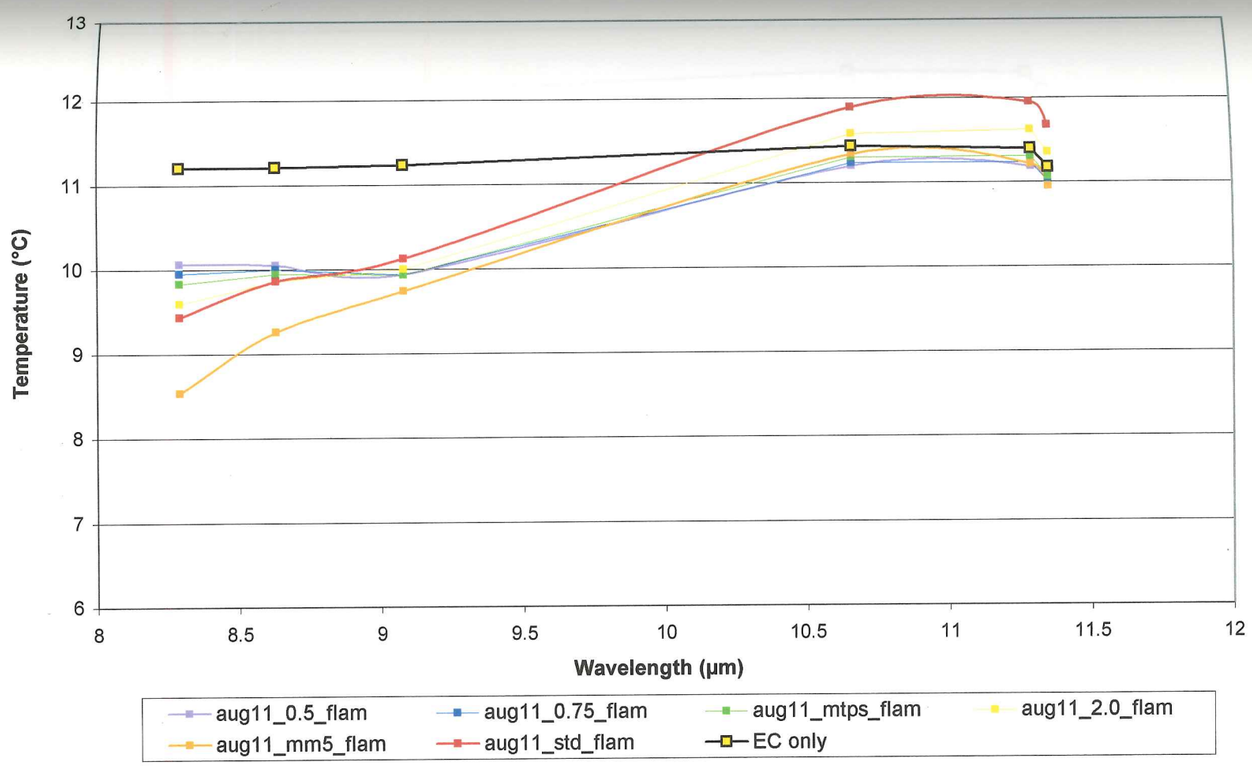

Figure 23a. Simulated At-Sensor Temperature (T_{rs}) - August 11, 2001 ASTER/Landsat 7 Data - 12 °C Target with EC and a Range of MODTRAN AC (Appendix I.) T_{rs} were simulated for Flaming Geyser State Park (flam).

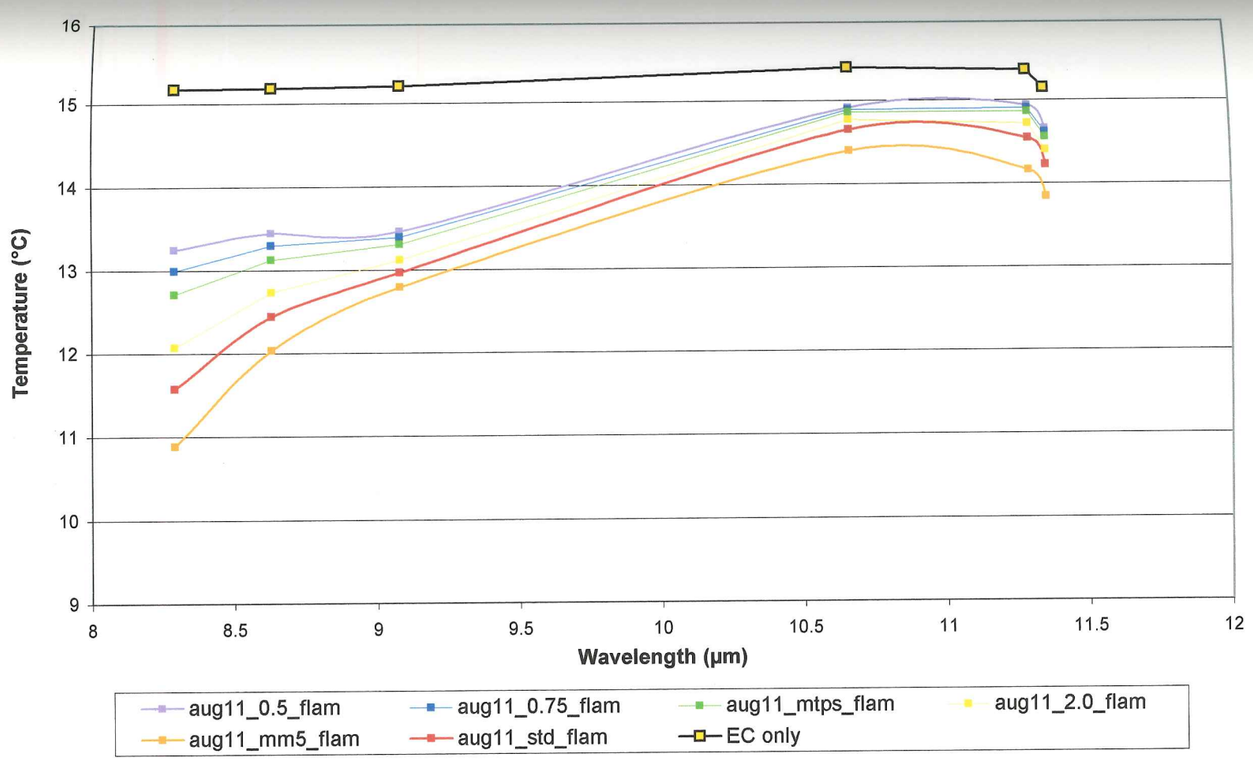

Figure 23b. Simulated At-Sensor Temperature (T_{rs}) - August 11, 2001 ASTER/Landsat 7 Data - 16 °C Target with EC and a Range of MODTRAN AC (Appendix I.) T_{rs} were simulated for Flaming Geyser State Park (flam).

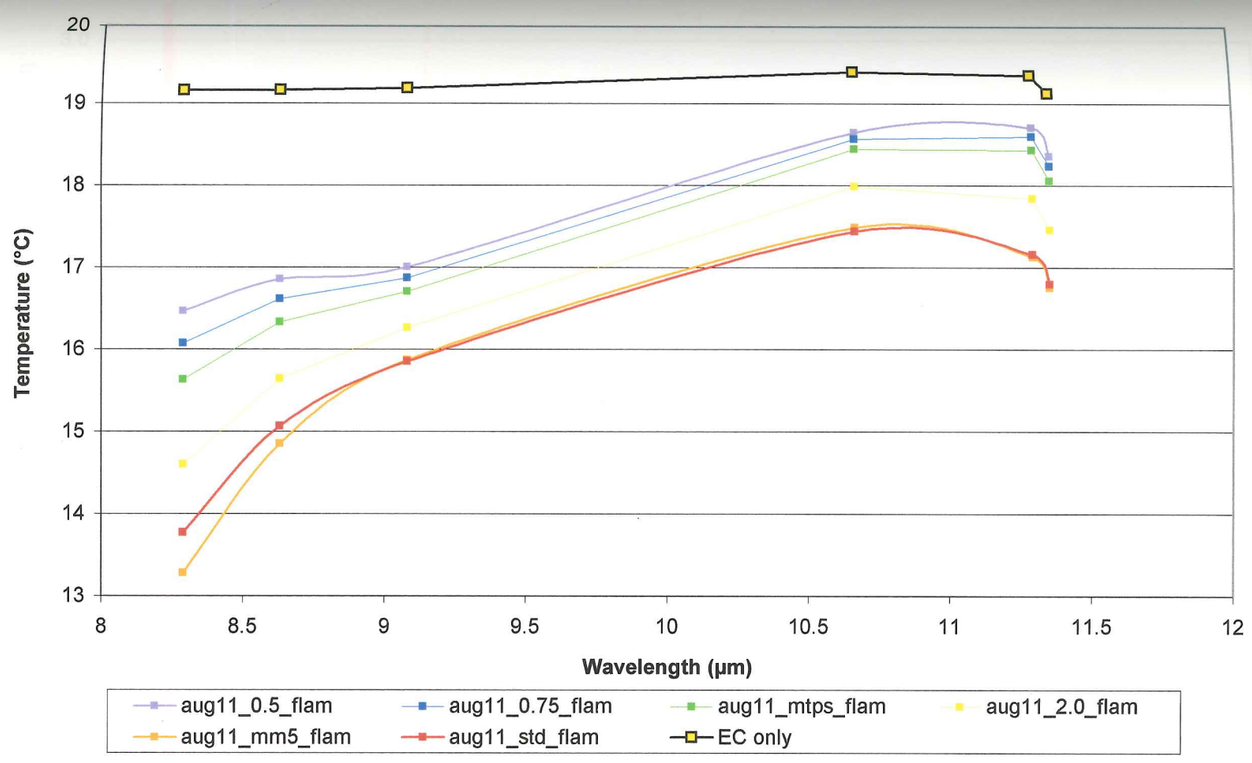

Figure 23c. Simulated At-Sensor Temperature (T_{rs}) - August 11, 2001 ASTER/Landsat 7 Data - 20 °C Target with EC and a Range of MODTRAN AC (Appendix I.) T_{rs} were simulated for Flaming Geyser State Park (flam).

Figure 24a. Effect of EC on Mean T_{rs} (MASTER: b43, b44, b46, b47, & b48; ASTER: b13 & b14)

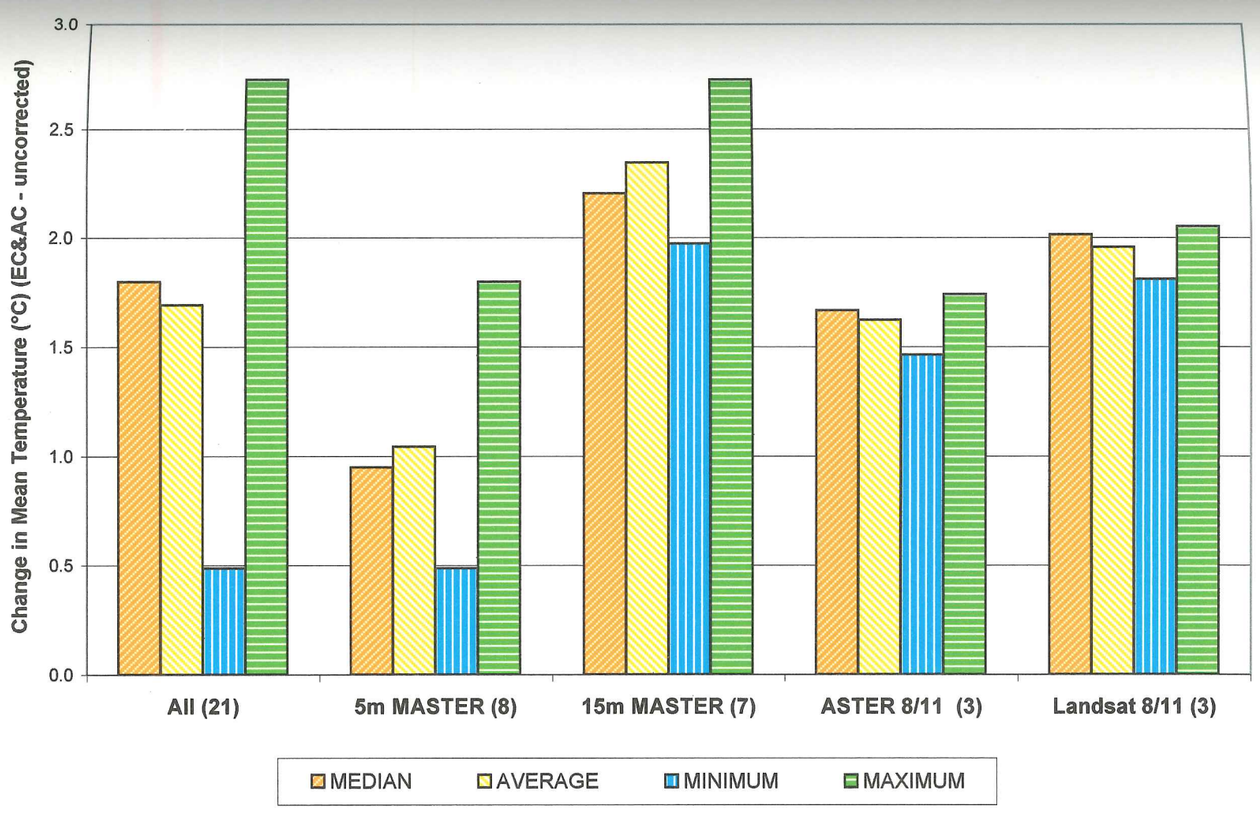

Figure 24b. Effect of EC and AC on Mean T_{rs} (MASTER: b43, b44, b46, b47, & b48; ASTER: b13 & b14)

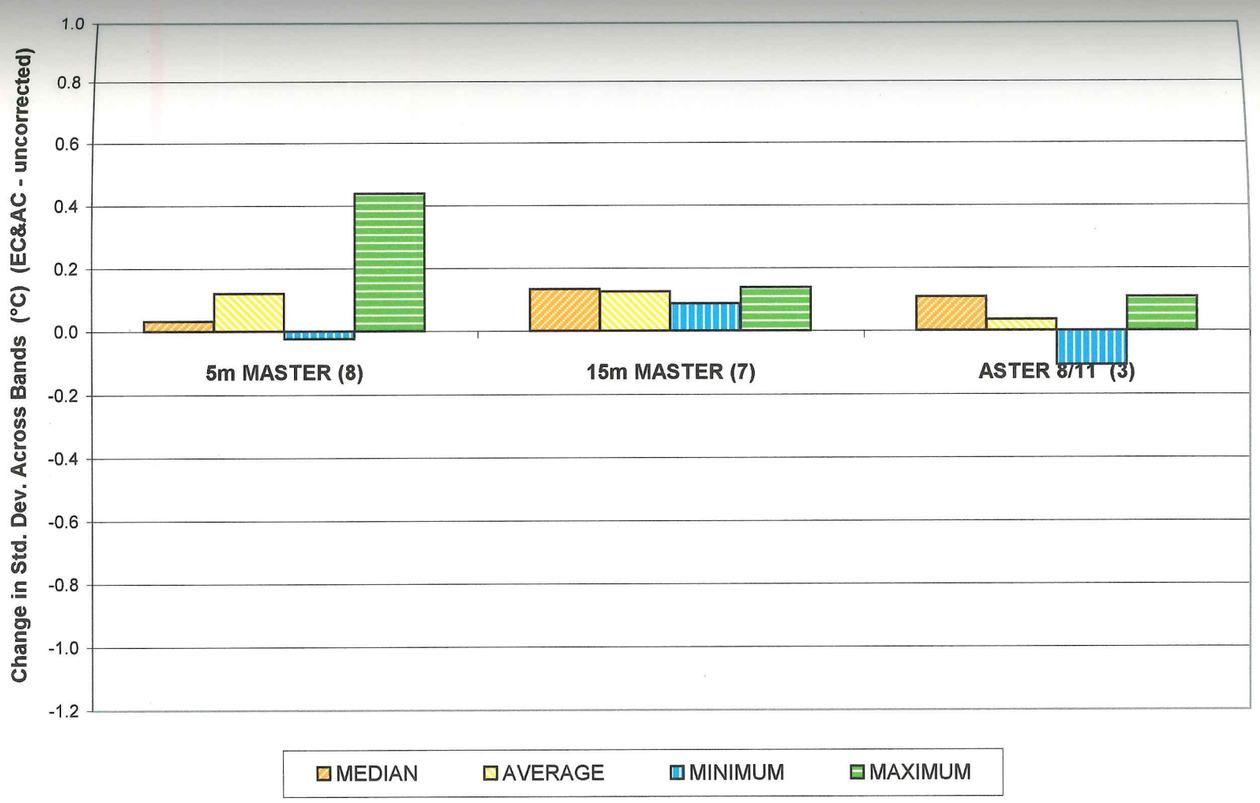

Figure 25a. Effect of EC on Standard Deviation in T_{rs} Across Bands (MASTER b42-b49, ASTER b10-b14)

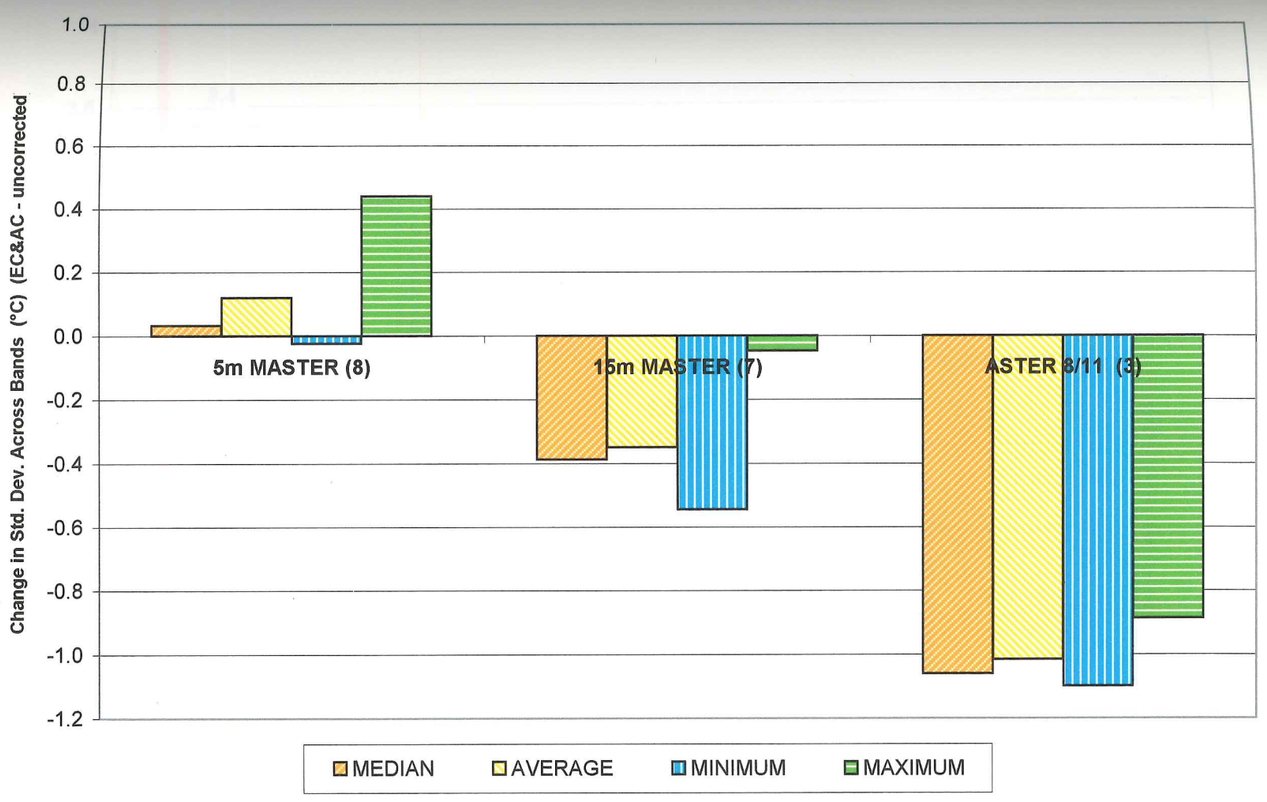

Figure 25b. Effect of EC and AC on Standard Deviation in T_{rs} Across Bands (MASTER b42-b49, ASTER b10-b14)

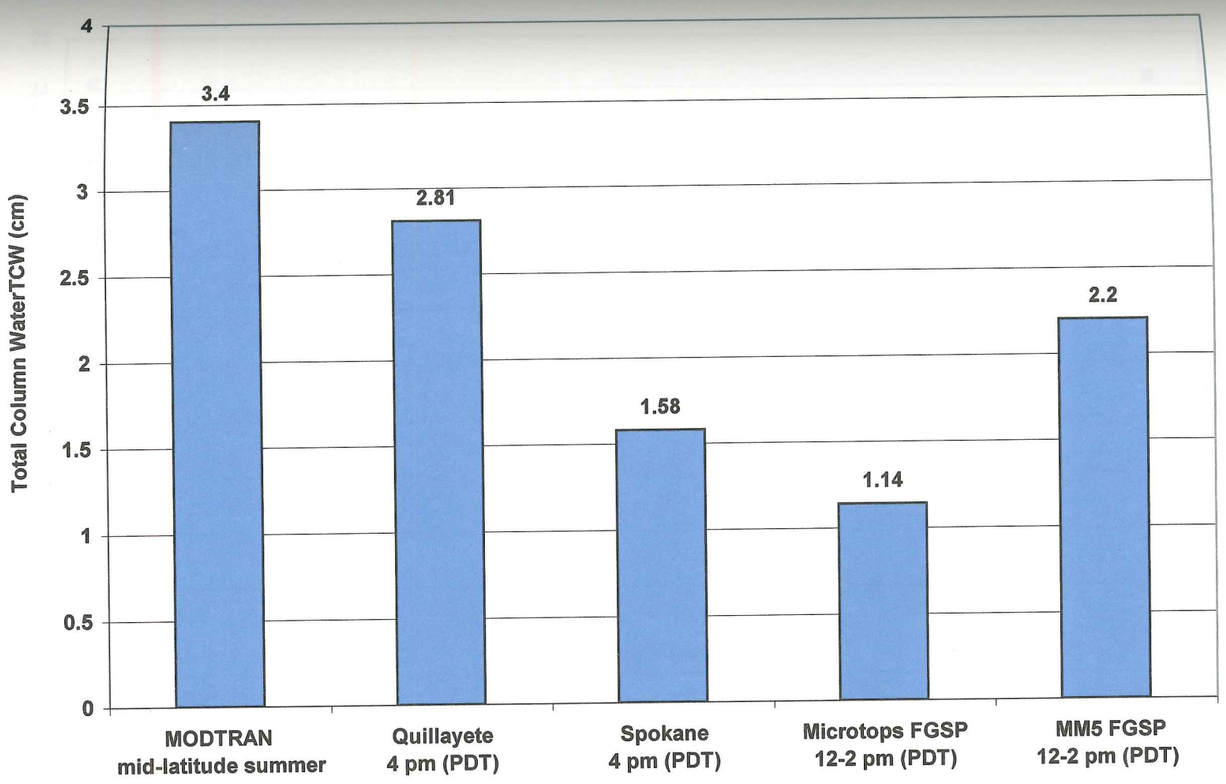

Figure 26. Total Column Water (TCW) Estimates for August 25, 2001

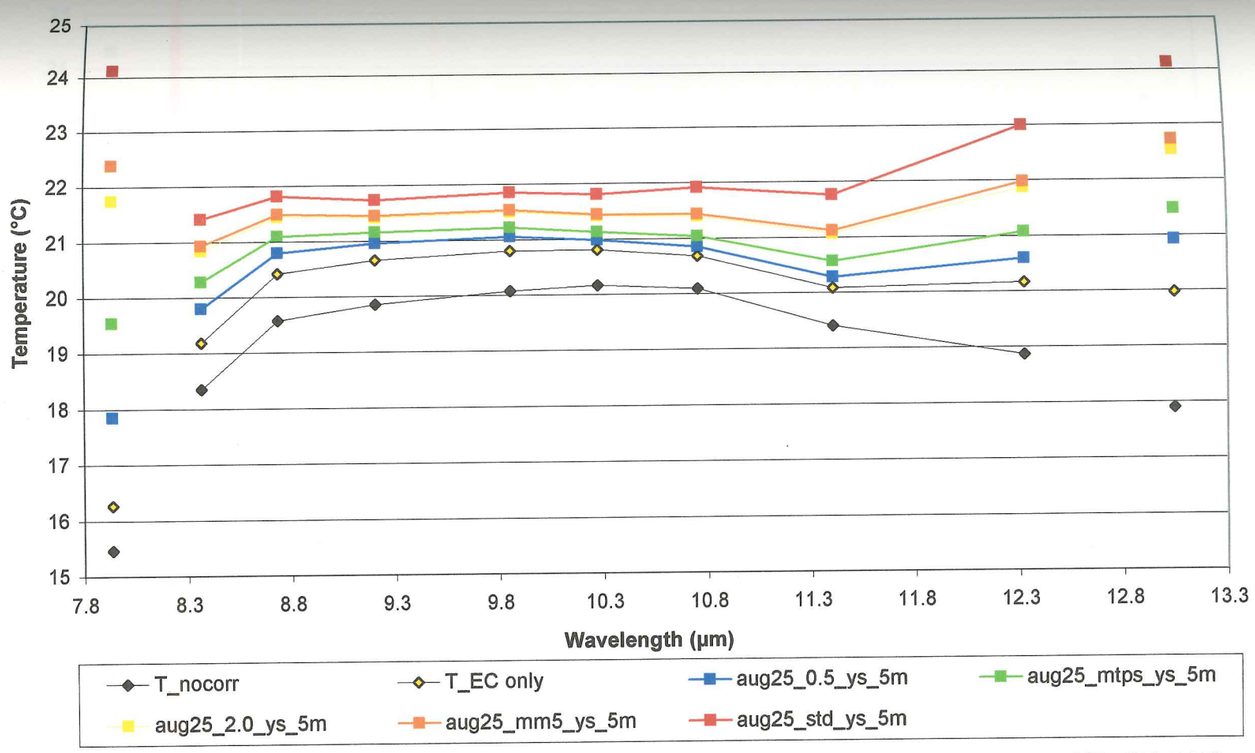

Figure 27. 5m MASTER (3-9) Lake Meridian Aug. 25, 2001 The aug25_2.0_ys_5m-corrected T_{rs} (21.5 °C) was within 0.3 °C of the ground-truth temperatures ($T_{radiant\text{-}surface}$ = 21.5 ± 0.5 °C, $T_{kinetic\text{-}surface}$ = 21.5 ± 0.3 °C, $T_{kinetic\text{-}gage}$ = 21.2 ± 0.3 °C).

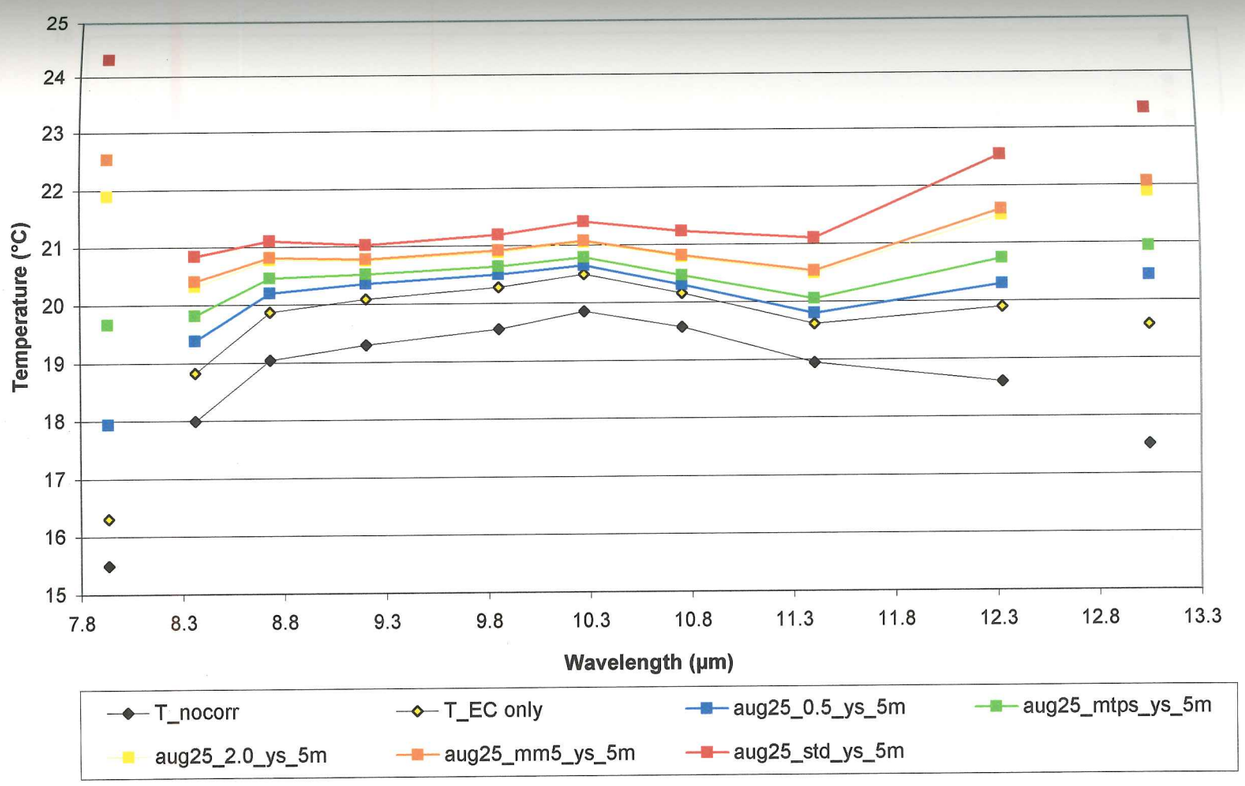

Figure 28. 5m MASTER (3-8) Lake Sawyer Aug. 25, 2001 The aug25_2.0_ys_5m-corrected T_{rs} (20.9 °C) was within 0.6 °C of the ground-truth temperatures ($T_{radiant\text{-}surface}$ 21.5 ± 2.0 °C, $T_{kinetic\text{-}surface}$ 21.4 ± 0.4 °C).

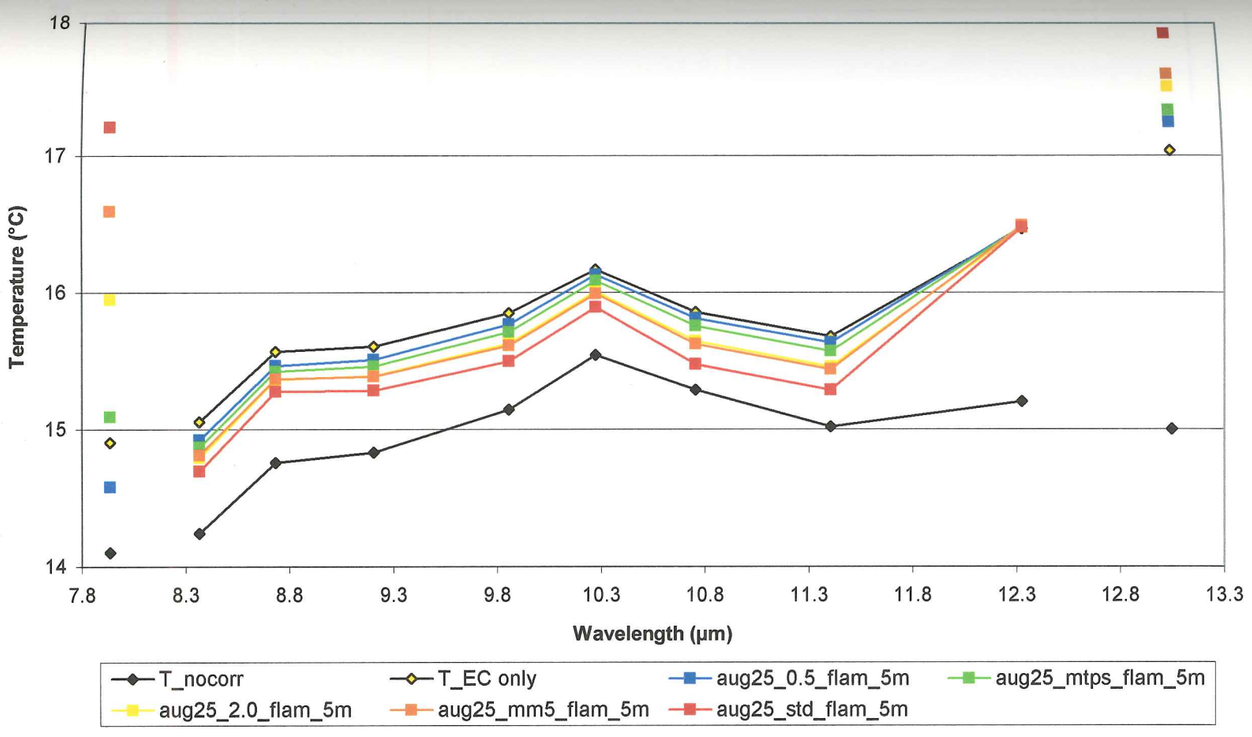

Figure 29. 5m MASTER Green River (GR5) Aug. 25, 2001 The aug25_2.0_flam_5m-corrected T_{rs} (15.6 °C) were higher than ground-truth temperatures ($T_{kinetic\text{-}gage}$ = 14.5 ± 0.3 °C, $T_{radiant\text{-}surface}$ = 14 ± 2.0 °C, $T_{kinetic\text{-}surface}$ = 14.8 ± 0.5 °C). As target temperature was lower, AC reduced radiant temperature.

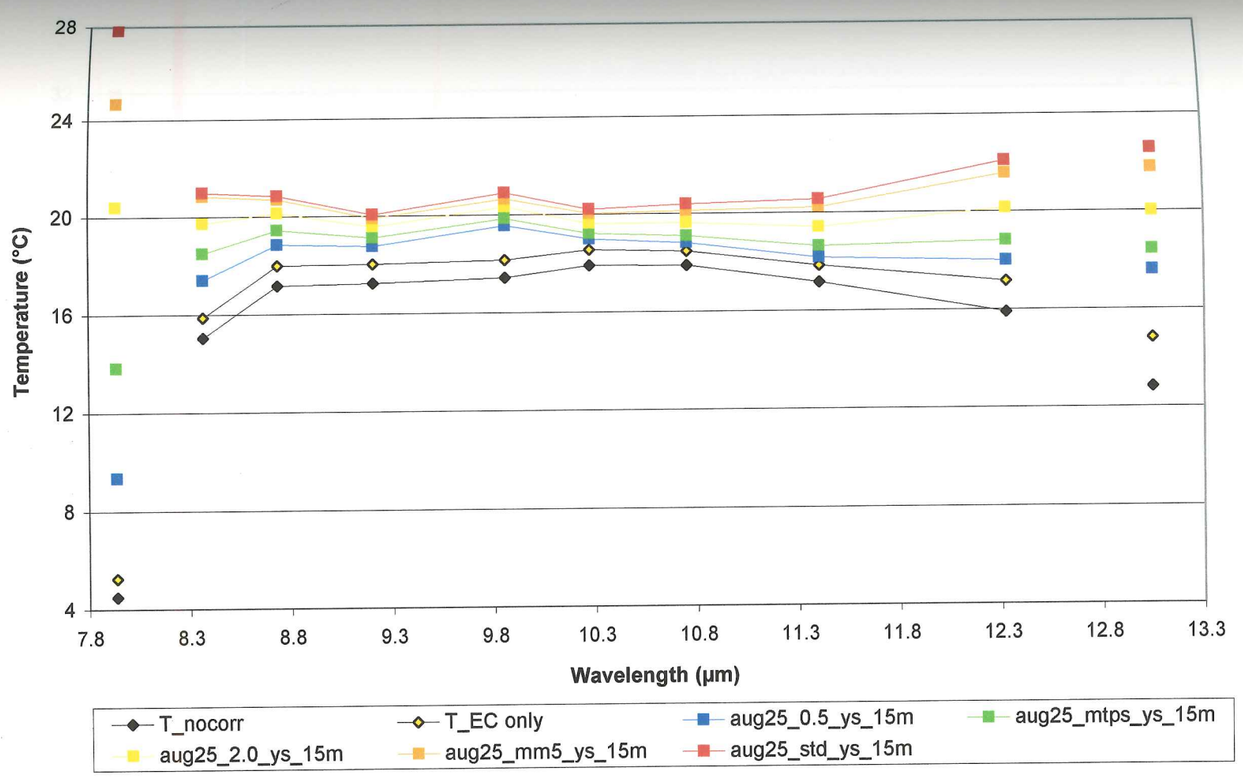

Figure 30. 15m MASTER (4-8) Lake Youngs Aug 25, 2001 The aug25_2.0_ys_15m-corrected T_{rs} (19.7 °C) was more consistent with ground-truth temperatures ($T_{kinetic\text{-}gage}$ = 19.5 ± 0.5 °C) than the uncorrected T_{rs} (17.5 °C).

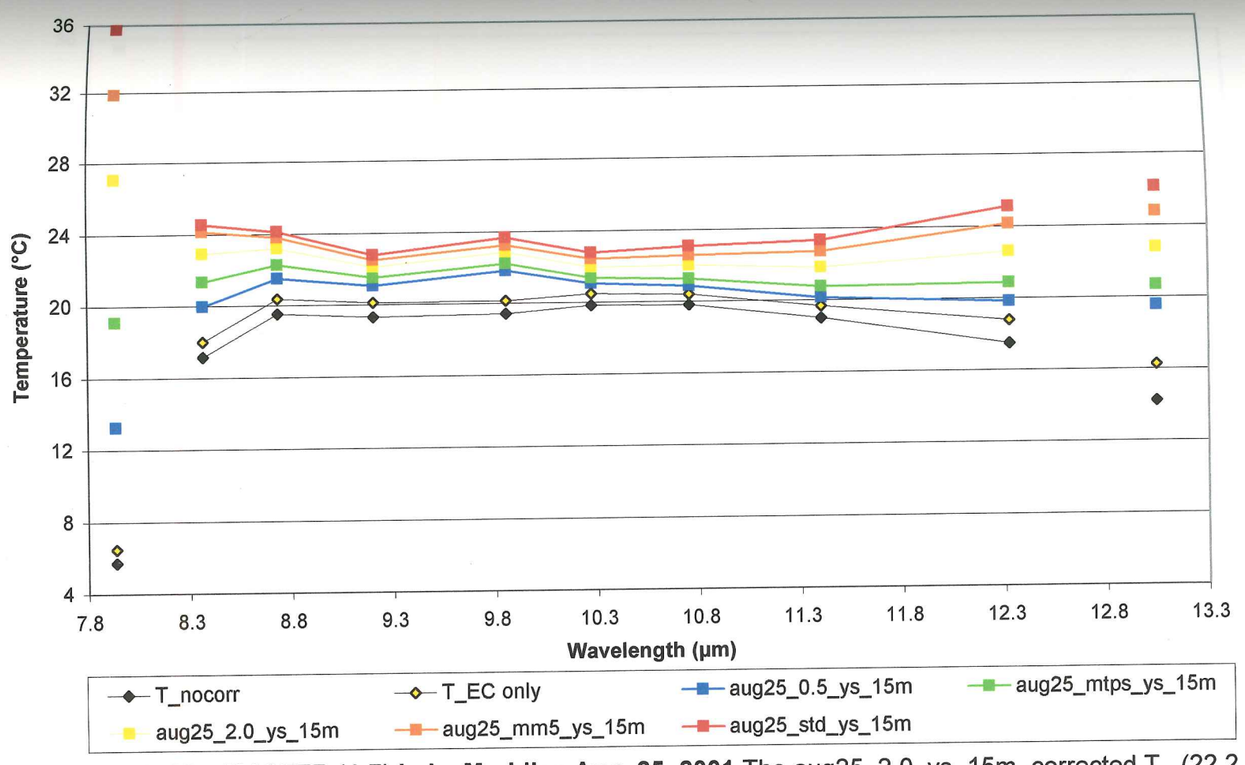

Figure 31. 15m MASTER (4-7) Lake Meridian Aug. 25, 2001 The aug25_2.0_ys_15m -corrected T_{rs} (22.2 °C) was within 0.9 ºC of the ground-truth temperatures ($T_{kinetic\text{-}gage}$ = 21.1 ± 0.3 °C, $T_{radiant\text{-}surface}$ = 21.5 ± 0.5 °C, $T_{kinetic\text{-}surface}$ = 22.4± 0.7°C) .

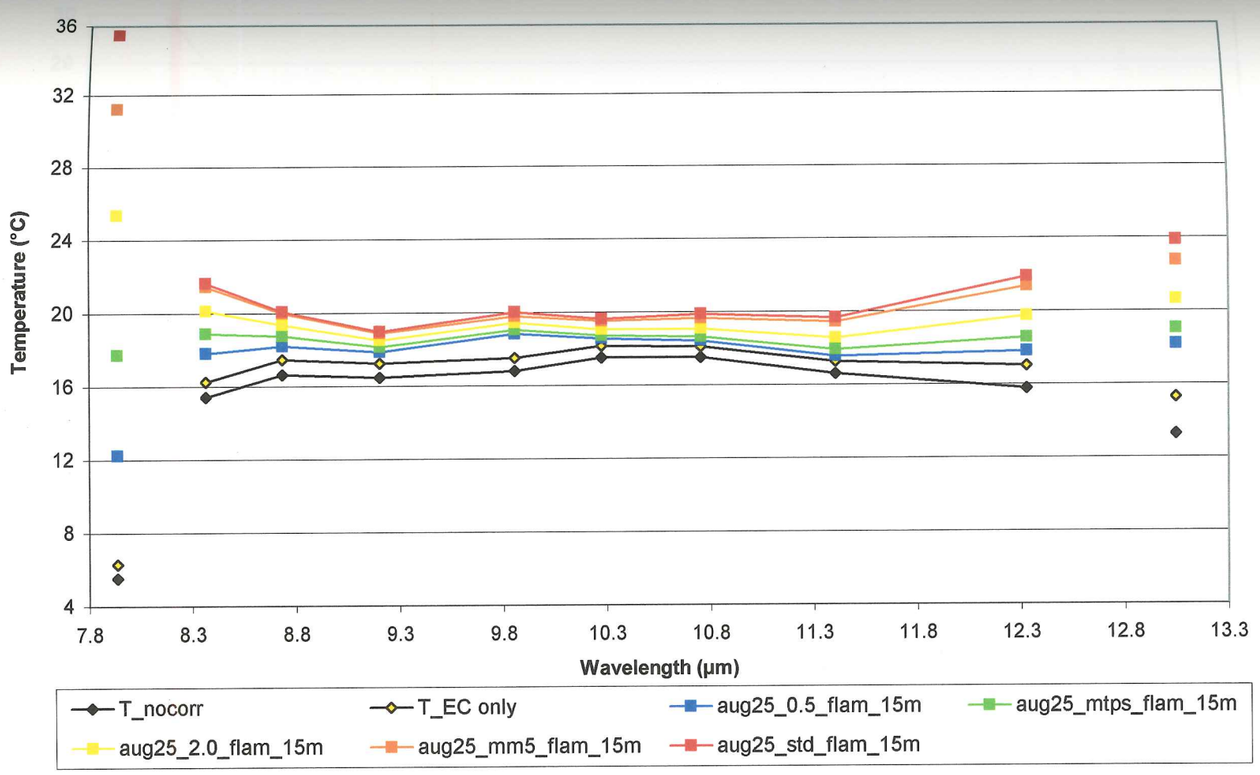

Figure 32. 15m Green River (GR5) Aug. 25, 2001 The aug25_2.0_flam_15m-corrected T_{rs} (18.9 °C) was 2.2 ºC greater than gage ground-truth temperature ($T_{kinetic\text{-}gage}$ =16.7 °C).

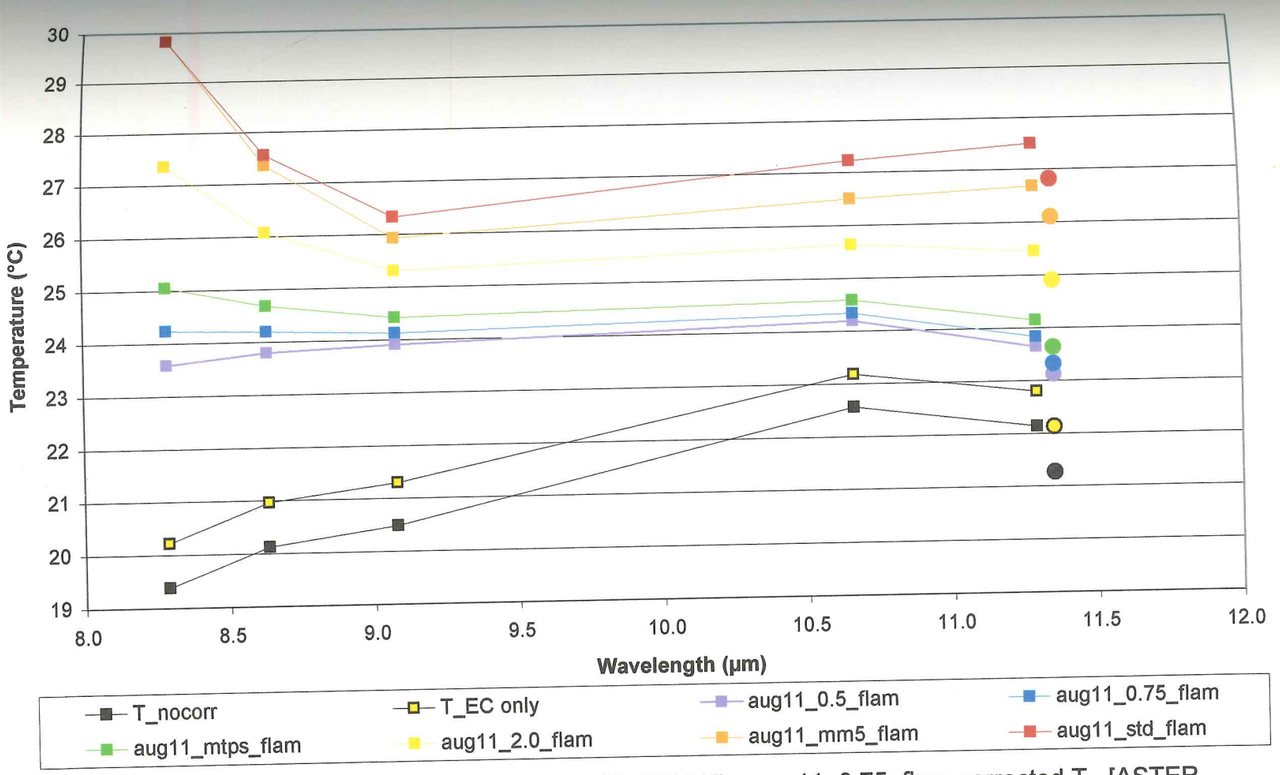

Figure 33. ASTER/Landsat 7 Lake Meridian Aug. 11, 2001 The aug11_0.75_flam-corrected T_{rs} [ASTER (squares): 24.1 °C, Landsat 7 (circles): 23.3 °C] were within 0.7 °C of ground-truth temperatures ($T_{kinetic\text{-}gage}$ = 23.4 ± 0.8 °C, $T_{radiant\text{-}surface}$ = 23.6 ± 0.2 °C, $T_{kinetic\text{-}surface}$ = 23.6 ± 0.7 °C).

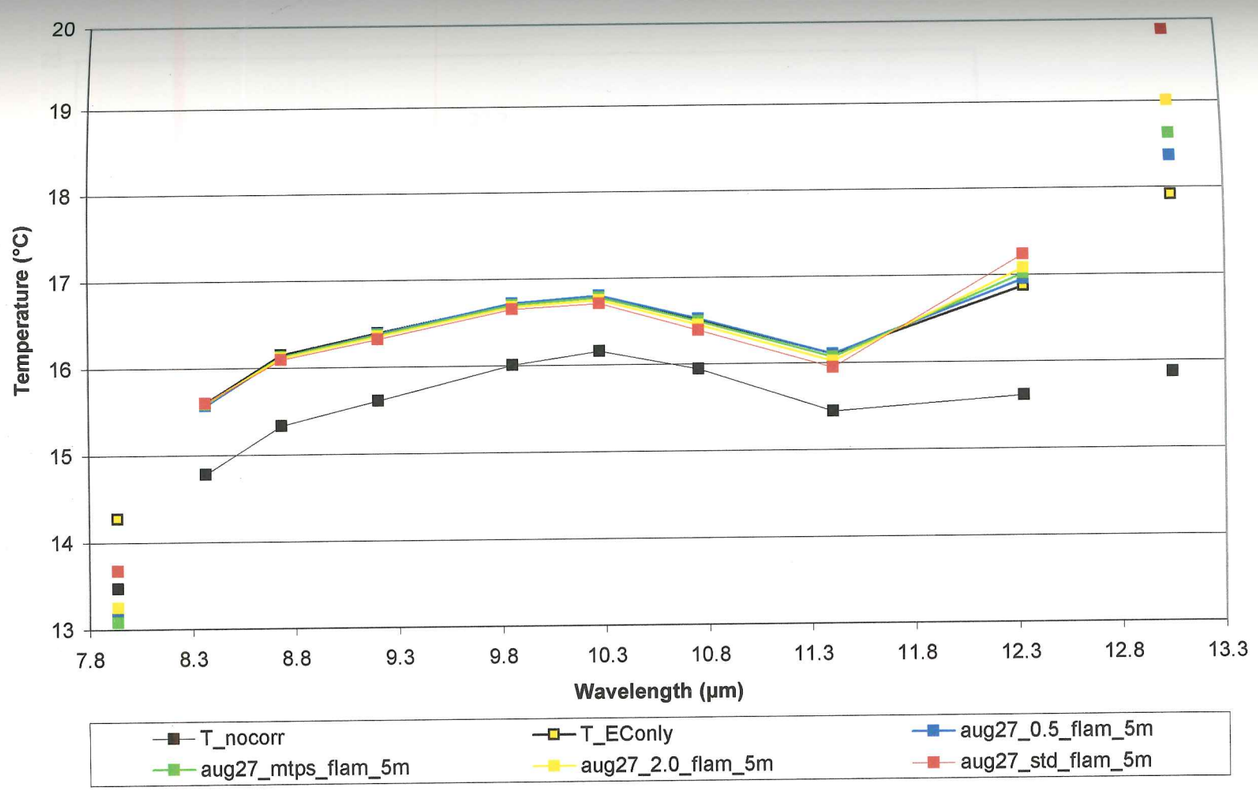

Figure 34. 5m MASTER Green River Aug. 27, 2001 Corrected T_{rs} at GR5 (16.4 °C) was greater than the gage ground-truth ($T_{kinetic\text{-}gage}$ =15.4 °C ± 0.2 °C). AC had little effect on T_{rs} from 8.3 - 12.3 µm.

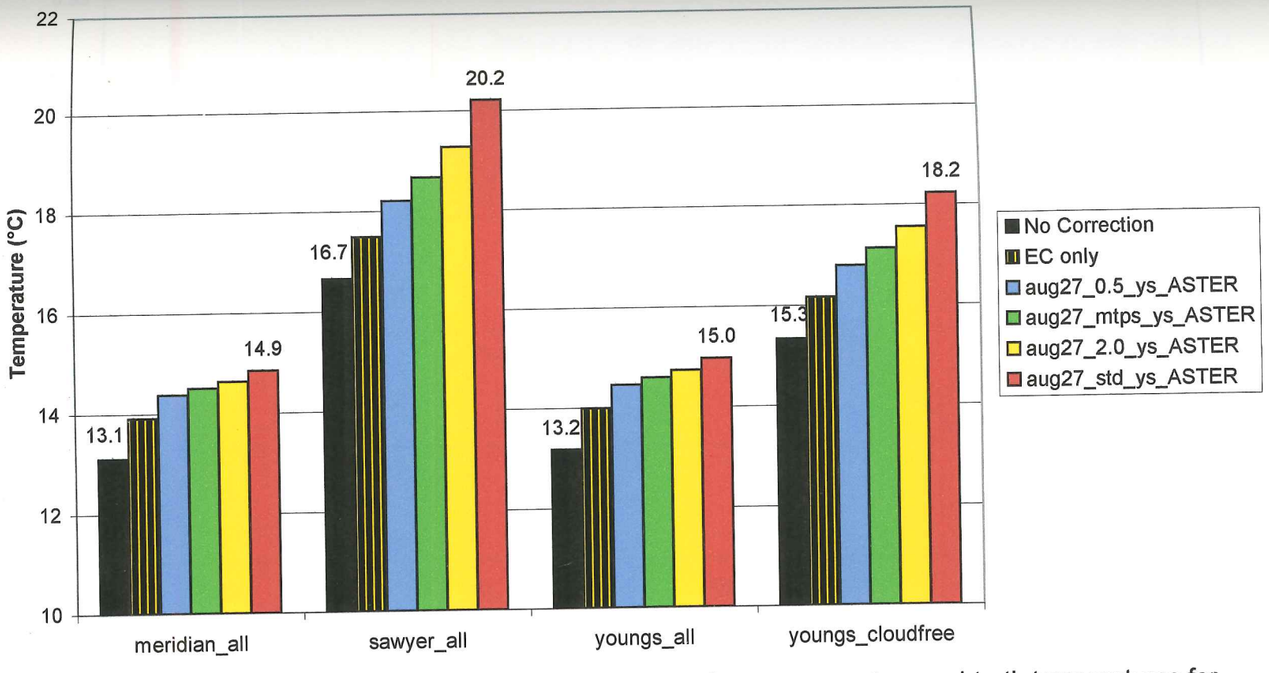

Figure 35. Landsat 7 Lakes Aug. 27, 2001 All T_{rs} were less than concurrent ground-truth temperatures for Lake Meridian ($T_{kinetic\text{-}gage}$ = 21.7 ± 0.3 °C, $T_{radiant\text{-}surface}$ = 21.5 ± 1.0 °C, $T_{kinetic\text{-}surface}$ = 21.2 ± 0.6 °C) and Lake Youngs ($T_{kinetic\text{-}gage}$ = 18.6 ± 0.3 °C). AC was difficult to evaluate at Lake Sawyer with only one TIR band and inconsistent ground-truth temperatures ($T_{radiant\text{-}surface}$ = 18.5 ± 2.0 °C, $T_{kinetic\text{-}surface}$ = 21.7 ± 0.4 °C).

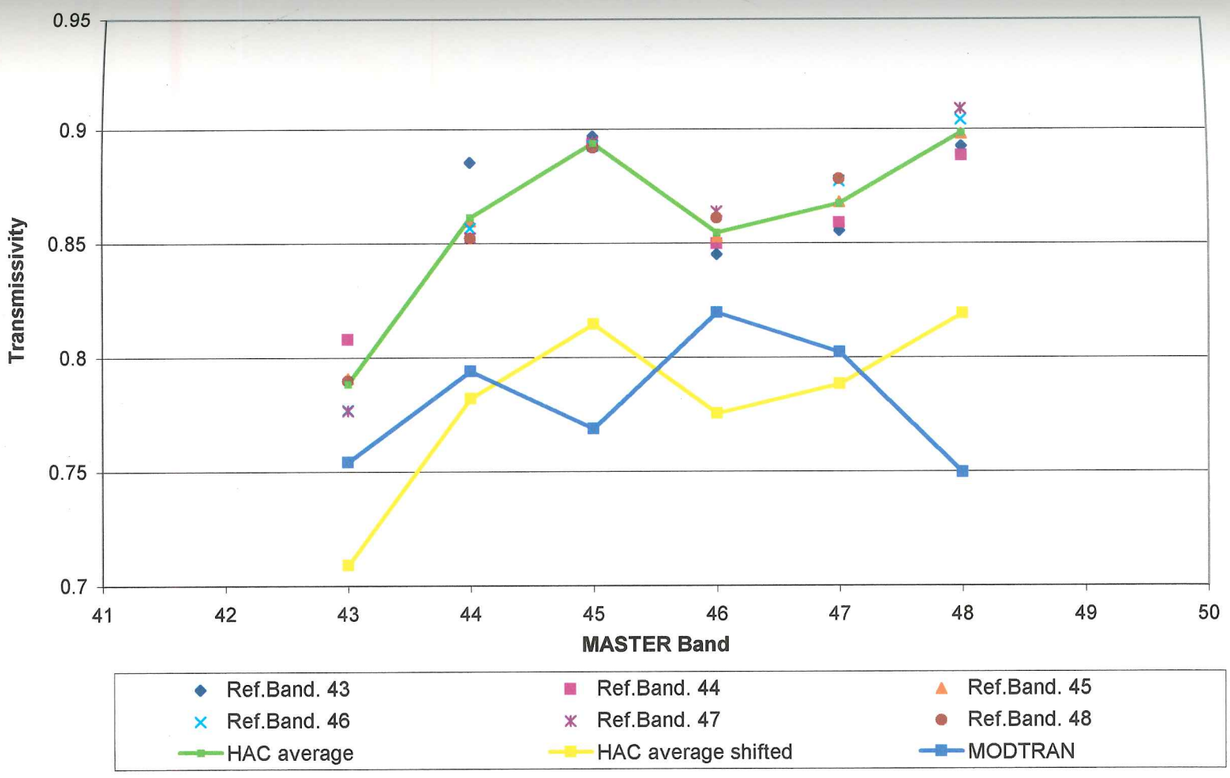

Figure 36a. HAC Method (ridge vegetation) - Transmissivity This plot shows HAC results for each reference band, averaging of all reference bands (green), and shifting to obtain HAC correction (yellow).

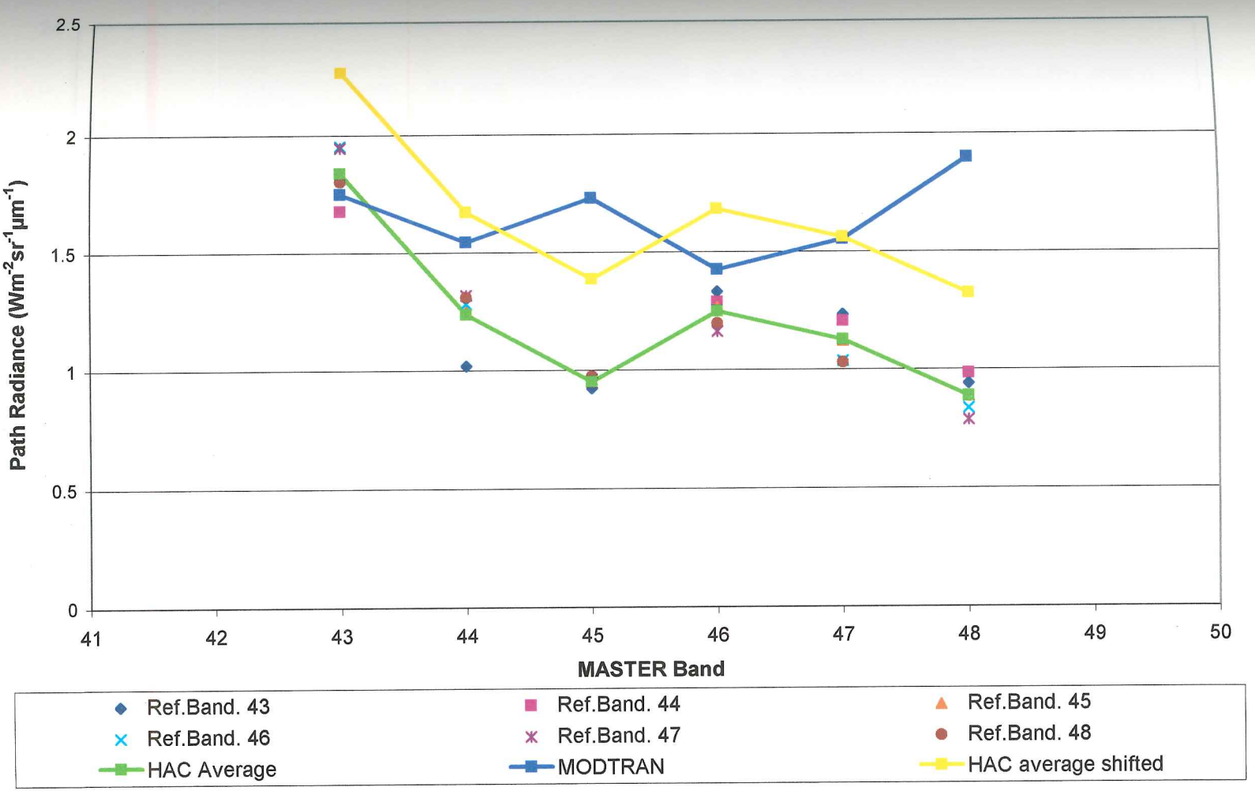

Figure 36b. HAC Method (ridge vegetation) - Path Radiance This plot shows HAC results for each reference band, averaging of all reference bands (green), and shifting to obtain HAC correction (yellow).

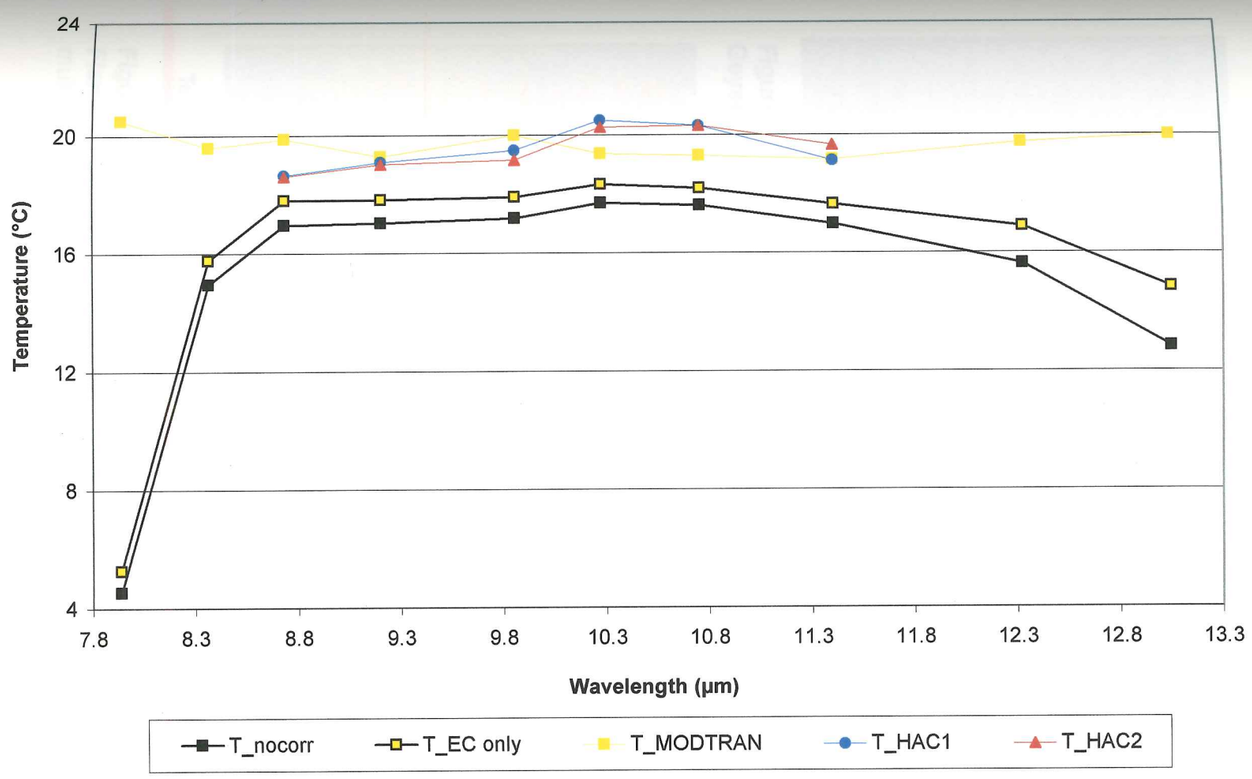

Figure 37. HAC - 15m MASTER (4-7) Lake Youngs Aug. 25, 2001. HAC1 (ridge vegetation) and HAC2 (youngs vegetation) have a distinct spectral shape. However, the resulting T_{rs} were similar to MODTRAN T_{rs}.

Figure 38a. Visible Image Looking Down Green River at Flaming Geyser State Park on August 11, 2001

Figure 38b. FLIR Thermal Image Looking Down Green River at Flaming Geyser State Park on August 11, 2001 Arrow shows where multiple scattering increased radiant water temperature.

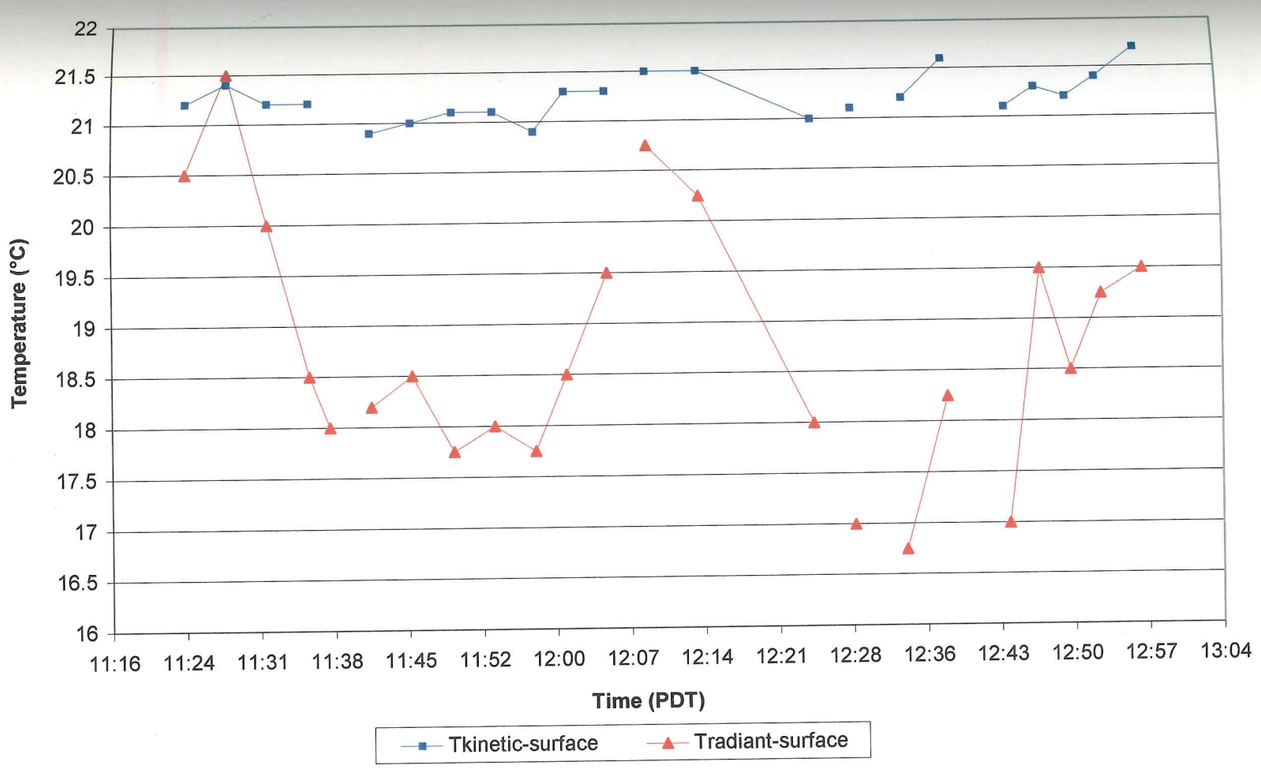

Figure 39. Lake Sawyer radiant and surface-kinetic ground-truth temperatures - August 25, 2001 Radiant temperatures were often less than kinetic temperatures. Possible explanations include: wind-driven surface evaporative cooling or detector instability.

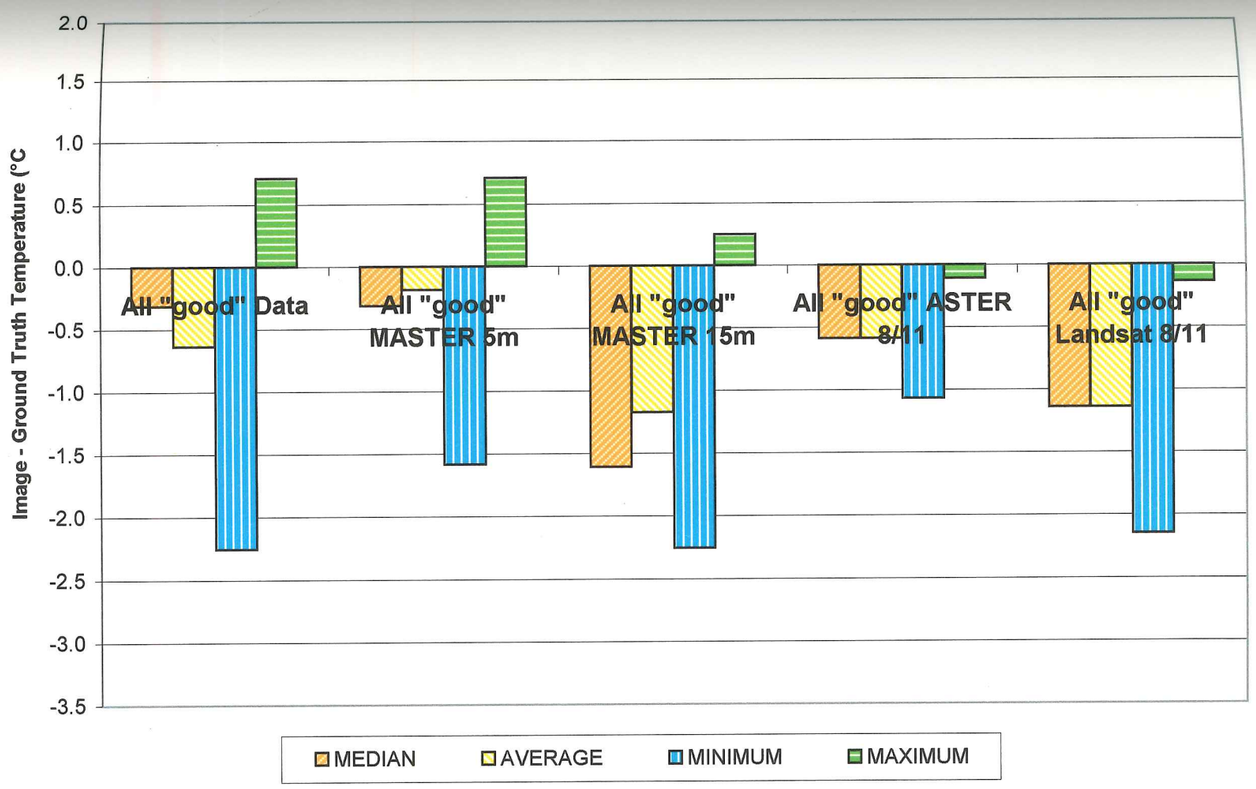

Figure 40a. Difference Between Uncorrected Image Temperatures and Gage Temperatures (T_{rs} - $T_{kinetic\text{-}gage}$)

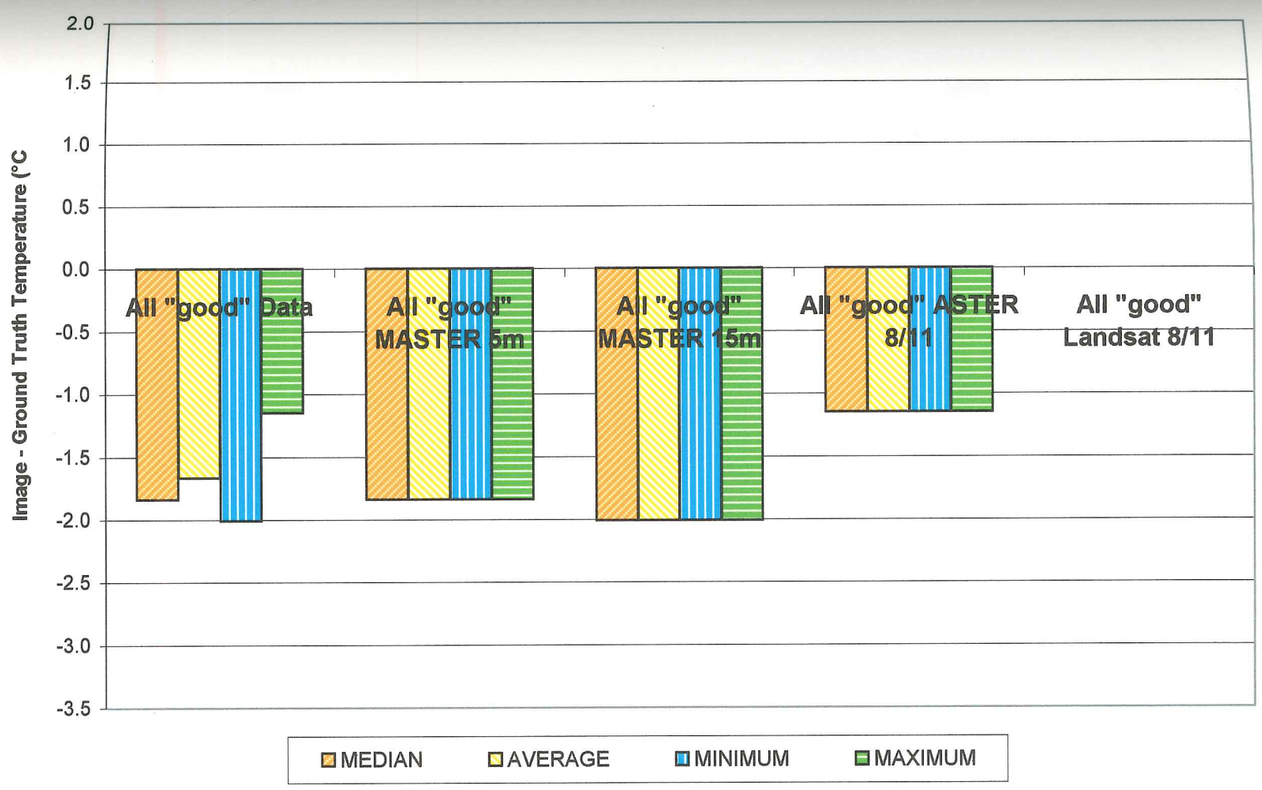

Figure 40b. Difference Between Uncorrected Image Temperatures and Surface Radiant Temperatures (T_{rs} - $T_{radiant\text{-}surface}$)

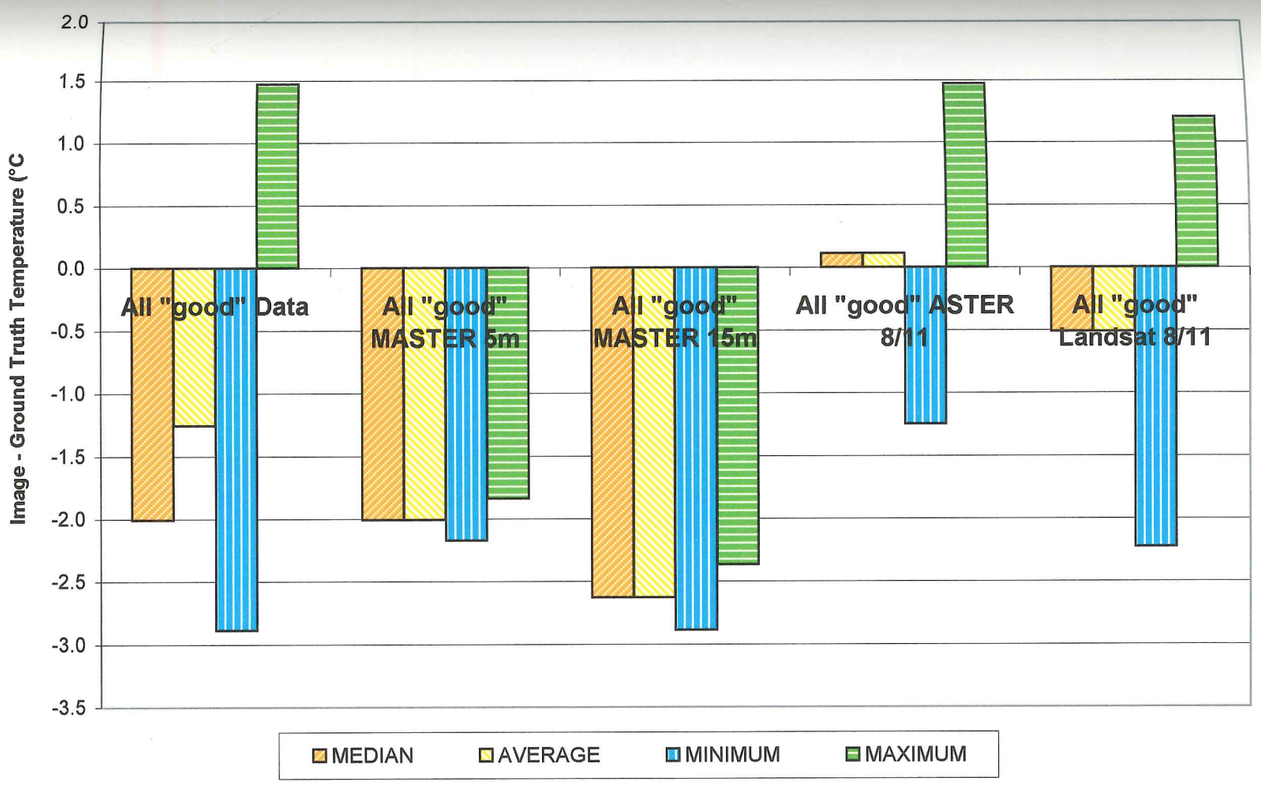

Figure 40c. Difference Between Uncorrected Image Temperatures and Surface Kinetic Temperatures (T_{rs} - $T_{kinetic\text{-}surface}$)

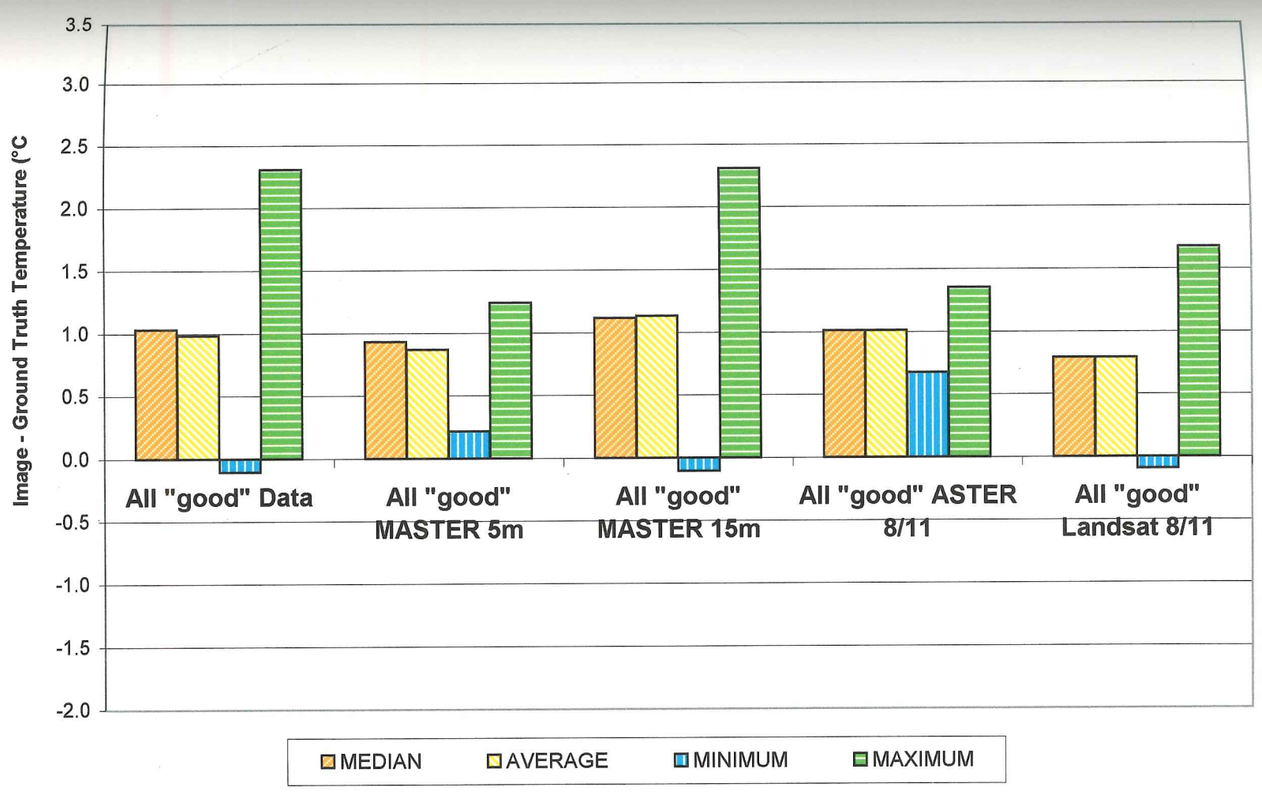

Figure 40d. Difference Between EC/AC-Corrected Image Temperatures and Gage Temperatures (T_{rs} - $T_{kinetic\text{-}gage}$)

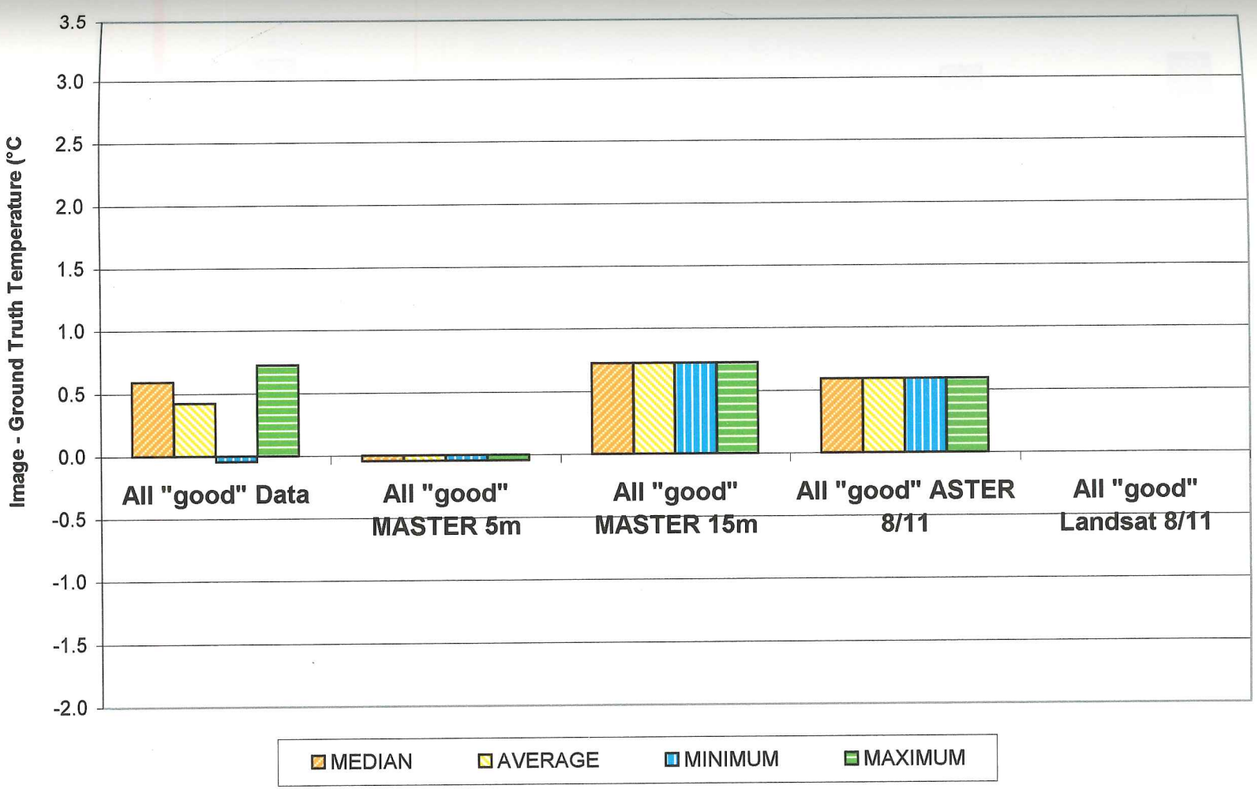

Figure 40e. Difference Between EC/AC-Corrected Image Temperatures and Surface Radiant Temperatures (T_{rs} - $T_{radiant\text{-}surface}$)

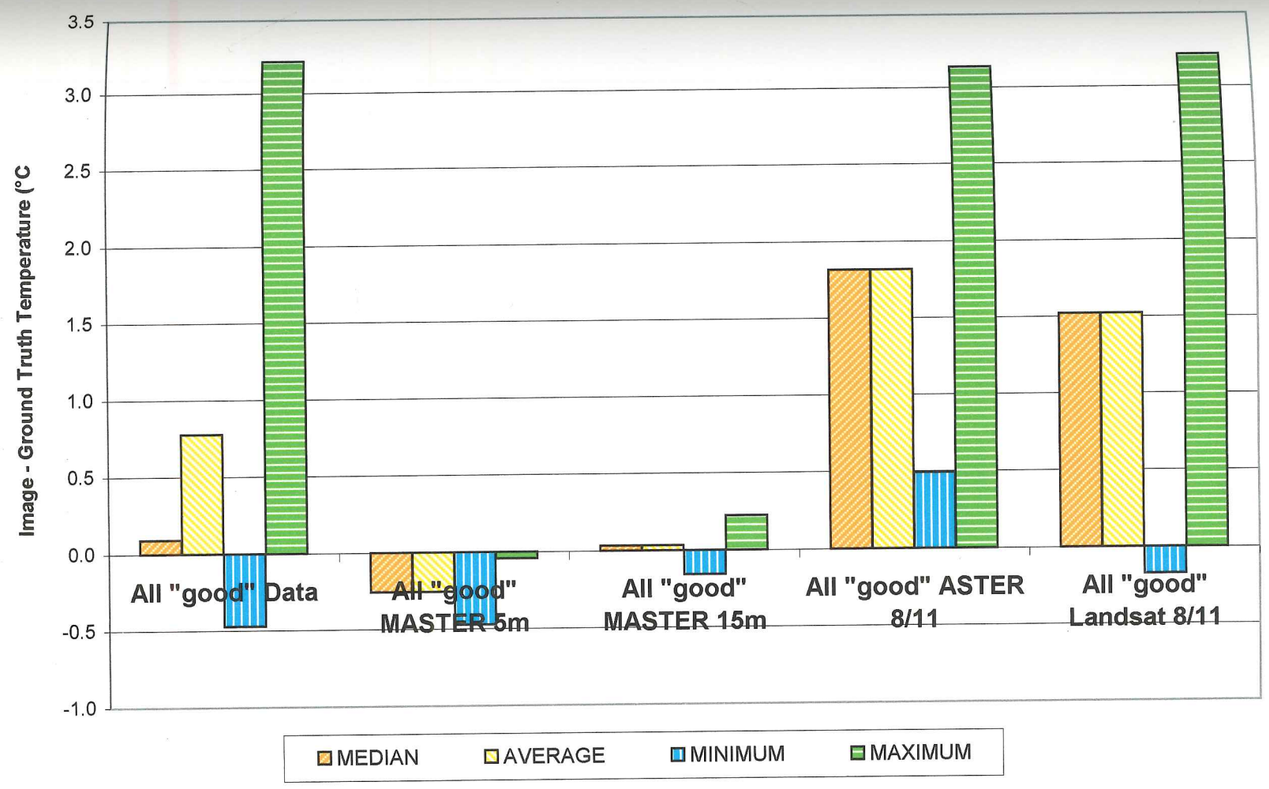

Figure 40f. Difference Between EC/AC-Corrected Image Temperatures and Surface Kinetic Temperatures (T_{rs} - $T_{kinetic\text{-}surface}$)

Table 1. Modis-ASTER Airborne Simulator (MASTER) Bands

MASTER BAND	Minimum (μm)	Maximum (μm)	Effective Center (μm)
1	0.44	0.48	0.46
2	0.48	0.52	0.50
3	0.52	0.56	0.54
4	0.56	0.60	0.58
5	0.63	0.69	0.66
6	0.69	0.74	0.71
7	0.73	0.78	0.75
8	0.78	0.83	0.80
9	0.85	0.89	0.87
10	0.89	0.93	0.91
11	0.93	0.97	0.95
12	1.59	1.65	1.62
13	1.65	1.70	1.68
14	1.70	1.75	1.73
15	1.75	1.81	1.78
16	1.81	1.86	1.83
17	1.86	1.91	1.88
18	1.91	1.96	1.93
19	1.96	2.01	1.98
20	2.06	2.11	2.08
21	2.14	2.19	2.17
22	2.19	2.24	2.22
23	2.24	2.29	2.26
24	2.30	2.37	2.33
25	2.37	2.42	2.39
26	3.07	3.22	3.14
27	3.22	3.36	3.28
28	3.36	3.51	3.44
29	3.52	3.67	3.59
30	3.67	3.81	3.74
31	3.82	3.97	3.89
32	3.98	4.12	4.05
33	4.14	4.29	4.21
34	4.31	4.42	4.36
35	4.42	4.57	4.50
36	4.57	4.73	4.65
37	4.73	4.88	4.80
38	4.87	5.02	4.95
39	5.02	5.17	5.09
40	5.17	5.32	5.24
41	7.70	8.04	7.86
42	8.07	8.50	8.28
43	8.51	8.90	8.71
44	8.97	9.39	9.18
45	9.64	10.04	9.82
46	10.06	10.47	10.26
47	10.50	11.11	10.80
48	11.18	11.86	11.51
49	12.08	12.59	12.33
50	12.82	13.30	13.06

Table 2. Summary Statistics for Regions of Interest in Mt. Rainier MASTER Data

Region of Interest (ROI) Name	ROI Color	DISORT INPUT ANGLES (°) Incidence	Emission	Phase	Average Visible Albedo b1-b11	Calculation Error Visible Albedo b1-b11	Optical Grain Radius (μm)[1]	Physical Grain Radius (μm)[2]	Average Radiant Temperature b42, b43, b44 & b46 (°C)[3]	Calculation Error Radiant Temperature b42, b43, b44 & b46 (°C)[3]
1. Summitcrater_snow	green	41	16	39	66	5	~75	250-500	-4	1
2. Below_summit_sw_clean	dark green	30	5	35	77	2	~75	250-500	-2	1
3. Cleansnow_nisqually	blue	21	5	24	82	2	~200	500-1500	1	1
4. Muir_clean2	cyan	26	6	21	65	4	~200	500-1500	2	1
5. Kautz_clean	purple	11	17	28	84	4	~200	500-1500	1	1
6. Emmons_clean	magenta	47	11	41	52	3	~200	500-1500	2	1
7. Dirtysnow_nisqually	red	9	12	18	33	6	~200	500-1500	2	1
8. Muir_dirty1	yellow	21	10	13	34	5	~200	500-1500	3	1
9. Wilson_dirty	orange	31	15	17	40	4	~200	500-1500	2	1
10. Emmons_dirty	mustard	47	6	46	0	0	~200	500-1500	2	1

Notes
1. Optical grain radii were estimated by comparing MASTER-calculated and DISORT-predicted bi-directional reflectance (BDR).
2. Physical grain radii were estimated using ground-truth measurements and relationships between optical and physical grain size from Salisbury et al. [1994].
3. Snow temperatures can exceed the melting point where dirt mixes with snow.

Table 3. Sensor Bands, Wavelengths, and Spatial Resolutions

MASTER
MODIS/ASTER Airborne Simulator

Band	Min (μm)	Max (μm)	Effective Center (μm)	Resolution (m)
1	0.44	0.48	0.46	5-15
2	0.48	0.52	0.50	5-15
3	0.52	0.56	0.54	5-15
4	0.56	0.60	0.58	5-15
5	0.63	0.69	0.66	5-15
6	0.69	0.74	0.71	5-15
7	0.73	0.78	0.75	5-15
8	0.78	0.83	0.80	5-15
9	0.85	0.89	0.87	5-15
10	0.89	0.93	0.91	5-15
11	0.93	0.97	0.95	5-15
12	1.59	1.65	1.62	5-15
13	1.65	1.70	1.68	5-15
14	1.70	1.75	1.73	5-15
15	1.75	1.81	1.78	5-15
16	1.81	1.86	1.83	5-15
17	1.86	1.91	1.88	5-15
18	1.91	1.96	1.93	5-15
19	1.96	2.01	1.98	5-15
20	2.06	2.11	2.08	5-15
21	2.14	2.19	2.17	5-15
22	2.19	2.24	2.22	5-15
23	2.24	2.29	2.26	5-15
24	2.30	2.37	2.33	5-15
25	2.37	2.42	2.39	5-15
26	3.07	3.22	3.14	5-15
27	3.22	3.36	3.28	5-15
28	3.36	3.51	3.44	5-15
29	3.52	3.67	3.59	5-15
30	3.67	3.81	3.74	5-15
31	3.82	3.97	3.89	5-15
32	3.98	4.12	4.05	5-15
33	4.14	4.29	4.21	5-15
34	4.31	4.42	4.36	5-15
35	4.42	4.57	4.50	5-15
36	4.57	4.73	4.65	5-15
37	4.73	4.88	4.80	5-15
38	4.87	5.02	4.95	5-15
39	5.02	5.17	5.09	5-15
40	5.17	5.32	5.24	5-15
41	7.70	8.04	7.86	5-15
42	8.07	8.50	8.28	5-15
43	8.51	8.90	8.71	5-15
44	8.97	9.39	9.18	5-15
45	9.64	10.04	9.82	5-15
46	10.06	10.47	10.26	5-15
47	10.50	11.11	10.80	5-15
48	11.18	11.86	11.51	5-15
49	12.08	12.59	12.33	5-15
50	12.82	13.30	13.06	5-15

Table 3 cont. Sensor Bands, Wavelengths, and Spatial Resolutions

ASTER

Advanced Spaceborne Thermal Emission and Reflection Radiometer

Band	Min (μm)	Max (μm)	Effective Center (μm)	Resolution (m)
1	0.52	0.60	0.56	15
2	0.63	0.69	0.66	15
3	0.76	0.86	0.81	15
4	1.60	1.70	1.65	30
5	2.15	2.19	2.17	30
6	2.19	2.23	2.21	30
7	2.24	2.29	2.26	30
8	2.30	2.37	2.33	30
9	2.36	2.43	2.40	30
10	8.13	8.48	8.29	90
11	8.48	8.83	8.63	90
12	8.93	9.28	9.08	90
13	10.25	10.95	10.66	90
14	10.95	11.65	11.29	90

Landsat 7

Band	Min (μm)	Max (μm)	Effective Center (μm)	Resolution (m)
1	0.45	0.52	0.49	30
2	0.52	0.60	0.56	30
3	0.63	0.69	0.66	30
4	0.76	0.90	0.83	30
5	1.55	1.75	1.65	30
7	2.08	2.35	2.22	30
6	10.40	12.50	11.30	60

Table 4. Airborne and Satellite Data Collected in August, 2001

	Date	Sensor	Line	Time (UTC)	Time (PDT)	TIR Resolution (m)	Logger
Lake Sawyer							
	8/11	ASTER		19:20	12:20	90	C01
	8/11	Landsat 7		18:44	11:44	60	C01
	8/25	MASTER	3-8	18:25	11:24-11:26	5	C01
	8/25	MASTER	4-6	21:37	2:35-2:39	15	C01
	8/27	Landsat 7		18:44	11:44	60	C01
Lake Youngs							
	8/11	ASTER		19:20	12:20	90	LS2
	8/11	Landsat 7		18:44	11:44	60	LS2
	8/25	MASTER	3-10	18:35	11:35-11:37	5	LS2
	8/25	MASTER	3-12	18:48	11:47-11:49	5	LS2
	8/25	MASTER	4-7	21:35	2:42-2:36	15	LS2
	8/25	MASTER	4-8	21:53	2:50-2:56	15	LS2
	8/27	Landsat 7		18:44	11:44	60	LS2
Lake Meridian							
	8/11	ASTER		19:20	12:20	90	LKMR1
	8/11	Landsat 7		18:44	11:44	60	LKMR1
	8/25	MASTER	3-9	18:30	11:30-11:32	5	LKMR1
	8/25	MASTER	4-7	21:40	2:42-2:36	15	LKMR1
	8/25	MASTER	4-8	21:53	2:50-2:56	15	LKMR1
	8/27	Landsat 7		18:44	11:44	60	LKMR1
Green River							
	8/11	ASTER		19:20	12:20	90	GR 3,4,5
	8/11	Landsat 7		18:44	11:44	60	GR 3,4,5
	8/25	MASTER	3-7	18:20	11:18-11:21	5	GR 3,4,5
	8/25	MASTER	4-4	21:15	2:12-2:17	15	GR 3,4,5
	8/27	MASTER	6-1	19:03	12:02-12:05	5	GR 3,4,5
	8/27	Landsat 7		18:44	11:44	60	GR 3,4,5

Table 5. Recommended Atmospheric Corrections (AC) for August, 2001 TIR Data

	Date	Sensor	Line	Time (UTC)	Time (PDT)	Resolution (m)	Atmospheric Correction (AC)
Lake Sawyer							
	8/11	ASTER		19:20	12:20	90	0.75 cm TCW
	8/11	LANDSAT		18:44	11:44	60	0.75 cm TCW
	8/25	MASTER	3-8	18:25	11:24-11:26	5	2cm TCW
	8/25	MASTER	4-6	21:37	2:35-2:39	15	2cm TCW
	8/27	Landsat 7		18:44	11:44	60	do not use[1]
Lake Youngs							
	8/11	ASTER		19:20	12:20	90	0.75 cm TCW
	8/11	LANDSAT		18:44	11:44	60	0.75 cm TCW
	8/25	MASTER	3-10	18:35	11:35-11:37	5	2cm TCW
	8/25	MASTER	3-12	18:48	11:47-11:49	5	2cm TCW
	8/25	MASTER	4-7	21:35	2:42-2:36	15	2cm TCW
	8/25	MASTER	4-8	21:53	2:50-2:56	15	2cm TCW
	8/27	Landsat 7		18:44	11:44	60	do not use[1]
Lake Meridian							
	8/11	ASTER		19:20	12:20	90	0.75 cm TCW
	8/11	LANDSAT		18:44	11:44	60	0.75 cm TCW
	8/25	MASTER	3-9	18:30	11:30-11:32	5	2cm TCW
	8/25	MASTER	4-7	21:40	2:42-2:36	15	2cm TCW
	8/25	MASTER	4-8	21:53	2:50-2:56	15	2cm TCW
	8/27	Landsat 7		18:44	11:44	60	do not use[1]
Green River							
	8/11	ASTER		19:20	12:20	90	
	8/11	LANDSAT		18:44	11:44	60	
	8/25	MASTER	3-7	18:20	11:18-11:21	5	2cm TCW
	8/25	MASTER	4-4	21:15	2:12-2:17	15	2cm TCW
	8/27	MASTER	6-1	19:03	12:02-12:05	5	none?[2]
	8/27	Landsat 7		18:44	11:44	60	do not use[1]

Notes:

1. High cirrus clouds limit the use of the August 27, 2001 Landsat 7 data (Figure17).
2. A balance between absorption and emission at the Green River makes AC difficult to evaluate (Figure16).

Table 6. Total Column Water (TCW) Data from August, 2001

Microtops Observations

Date	Location	# Obs	Total Column Water (cm) Mean	Max	Min	StdDev
08/11/01	Flaming Geyser, Green River	6	1.08	1.15	1.01	0.07
08/25/01	Flaming Geyser, Green River	10	1.14	1.23	1.06	0.07
08/25/01	Whitney Park, Green River	13	1.14	1.19	1.05	0.05
08/26/01	Longmire, Mt. Rainier	6	0.80	0.81	0.78	0.01
08/27/01	Flaming Geyser, Green River	10	1.30	1.46	1.19	0.08
08/28/01	Naches River, Yakima	19	1.03	1.18	0.95	0.06

All Observations

Date	Location	TIME (PDT)	Total Column Water (cm) MM5	Radiosonde	Microtops
08/25/01	Flaming Geyser, Green River	12:00 PM-2:00 PM	2.0-2.2	n/a	1.14
08/25/01	Flaming Geyser, Green River	3:00 PM-5:00 PM	2.2-2.4	n/a	1.14
08/25/01	Quillayute, WA	5:00 PM	2.2-2.4	2.81	n/a
08/25/01	Spokane, WA	5:00 PM	1.6-1.8	1.54	n/a
08/26/01	Longmire, Mt. Rainier	2:00 PM-4:00 PM	1.4-1.6	n/a	0.8
08/26/01	Enumclaw, WA	2:00 PM-3:00 PM	1.8-2.0	n/a	n/a
08/26/01	Enumclaw, WA	4:00 PM-5:00 PM	1.8-2.0	1.85	n/a
08/26/01	Quillayute, WA	5:00 PM	2.0-2.2	2.67	n/a
08/26/01	Spokane, WA	5:00 PM	1.6-1.8	1.84	n/a
08/27/01	Flaming Geyser, Green River	12:00 PM-1:00 PM	2.6-2.8	n/a	1.3
08/27/01	Enumclaw, WA	5:00 PM	2.8-3.0	2.59	n/a
08/27/01	Spokane, WA	5:00 PM	1.8-2.0	1.84	n/a

Table 7. Comparison of Ground-Truth Temperatures with Remotely Sensed Temperatures

Date (2001)	Sensor	Line	Gage Name	$T_{kinetic\text{-}gage}$[2] (°C)	$T_{radiant\text{-}surface}$ (°C)	Error $T_{radiant\text{-}surface}$[3] (°C)	$T_{kinetic\text{-}surface}$ (°C)	Error $T_{kinetic\text{-}surface}$[3] (°C)	Mean No C T_{rs}[5] (°C)	Std. Dev. No C T_{rs}[6] (°C)	Mean EC T_{rs}[6,7] (°C)	Std. Dev. EC T_{rs}[6,7] (°C)	Mean AC T_{rs}[5,8] (°C)	Std. Dev. AC T_{rs}[6,8] (°C)
Lake Sawyer[1]														
8/11	ASTER		C01	n/a[4]	*21*	*1.5*	20.0	0.3	21.5	1.4	22.1	1.3	23.1	0.2
8/11	LANDSAT		C01	n/a[4]	*20*	*1.5*	19.7	0.8	20.9	-	21.8	-	22.9	-
8/25	MASTER	3-8	C01	n/a[4]	*21.5*	2	21.4	0.4	19.2	0.7	20.0	0.3	20.9	0.5
8/25	MASTER	4-6	C01	n/a[4]	*19*	*1.5*	21.3	0.5	18.9	1.0	19.6	0.8	21.5	0.5
8/27	LANDSAT[2]		C01	n/a[4]	*18.5*	2	21.7	0.4	16.7	-	17.5	-	18.2-20.2	-
Lake Younge[1]														
8/11	ASTER		LS2	19.2	n/a[4]	n/a[4]	n/a[4]	n/a[4]	19.1	1.2	19.7	1.1	20.5	0.2
8/11	LANDSAT		LS2	19.0	n/a[4]	n/a[4]	n/a[4]	n/a[4]	18.9	-	19.7	-	20.7	-
8/25	MASTER	3-10	LS2	18.6	n/a[4]	n/a[4]	n/a[4]	n/a[4]	18.2	0.5	18.9	0.4	19.4	0.4
8/25	MASTER	3-12	LS2	18.7	n/a[4]	n/a[4]	n/a[4]	n/a[4]	18.4	0.5	19.1	0.5	19.6	0.5
8/25	MASTER	4-7	LS2	19.5	n/a[4]	n/a[4]	n/a[4]	n/a[4]	17.5	1.0	18.2	0.9	19.7	0.3
8/25	MASTER	4-8	LS2	19.5	n/a[4]	n/a[4]	n/a[4]	n/a[4]	17.3	1.0	18.0	0.9	19.4	0.3
8/27	LANDSAT[2]		LS2	18.6	n/a[4]	n/a[4]	n/a[4]	n/a[4]	13.2	-	14.0	-	14.5-15.0	-
Lake Meridian[1]														
8/11	ASTER		LKMR1	23.4	23.5	0.8	23.6	0.2	22.4	1.4	23.0	1.3	24.1	0.2
8/11	LANDSAT		LKMR1	23.4	*22.5*	*1.5*	23.5	0.3	21.3	-	22.1	-	23.3	-
8/25	MASTER	3-9	LKMR1	21.2	21.5	0.5	21.5	0.3	19.7	0.8	20.5	0.3	21.5	0.4
8/25	MASTER	4-7	LKMR1	21.1	21.5	0.5	22.4	0.7	19.5	1.0	20.2	0.9	22.2	0.5
8/25	MASTER	4-8	LKMR1	21.1	**21.5**	**1.5**	**22.4**	**1**	19.4	1.1	20.2	0.9	22.2	0.4
8/27	LANDSAT[2]		LKMR1	21.7	**21.5**	**1**	21.2	0.6	13.1	-	13.9	-	14.4-14.9	-
GR3/GR4 Green River[1]														
8/11	ASTER		GR3, GR4	17.1	n/a[4]	n/a[4]	n/a[4]	n/a[4]	n/a[9]	n/a[9]	n/a[9]	n/a[9]	n/a[9]	n/a[9]
8/11	LANDSAT		GR3, GR4	16.8	n/a[4]	n/a[4]	n/a[4]	n/a[4]	n/a[9]	n/a[9]	n/a[9]	n/a[9]	n/a[9]	n/a[9]
8/25	MASTER	3-7	GR3, GR4	14.6	**14**	**2**	**14.8**	**0.5**	15.3	0.4	16.0	0.5	15.8	0.5
8/25	MASTER	4-4	GR3, GR4	17	**16.5**	**2**	**16.9**	**0.5**	17.2	0.9	17.9	0.8	19.3	0.8
8/27	MASTER	6-1	GR3, GR4	15.7	n/a[4]	n/a[4]	n/a[4]	n/a[4]	16.0	0.5	16.7	0.5	16.7	0.5
8/27	LANDSAT[2]		GR3, GR4	15.7	n/a[4]	n/a[4]	n/a[4]	n/a[4]	n/a[9]	n/a[9]	n/a[9]	n/a[9]	n/a[9]	n/a[9]
GR5 Green River[1]														
8/11	ASTER		GR5	16.8	n/a[4]	n/a[4]	n/a[4]	n/a[4]	n/a[9]	n/a[9]	n/a[9]	n/a[9]	n/a[9]	n/a[9]
8/11	LANDSAT		GR5	16.4	n/a[4]	n/a[4]	n/a[4]	n/a[4]	n/a[9]	n/a[9]	n/a[9]	n/a[9]	n/a[9]	n/a[9]
8/25	MASTER	3-7	GR5	14.5	**14**	**2**	**14.8**	**0.5**	15.1	0.4	15.8	0.4	15.6	0.5
8/25	MASTER	4-4	GR5	16.7	**16.5**	**2**	**16.9**	**0.5**	16.9	0.7	17.6	0.6	18.9	0.6
8/27	MASTER	6-1	GR5	15.4	n/a[4]	n/a[4]	n/a[4]	n/a[4]	15.7	0.4	16.4	0.4	16.4	0.4
8/27	LANDSAT[2]		GR5	15.4	n/a[4]	n/a[4]	n/a[4]	n/a[4]	n/a[9]	n/a[9]	n/a[9]	n/a[9]	n/a[9]	n/a[9]

Notes:

1. Image temperatures were calculated from regions of interest that included the entire lake, or reach of stream close to gages.
2. The August 27, 2001 Landsat 7 data had high cirrus clouds over the study area.
3. If the measurement was taken concurrently with image data acquisition and showed persistence (within 5 minutes) estimated error was the detector sensitivity (0.5 °C for $T_{radiant\ surface}$, 0.1 °C for $T_{kinetic\text{-}gage}$ and $T_{kinetic\text{-}surface}$) added to the standard deviation over a 5 minute time period. If temperature measurements were not concurrent with the overflight, the closest-time temperature was taken and error was estimated as the spread in temperatures over the closest hour of measurement. Individual error assessments for $T_{kinetic\text{-}gage}$ were not completed. Error was estimated as 0.2 °C for all $T_{kinetic\text{-}gage}$.
4. Data were not available.
5. Image temperatures (T_{rs}) were calculated as the mean in b43, b44, b46, b47 and b48 for MASTER, mean of b13 and b14 for ASTER, and the value in b6 for Landsat 7 (Table 1).
6. Standard deviation across bands is calculated across b42-b48 for MASTER data and b10-b14 for ASTER data. Landsat 7 only has one TIR band so standard deviation could not be calculated (Table 1).
7. Emissivity correction (EC) was applied (Figure 2).
8. Emissivity and atmspheric correction (EC, AC) were applied (Figure 2, Table 3)
9. Temperatures were not calculated because target was unresolved.
10. Ground-truth temperatures in italics were highly variable (i.e., >1 °C variability within 30 minutes).
11. Shaded ground-truth temperatures were single measurements or when measurements were more than 10 minutes away from image data acquisition.

Table 8. Percentage of Remotely Sensed Data Within 1 °C of Ground-Truth

All "good" data[1]

	Percentage within 1 °C					
	No Correction			All Corrections (EC and AC)		
	$T_{gage-kinetic}$	$T_{radiant-surface}$	$T_{kinetic-surface}$	$T_{gage-kinetic}$	$T_{radiant-surface}$	$T_{kinetic-surface}$
All	59%	0%	0%	47%	100%	75%
MASTER 5m	80%	0%	0%	60%	100%	100%
MASTER 15m	33%	0%	0%	33%	100%	100%
ASTER 8/11	50%	0%	0%	50%	100%	50%
Landsat 8/11	50%	n/a[2]	0%	50%	n/a[2]	50%

	Number of Obsevations					
	No Correction			All Corrections (EC and AC)		
	$T_{gage-kinetic}$	$T_{radiant-surface}$	$T_{kinetic-surface}$	$T_{gage-kinetic}$	$T_{radiant-surface}$	$T_{kinetic-surface}$
All	17	3	8	17	3	8
MASTER 5m	5	1	2	5	1	2
MASTER 15m	6	1	2	6	1	2
ASTER 8/11	2	1	2	2	1	2
Landsat 8/11	2	0	2	2	0	2

All data

	Percentage within 1 °C					
	No Correction			All Corrections (EC and AC)		
	$T_{gage-kinetic}$	$T_{radiant-surface}$	$T_{kinetic-surface}$	$T_{gage-kinetic}$	$T_{radiant-surface}$	$T_{kinetic-surface}$
All Data	53%	33%	27%	47%	46%	62%
All MASTER 5m	80%	0%	50%	60%	50%	75%
All MASTER 15m	33%	60%	0%	33%	40%	100%
All ASTER 8/11	50%	50%	0%	50%	50%	50%
All Landsat 8/11	50%	50%	0%	50%	50%	50%
All Landsat 8/27	0%	0%	0%	n/a[2]	n/a[2]	n/a[2]

	Number of Obsevations					
	No Correction			All Corrections (EC and AC)		
	$T_{gage-kinetic}$	$T_{radiant-surface}$	$T_{kinetic-surface}$	$T_{gage-kinetic}$	$T_{radiant-surface}$	$T_{kinetic-surface}$
All Data	19	15	15	17	13	13
All MASTER 5m	5	4	4	5	4	4
All MASTER 15m	6	5	3	6	5	3
All ASTER 8/11	2	2	2	2	2	2
All Landsat 8/11	2	2	2	2	2	2
All Landsat 8/27	2	2	2	0	0	0

Notes:

1. "Good" data were persistent (less 1 °C variability in 30 minutes) and concurrent (within 10 minutes of image data acquisition).
2. No observations were available.
3. Atmospheric and emissivity corrections (EC, AC) are summarized in Figure 2 and Table 3.

Table 9. Summary of Emissivity, Atmospheric, and Surface Effects on August, 2001 TIR Remote-Sensing Data

Factor:	Function of:	How addressed in this study:	Maximum recommended correction or observed effect:	Additional factors to consider:
Emissivity Compensation	wavelength, material properties	laboratory measurements of distilled water (http://speclib.jpl.nasa.gov/)	from 0.6 °C to 0.9 °C (Figure 6a)	Sediment content *(Salisbury and D'Aria,1994)* and roughness *(Torgerson, 2001)* could also be important.
Atmospheric Compensation	wavelength, path length from target to detector, target temperature, vertical distribution in atmospheric radiant temperature and composition (mostly H_20, also O_3 and CO_2)	radiative transfer modeling (e.g., MODTRAN) with atmospheric parameterization from radiosonde, microtops, and numerical weather forecasting model data, in-scene methods [HAC (Kay et al., 2001)]	from -0.2 °C to 2.0 °C (Figure 7a shows both emissivity and atmospheric correction.)	Detector filter function accuracy is critical for spectrally resampling MODTRAN output.
Multiple Scattering	detector viewing angle, target reflectance, near-bank temperature	ground-based FLIR measurements	3 °C Green River (Figure 20)	Multiple scattering is probably less important for nadir views (i. e., most remote sensing data).
Evaporative Cooling	wind speed, exposure	ground-based radiant temperature measurements	3.5 °C Lake Sawyer (Figure 10)	Observed effects could be related to detector instability.

Bibliography

Anderson, G. P., Chetwynd, J.H., Kenizys, F. X., Shettle, E. P., Abereu, F. X., Gallery, W. O., Selby, J. E. A., and S.A. Clough, Archarya, P. K., Berk, A., Bernstein, L. S., Matthew, M. W., Adler-Golden, S. M., and Robertson, D. C. (1998). *MODTRAN User's Manual Versions 3.7 and 4.0 - December 1, 1998 Draft*, Air Force Research Laboratory.

Bechta, R.L. (1997). Riparian shade and stream temperature: an alternate perspective. *Rangelands*, 19, 25-28.

V. Carrere, V., and Conel, J. E. (1993). Recovery of atmospheric water vapor total column abundance from imaging spectrometer data around 940 nm – sensitivity analysis and application to airborne visible/infrared imaging spectrometer data. *Remote Sensing of Environment*, 44,179-204.

Colbeck, S. C. (1982). An overview of seasonal snow metamorphism. *Reviews of Geophysics and Space Physics*, 20, 45-61.

Dozier, J., and Warren, S. (1982). Effect of viewing angle on the infrared brightness temperature of snow. *Water Resources Research*, 18, 1424-1434.

Driedger, C. (1981). Effect of ash thickness on snow ablation. *The 1980 Eruptions of Mt. St. Helens Washington, USGS Professional Paper 1250,* Lipman, P.W. and Mullineaux, D. R. (Ed.), 757-760.

Emery, W. J., and Yu. , Y. (1997). Satellite sea surface temperature patterns. *International. Journal of Remote Sensing,* 18:2, 323-334.

Gao, B. C., and Goetz, A. F. H. (1990). Column atmospheric water vapor and vegetation liquid water retrievals from airborne imaging spectrometer data. *Journal of Geophysical Research*, 95, 3549-3564.

Gillespie, A. R. (1992). Spectral mixture analysis of multispectral thermal infrared images," *Remote Sensing of Environment,* 42, 137-145.

Gu, D., Gillespie, A. R., Kahle, A. B., and Palluconi, F. D. (2000). Autonomous atmospheric compensation (AAC) of high resolution hyperspectral thermal infrared remote sensing imagery. *IEEE Transactions on Geoscience and Remote Sensing*, 38:6, 2557-2570.

Higuchi, K., and Nagoshi, A. (1975). Effect of particulate matter in surface snow layers on the albedo of perennial snow patches. *Isotopes and Impurities in Snow and Ice Symposium, IAHS-AISH Publication No. 118, Proceedings of the Grenoble Symposium*, 95-98.

Hook, S., Myers, J., Thome, K, Fitzgerald, M., and Kahle, A. (2001). The MODIS/ASTER airborne simulator (MASTER) - a new instrument for earth science studies. *Remote Sensing of Environment*, 76, 93-102.

Houghton, J.T., Ding, Y., Griggs, D.J. , Noguer, M., Van der Linden, P. J. , and Xiaosu, D. (Eds.) (2001). Climate Change 2001: The Scientific Basis Contribution of Working Group I to the Third Assessment Report of the Intergovernmental Panel on Climate Change (IPCC). Cambridge University Press, UK.

Johnson, B. R. (1998) In-scene Atmospheric Compensation: Application to SEBASS data collected at the ARM site. *Aerospace Report No. ATR-99 (8407)-1 Part I.*

Kay, J. E., Handcock, R. N., Gillespie, A. R., Konrad, C., Burges, S., Naveh, N. and Booth., D. (2001). Stream-temperature estimation from thermal infrared images. *International Geoscience and Remote Sensing Symposium*, abstract.

Kidder, S Q., and T. H. Vonder Haar. (1995). Satellite Meteorology: An Introduction, Academic Press.

Kou, L., D. Labrie, and P. Chylek (1993). Refractive indices of water and ice in the 0.65– to 2.5-μm spectral range. *Appl. Optics, 32*, 3531–3540.

LeDrew, E. F., and Franklin, S. E. (1985). The use of thermal infrared imagery in surface current analysis of a small lake. *Photogrammetric Engineering and Remote Sensing*, 51, 565-573.

Larson, L.L., and Larson, S. E. (1996). Riparian shade and stream temperature: A perspective. *Rangelands*, 18: 149-152.

McMillin, L. M., and Crosby, D. S. (1984). Theory and validation of the multiple window sea surface temperature. *Journal of Geophysical Research*, 89, 3655-3661.

Nolin, A., and Dozier, J. (1993). Estimating snow grain size using AVIRIS data. *Remote Sensing of Environment,* 44, 231-238.

Nolin, A., and Dozier, J. (2000). A hyperspectral method for remote sensing of the grain size of snow. *Remote Sensing of Environment*, 74, 207-216.

Ontar Corporation (2001) PcModWin v 4.0, Village Way, North Andover, MA, 01845, USA.

Poole, G. C., and Berman, C. H. (2001). An ecological perspective on in-stream temperature: natural heat dynamics and mechanisms of human-caused thermal degradation, *Environmental Management*, 27:6, 787-802.

Raup, B., Kieffer, H., Barry, R., Kaab, A., Kargel, J., Khalso, S. J. S., Troisi, V., Wang, I., and Wessels, R. (2001) The GLIMS database: scientific considerations in the design of a global glacier data archive. *International Glaciological Society 4th International Symposium on Remote Sensing in Glaciology*, 114.

Research Systems, Inc., The Environment for Visualizing Images (ENVI). (2001). 4990 Pearl East Circle, Boulder, CO, 80301, USA, 2001.

Robinson, D. A. (1997). Hemispheric snow cover and surface albedo for model validation. *Annals of Glaciology*, 25, 241-245.

Salisbury, J. W. and D'Aria, D. M. (1992). Emissivity of terrestrial materials in the 8-14 μm atmospheric window. *Remote Sensing of Environment,* 42, 83-106.

Salisbury, J. W., D'Aria, D. M., and Wald, A. (1994). Measurements of thermal infrared spectral reflectance of frost, snow, and ice. *Journal of Geophysical Research*, 99, 24,235-24,240.

Schott, J. R., Barsi, J. A., Raqueno, N. G., and Alwis, D. D. (2001). Calibration of Landsat thermal data and application to water resource studies, *Remote Sensing of Environment*, 78, 108-117.

Smith, W.L., Knuteson, R. O., and Revercomb, H. E. (1996). Observations of the infrared radiative properties of the ocean: Implications for the measurement of sea surface temperature via satellite remote sensing. *Bulletin of the American Meteorogical Society,* 77, 41-51.

Stamnes, K, Tsay, S., Wiscombe, W., and Jayaweera, K. (1988). Numerically stable algorithm for discrete-ordinate-method radiative transfer in multiple scattering and emitting layered media. *Applied Optics*, 27, 2502-2509.

Torgersen, C. E., Faux, R. N., McIntosh, B. A., Poage, N. J., and Norton, D. J. (2001). Airborne thermal remote sensing for water temperature assessment in rivers and streams, *Remote Sensing of Environment*, 76, 386-398.

Warren, S. (1982). Optical properties of snow. *Reviews of Geophysics and Space Physics*, 20, 67-89.

Warren, S., and Wiscombe, W. (1981). A model for the spectral albedo of snow II. Snow containing atmospheric aerosols. *Journal of the Atmospheric Sciences*, 37, 2,734-2,745.

Warren, S. G., Brandt, R. E., and Hinton, P.O. (1998). Effect of surface roughness on bi-directional reflectance of Antarctic snow. *Journal of Geophysical Research*, 103, 25,789-25,807.

Wiscombe, W. J. (1980). Improved Mie scattering algorithms. *Applied Optics*, 19, 1505–1509.

Wiscombe, W., and Warren, S. (1980). A model for the spectral albedo of snow. I. Pure Snow. *Journal of the Atmospheric Sciences*, 37, 2,712-2,733.

Young, S. J. (1998). In-scene Atmospheric Compensation: Application to SEBASS data collected at the ARM site, *Aerospace Report No. ATR-99 (8407)-1 Part II.*

Appendix A. MODTRAN Runs for Mt. Rainier

Location:	**Louise Lake**	**Paradise**	**Panorama Point**	**Kautz Glacier**
MODTRAN output file names	radiosonde_louiselake radiosonde_louiselake_20 radiosonde_louiselake_40	radiosonde_paradise radiosonde_paradise_20 radiosonde_paradise_40	radiosonde_panpoint radiosonde_panpoint_20 radiosonde_panpoint_40	radiosonde_kautz radiosonde_kautz_20 radiosonde_kautz_40
MODTRAN Prompt:	**Input:**			
Calculation Option	MODTRAN	MODTRAN	MODTRAN	MODTRAN
Model Atmosphere	User Specified	User Specified	User Specified	User Specified
Type of Atmospheric Path	Slant Path	Slant Path	Slant Path	Slant Path
Mode of Execution	Radiance w/scattering	Radiance w/scattering	Radiance w/scattering	Radiance w/scattering
Execute with Multiple Scattering	MS on Scattering at Observer	MS on Scattering at Observer	MS on Scattering at Observer	MS on Scattering at Observer
Atmospheric Profiles	aug26_rainier.csv	aug26_rainier.csv	aug26_rainier.csv	aug26_rainier.csv
CO_2 concentration	365 ppm	365 ppm	365 ppm	365 ppm
Total Column Water (g/cm^2)	Use default	Use default	Use default	Use default
Use Instrument Filter File	none	none	none	none
Scattering algorithm	modtran 2	modtran 2	modtran 2	modtran 2
Temperature at First Boundary	0	0	0	0
Surface Albedo Flag	Surface Albedo Value	Surface Albedo Value	Surface Albedo Value	Surface Albedo Value
Surface Albedo	0.02	0.02	0.02	0.02
Atmospheric Parameters - do not scale TOA irradiance File Sun 2				
Aerosol Model Used	Rural - VIS 23km	Rural - VIS 23km	Rural - VIS 23km	Rural - VIS 23km
Seasonal Modification	Spring-Summer	Spring-Summer	Spring-Summer	Spring-Summer
Upper Atmosphere Aerosols	Background Stratospheric	Background Stratospheric	Background Stratospheric	Background Stratospheric
GRNDALTABOVE SEALEVEL	1.4	1.645	2	2.438
Observer Height	9.5	9.5	9.5	9.5
Final Height (km)	1.4	1.645	2	2.438
Zenith Angle	0°, 20°, 40°	0°, 20°, 40°	0°, 20°, 40°	0°, 20°, 40°
Wavelength Coverage	from 0.4 to 13.5 micrometers	from 0.4 to 13.5 micrometers	from 0.4 to 13.5 micrometers	from 0.4 to 13.5 micrometers
default frequency increment	(1 1/cm .00048um)	(1 1/cm .00048um)	(1 1/cm .00048um)	(1 1/cm .00048um)
default FWHM	(1 1/cm - .014411 um)	(1 1/cm - .014411 um)	(1 1/cm - .014411 um)	(1 1/cm - .014411 um)
Solar/Lunar Geometry Type	Option Azimuth and Zenith Angle	Option Azimuth and Zenith Angle	Option Azimuth and Zenith Angle	Option Azimuth and Zenith Angle
Aerosol Phase Function	MIE Generated	MIE Generated	MIE Generated	MIE Generated
Day of year	237	237	237	237
Solar Zenith Angle	37	37	37	37
Azimuth Angle at Observer	-164	-164	-164	-164

Appendix A Cont. MODTRAN Runs for Mt. Rainier

Location	**Camp Muir**	**Sunset Ampitheater**	**Summit**
MODTRAN output file names	radiosonde_muir radiosonde_muir_20 radiosonde_muir_40	radiosonde_sunsetamp radiosonde_sunsetamp_20 radiosonde_sunsetamp_40	radiosonde_summit radiosonde_summit_20 radiosonde_summit_40
MODTRAN Prompt:	**Input:**		
Calculation Option	MODTRAN	MODTRAN	MODTRAN
Model Atmosphere	User Specified	User Specified	User Specified
Type of Atmospheric Path	Slant Path	Slant Path	Slant Path
Mode of Execution	Radiance w/scattering	Radiance w/scattering	Radiance w/scattering
Execute with Multiple Scattering	MS on Scattering at Observer	MS on Scattering at Observer	MS on Scattering at Observer
Atmospheric Profiles	aug26_rainier.csv	aug26_rainier.csv	aug26_rainier.csv
CO_2 concentration	365 ppm	365 ppm	365 ppm
Total Column Water (g/cm^2)	Use default	Use default	Use default
Use Instrument Filter File	none	none	none
Scattering algorithm	modtran 2	modtran 2	modtran 2
Temperature at First Boundary	0	0	0
Surface Albedo Flag	Surface Albedo Value	Surface Albedo Value	Surface Albedo Value
Surface Albedo	0.02	0.02	0.02
Atmospheric Parameters - do not scale TOA irradiance			
File Sun 2			
Aerosol Model Used	Rural - VIS 23km	Rural - VIS 23km	Rural - VIS 23km
Seasonal Modification	Spring-Summer	Spring-Summer	Spring-Summer
Upper Atmosphere Aerosols	Background Stratospheric	Background Stratospheric	Background Stratospheric
GRNDALTABOVE SEALEVEL	3.105	3.72	4.393
Observer Height	9.5	9.5	9.5
Final Height (km)	3.105	3.72	4.393
Zenith Angle	0º, 20º, 40º	0º, 20º, 40º	0º, 20º, 40º
Wavelength Coverage	from 0.4 to 13.5 micrometers	from 0.4 to 13.5 micrometers	from 0.4 to 13.5 micrometers
default frequency increment	(1 1/cm .00048um)	(1 1/cm .00048um)	(1 1/cm .00048um)
default FWHM	(1 1/cm - .014411 um)	(1 1/cm - .014411 um)	(1 1/cm - .014411 um)
Solar/Lunar Geometry Type	Option Azimuth and Zenith Angle	Option Azimuth and Zenith Angle	Option Azimuth and Zenith Angle
Aerosol Phase Function	MIE Generated	MIE Generated	MIE Generated
Day of year	237	237	237
Solar Zenith Angle	37	37	37
Azimuth Angle at Observer	-164	-164	-164

MODTRAN OUTPUT

Path Thermal Radiance ($Wm^{-2}sr^{-1}(cm^{-1})^{-1}$)
radiance emitted by the path constituents (atmospheric gases, as well as aerosols) that is seen at the observer

Total Transmissivity
total path transmission from the observer to the start of the path

Appendix B. MODTRAN Runs for August 11, 2001 TIR Data (ASTER/Landsat 7)

MODTRAN output name	aug11_0.5_flam	aug11_0.75_flam	aug11_mtps_flam	aug11_2.0_flam	aug11_std_flam
MODTRAN OPTION:					
Calculation Option	MODTRAN	MODTRAN	MODTRAN	MODTRAN	MODTRAN
Model Atmosphere	Mid-Latitude Summer	Mid-Latitude Summer	Mid-Latitude Summer	Mid-Latitude Summer	Mid-Latitude Summer
Type of Atmospheric Path	Slant Path	Slant Path	Slant Path	Slant Path	Slant Path
Mode of Execution	Radiance w/scattering	Radiance w/scattering	Radiance w/scattering	Radiance w/scattering	Radiance w/scattering
Execute with Multiple Scattering	MS on Scattering at Observer	MS on Scattering at Observer	MS on Scattering at Observer	MS on Scattering at Observer	MS on Scattering at Observer
Atmospheric Profiles	Default to Model	Default to Model	Default to Model	Default to Model	Default to Model
WaterVapor Column Choices	0.5 - gm/cm^2	1 - gm/cm^2	1.08 gm/cm^2- microtops	2 - gm/cm^2	Use Default water vapor column
Ozone default ozone column	Use Default ozone column	Use Default ozone column	Use Default ozone column	Use Default ozone column	Use Default ozone column
Use Instrument Filter File	none	none	none	none	none
Carbon Dioxide	365	365	365	365	365
Scattering Algorithm	Modtran 2	Modtran 2	Modtran 2	Modtran 2	Modtran 2
Temperature at First Boundary	293	293	293	293	293
Surface Albedo Flag	Surface Albedo Value	Surface Albedo Value	Surface Albedo Value	Surface Albedo Value	Surface Albedo Value
Surface Albedo	0	0	0	0	0
Solar Irradiance Source	File Sun 2	File Sun 2	File Sun 2	File Sun 2	File Sun 2
Top of Atmopshere Parameters	Do not scale TOA irradiance	Do not scale TOA irradiance	Do not scale TOA irradiance	Do not scale TOA Irradiance	Do not scale TOA irradiance
Triangular Filter Width	5	5	5	5	5
Aerosol Model Used	Rural - VIS 23km	Rural - VIS 23km	Rural - VIS 23km	Rural - VIS 23km	Rural - VIS 23km
Seasonal Modification to Aerosol	Spring-Summer	Spring-Summer	Spring-Summer	Spring-Summer	Spring-Summer
Upper Atmosphere Aerosols	Background Stratospheric	Background Stratospheric	Background Stratospheric	Background Stratospheric	Background Stratospheric
Surface Range for Boundar Layer	0	0	0	0	0
GNDALT (Altitude above sea level)	0.056	0.056	0.056	0.056	0.056
all rest default					
Path Type: Observer, Zenith < and Final					
Observer Height (km) - detector	0	0	0	0	100
Final Height (km) - surface elevation	0.056	0.056	0.056	0.056	0.056
Zenith Angle - Note: 180=nadir	180	180	180	180	180
Wavelength Coverage	from 0.4 to 13.5 micrometers	from 0.4 to 13.5 micrometers	from 0.4 to 13.5 micrometers	from 0.4 to 13.5 micrometers	from 0.4 to 13.5 micrometers
default frequency increment	(1 1/cm .00048um)	(1 1/cm .00048um)	(1 1/cm .00048um)	(1 1/cm .00048um)	(1 1/cm .00048um)
default FWHM	(1 1/cm - .014411 um)	(1 1/cm - .014411 um)	(1 1/cm - .014411 um)	(1 1/cm - .014411 um)	(1 1/cm - .014411 um)
SA. Geometry Type:					
Aerosol Phase Function	MIE Generated	MIE Generated	MIE Generated	MIE Generated	MIE Generated
Day of year	222	222	222	222	222
Azimuth Angle at Observer (UTC 21)	175.82	175.82	175.82	175.82	175.82
Solar Zenith Angle (UTC 21)	32.27	32.27	32.27	32.27	32.27

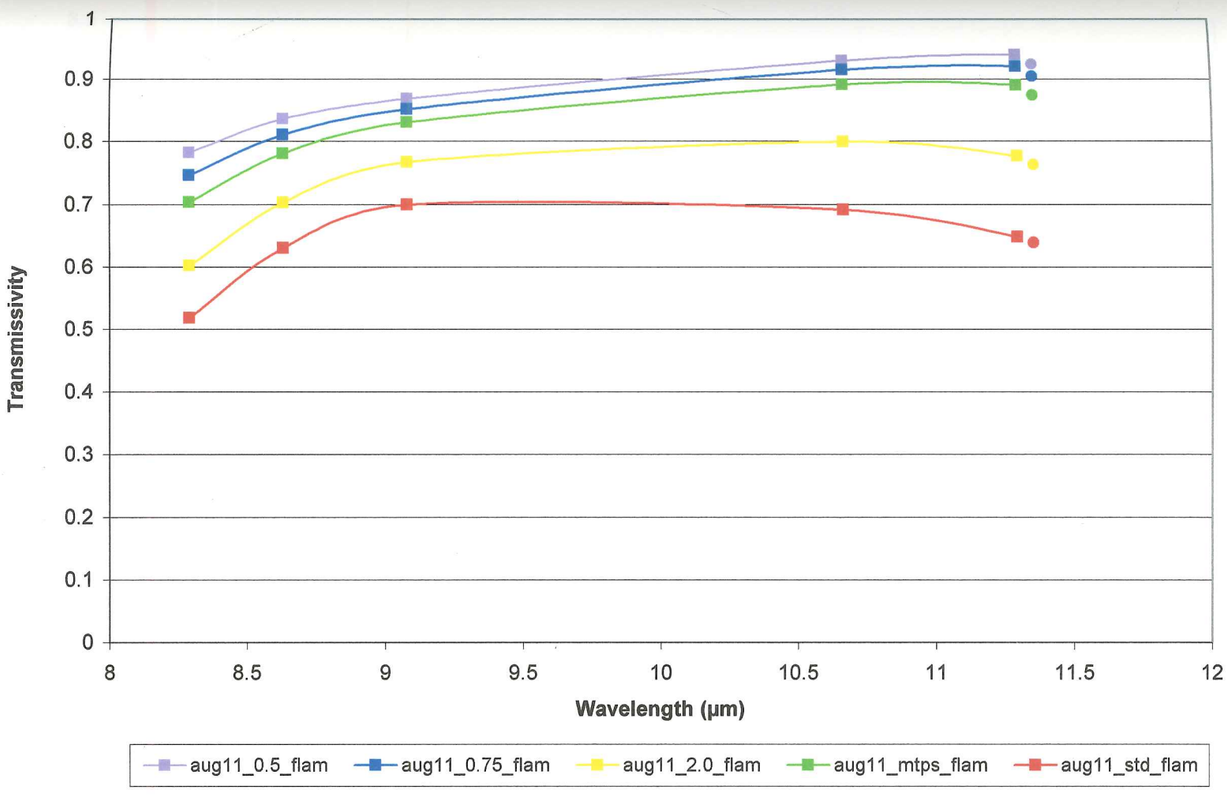

Appendix B. August 11, 2001 ASTER/Landsat 7 Transmissivity

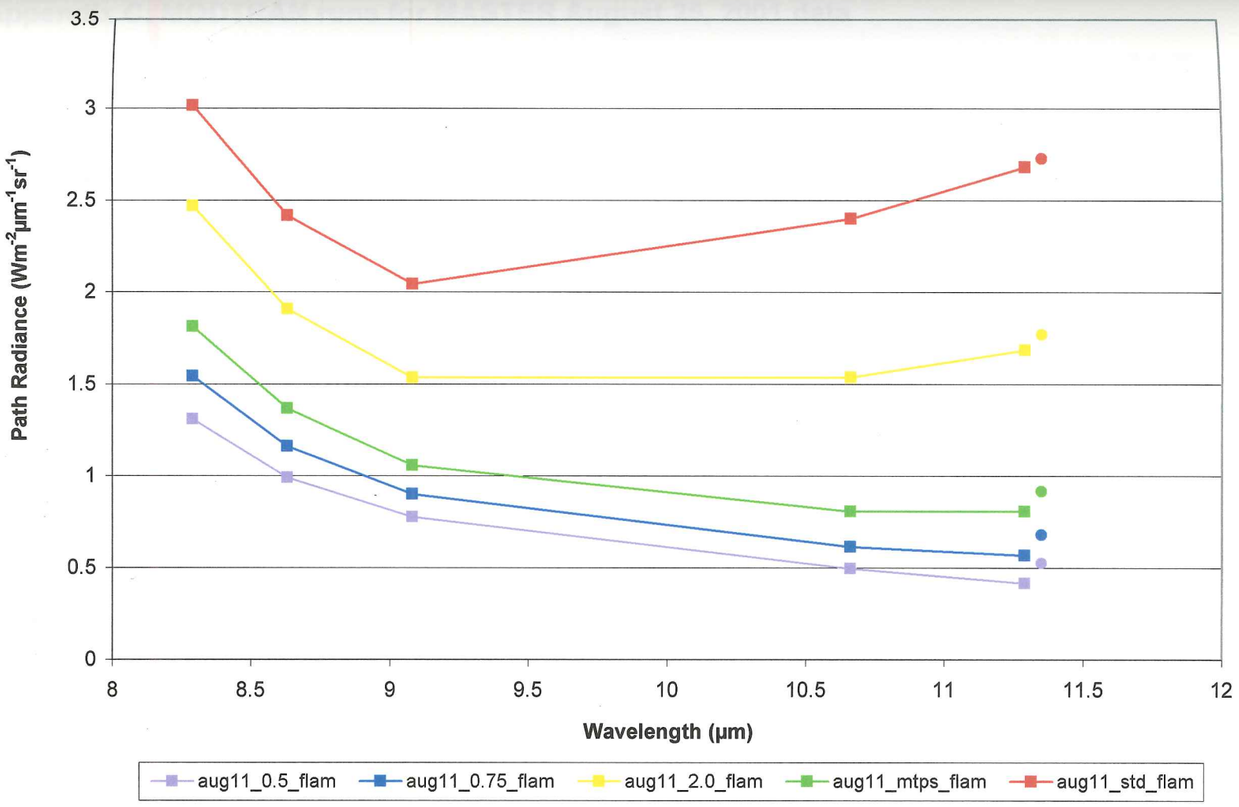

Appendix B. August 11, 2001 ASTER/Landsat 7 Path Radiance

Appendix C. MODTRAN runs for MASTER August 25, 2001 data

MODTRAN output name (plus 5m or 16m)	**aug25_0.6_flam aug25_0.6_ys**	**aug25_mtps_flam aug25_mtps_ys**	**aug25_2.0_flam aug25_2.0_ys**	**aug25_mm5_flam aug25_mm5_ys**	**aug25_std_flam aug25_std_ys**
MODTRAN OPTION:					
Calculation Option	MODTRAN	MODTRAN	MODTRAN	MODTRAN	MODTRAN
Model Atmosphere	Mid-Latitude Summer	Mid-Latitude Summer	Mid-Latitude Summer	Mid-Latitude Summer	Mid-Latitude Summer
Type of Atmospheric Path	Slant Path	Slant Path	Slant Path	Slant Path	Slant Path
Mode of Execution	Radiance w/scattering	Radiance w/scattering	Radiance w/scattering	Radiance w/scattering	Radiance w/scattering
Execute with Multiple Scattering	MS on Scattering at Observer	MS on Scattering at Observer	MS on Scattering at Observer	MS on Scattering at Observer	MS on Scattering at Observer
Atmospheric Profiles	Default to Model for all profiles	Default to Model for all profiles	Default to Model for all profiles	Default to Model for all profiles	Default to Model for all profiles
WaterVapor Column Choices	0.5 - gm/cm^2	1.2 gm/cm^2- microtops	2 - gm/cm^2	Default to Model for all profiles	Use Default water vapor column
Ozone default ozone column	Use Default ozone column	Use Default ozone column	Use Default ozone column	Use Default ozone column	Use Default ozone column
Use Instrument Filter File	none	none	none	aug25_greenmm5.csv	none
Carbon Dioxide	365	365	365	365	365
Scattering Algorithm	Scattering algorithm - modtran 2	Scattering algorithm - modtran 2	Scattering algorithm - modtran 2	Scattering algorithm - modtran 2	Scattering algorithm - modtran 2
Temperature at First Boundary	296	296	296	296	296
Surface Albedo Flag	Surface Albedo Value	Surface Albedo Value	Surface Albedo Value	Surface Albedo Value	Surface Albedo Value
Surface Albedo	0	0	0.02	0.02	0
Solar Irradiance Source	File Sun 2	File Sun 2	File Sun 2	File Sun 2	File Sun 2
Top of Atmopshere Parameters	Do not scale TOA irradiance	Do not scale TOA irradiance	Do not scale TOA irradiance	Do not scale TOA irradiance	Do not scale TOA irradiance
Triangular Filter Width	5	5	5	5	5
Aerosol Model Used	Rural - VIS 23km	Rural - VIS 23km	Rural - VIS 23km	Rural - VIS 23km	Rural - VIS 23km
Seasonal Modification to Aerosol	Spring-Summer	Spring-Summer	Spring-Summer	Spring-Summer	Spring-Summer
Upper Atmosphere Aerosols	Background Stratospheric	Background Stratospheric	Background Stratospheric	Background Stratospheric	Background Stratospheric
Surface Range for Boundar Layer	0	0	0	0	0
GNDALT (Altitude above sea level)	0.1524 OR 0.056	0.1524 or 0.056	0.1524 or 0.056	0.1524 or 0.056	0.1524 or 0.056
all rest default					
Path Type: Observer, Zenith < and Final					
Observer Height (km) - detector	1.98 OR 6.331	1.98 OR 6.329	1.98 OR 6.333	1.98 OR 6.330	1.98 OR 6.328
Final Height (km) - surface elevation	0.1524 OR 0.059	0.1524 OR 0.057	0.1524 OR 0.061	0.1524 OR 0.058	0.1524 OR 0.056
Zenith Angle - Note: 180=nadir	160	180	180	180	180
Wavelength Coverage	from 0.4 to 13.5 micrometers	from 0.4 to 13.5 micrometers	from 0.4 to 13.5 micrometers	from 0.4 to 13.5 micrometers	from 0.4 to 13.5 micrometers
default frequency increment	(1 1/cm .00048um)	(1 1/cm .00048um)	(1 1/cm .00048um)	(1 1/cm .00048um)	(1 1/cm .00048um)
default FWHM	(1 1/cm - .014411 um)	(1 1/cm - .014411 um)	(1 1/cm - .014411 um)	(1 1/cm - .014411 um)	(1 1/cm - .014411 um)
S/L Geometry Type:	Option Azimuth and Zenith Angle	Option Azimuth and Zenith Angle	Option Azimuth and Zenith Angle	Option Azimuth and Zenith Angle	Option Azimuth and Zenith Angle
Aerosol Phase Function	MIE Generated	MIE Generated	MIE Generated	MIE Generated	MIE Generated
Day of year	234	234	234	234	234
Azimuth Angle at Observer (UTC 21)	-158.4	-158.4	-158.4	-158.4	-158.4
Solar Zenith Angle (UTC 21)	38.5	38.5	38.5	38.5	38.5

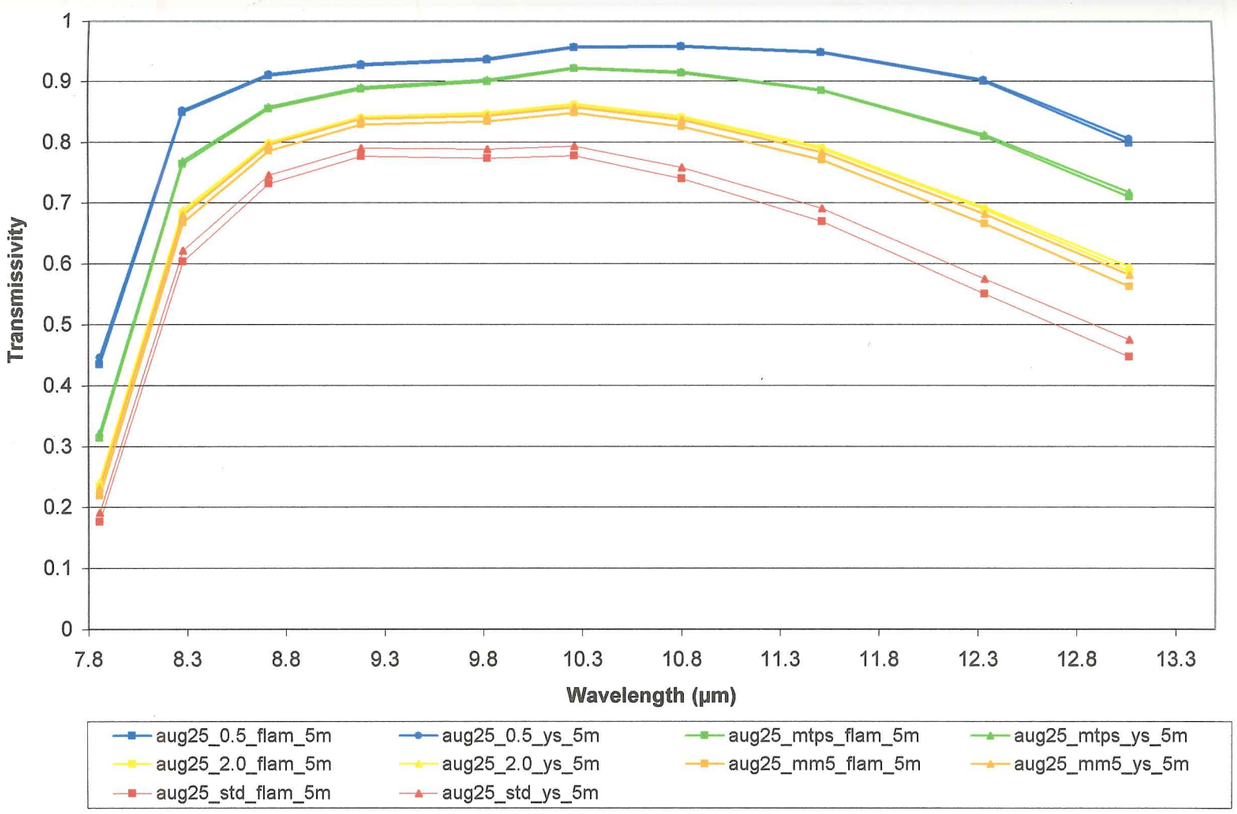

Appendix C. August 25, 2001 - 5m MASTER Transmissivity

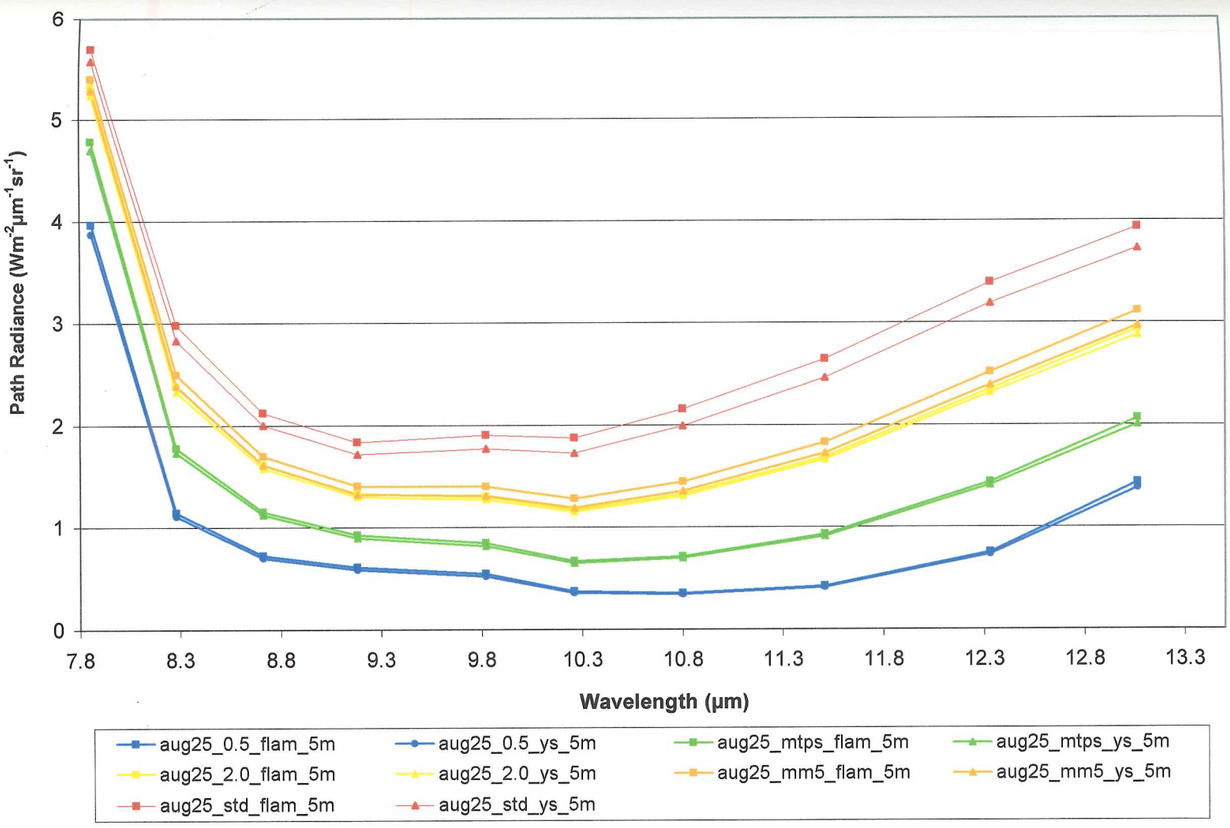

Appendix C. August 25, 2001 - 5m MASTER Path Radiance

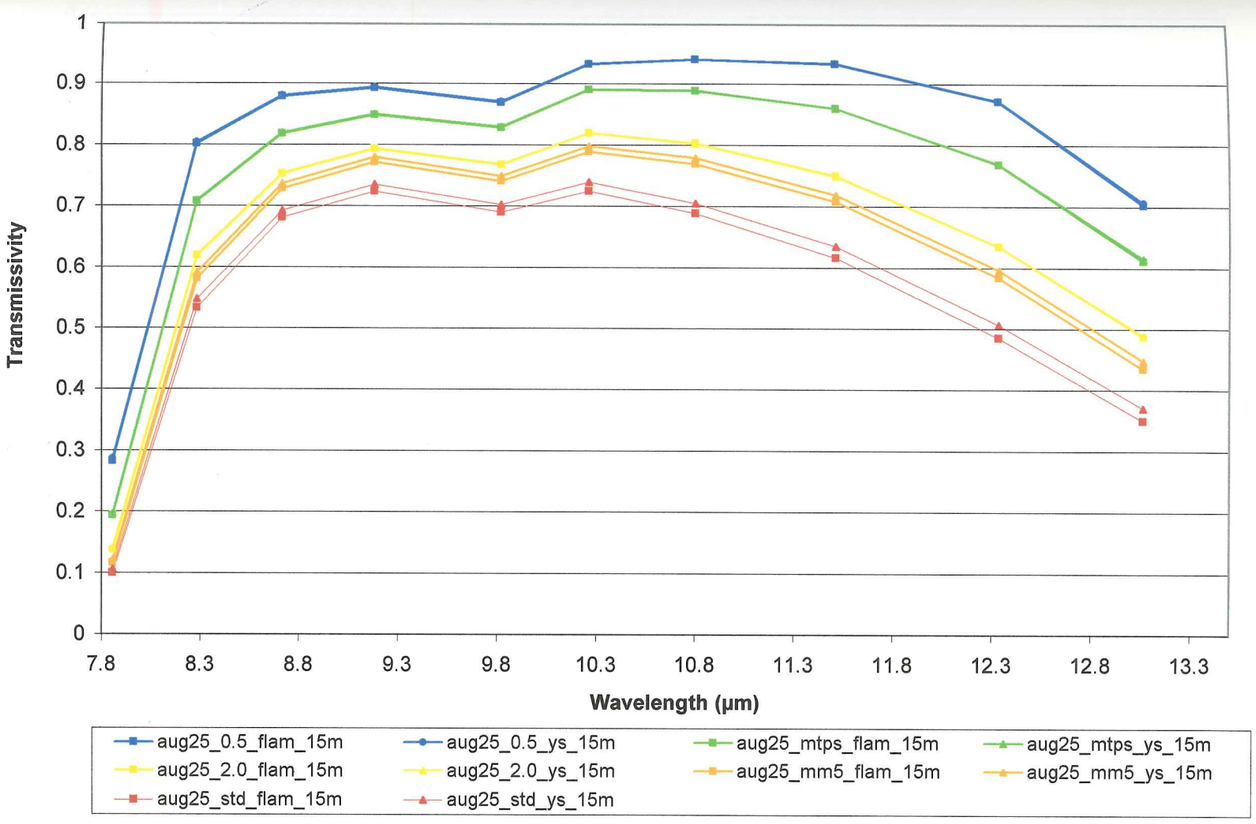

Appendix C. August 25, 2001 - 15m MASTER Transmissivity

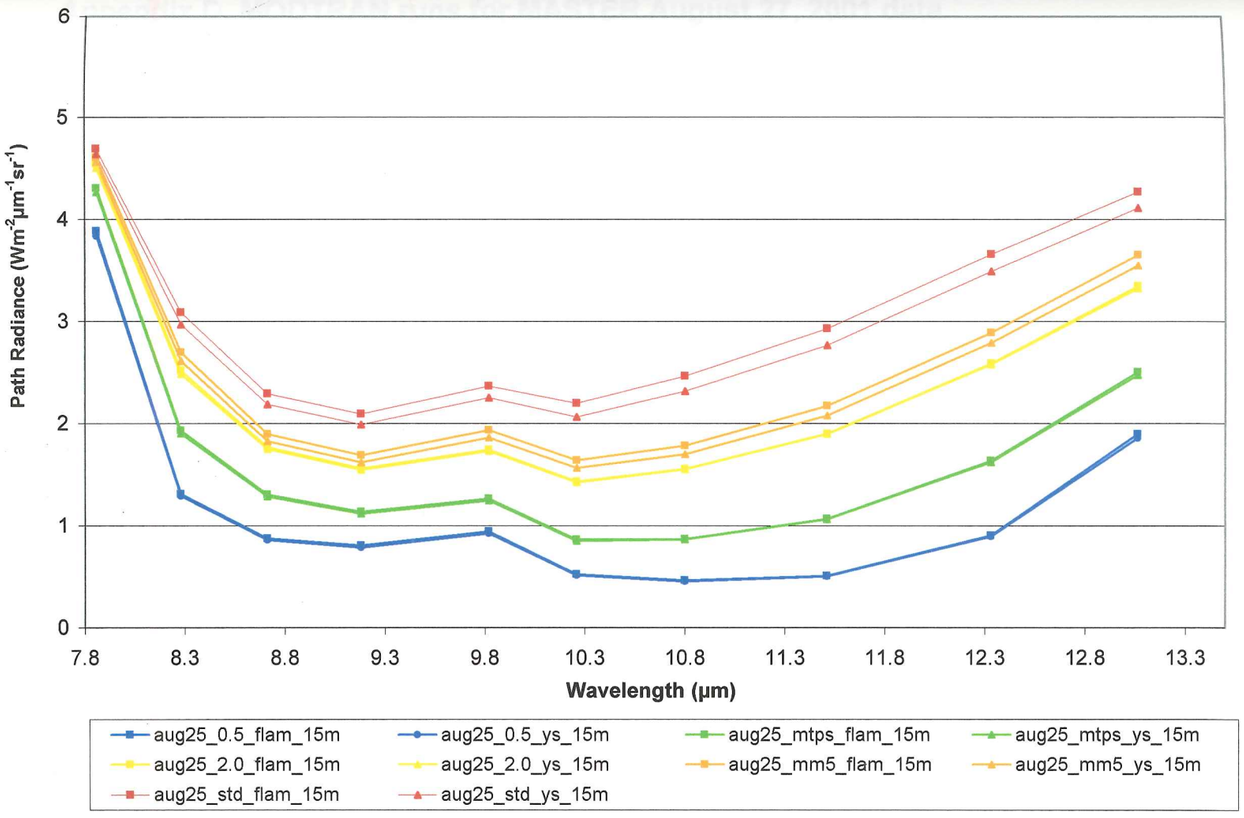

Appendix C. August 25, 2001 - 15m MASTER Path Radiance

Appendix D. MODTRAN runs for MASTER August 27, 2001 data

MODTRAN output name (_5m or _ASTER)	**aug27_0.5_ys aug27_0.5_flam**	**aug27_mtps_ys aug27_mtps_flam**	**aug27_2.0_ys aug27_2.0_flam**	**aug27_std_ys aug27_std_flam**
MODTRAN OPTION:				
Calculation Option	MODTRAN	MODTRAN	MODTRAN	MODTRAN
Model Atmosphere	Mid-Latitude Summer	Mid-Latitude Summer	Mid-Latitude Summer	Mid-Latitude Summer
Type of Atmospheric Path	Slant Path	Slant Path	Slant Path	Slant Path
Mode of Execution	Radiance w/scattering	Radiance w/scattering	Radiance w/scattering	Radiance w/scattering
Execute with Multiple Scattering	MS on Scattering at Observer	MS on Scattering at Observer	MS on Scattering at Observer	MS on Scattering at Observer
Atmospheric Profiles	Default to Model for all profiles	Default to Model for all profiles	Default to Model for all profiles	Default to Model for all profiles
WaterVapor Column Choices	0.5 - gm/cm^2	1.3 gm/cm^2- microtops	2 - gm/cm^2	Use Default water vapor column
Ozone default ozone column	Use Default ozone column	Use Default ozone column	Use Default ozone column	Use Default ozone column
Use Instrument Filter File	none	none	none	none
Carbon Dioxide	365	365	365	365
Scattering Algorithm	Scattering algorithm - modtran 2	Scattering algorithm - modtran 2	Scattering algorithm - modtran 2	Scattering algorithm - modtran 2
Temperature at First Boundary	293	293	293	293
Surface Albedo Flag	Surface Albedo Value	Surface Albedo Value	Surface Albedo Value	Surface Albedo Value
Surface Albedo	0	0	0.02	0
Solar Irradiance Source	File Sun 2	File Sun 2	File Sun 2	File Sun 2
Top of Atmopshere Parameters	Do not scale TOA irradiance	Do not scale TOA irradiance	Do not scale TOA irradiance	Do not scale TOA irradiance
Triangular Filter Width	5	5	5	5
Aerosol Model Used	Rural - VIS 23km	Rural - VIS 23km	Rural - VIS 23km	Rural - VIS 23km
Seasonal Modification to Aerosol	Spring-Summer	Spring-Summer	Spring-Summer	Spring-Summer
Upper Atmosphere Aerosols	Background Stratospheric	Background Stratospheric	Background Stratospheric	Background Stratospheric
Surface Range for Boundar Layer	0	0	0	0
GNDALT (Alititude above sea level)	0.056	0.056	0.056	0.056 or 0.1524
all rest default				
Path Type: Observer, Zenith < and Final				
Observer Height (km) - detector	1.98 OR 100	1.98 OR 100	1.98 OR 100	1.98 OR 100
Final Height (km) - surface elevation	0.056	0.056	0.056	0.056
Zenith Angle - Note: 180=nadir	160	180	180	180
Wavelength Coverage	from 0.4 to 13.5 micrometers	from 0.4 to 13.5 micrometers	from 0.4 to 13.5 micrometers	from 0.4 to 13.5 micrometers
default frequency increment	(1 1/cm .00048um)	(1 1/cm .00048um)	(1 1/cm .00048um)	(1 1/cm .00048um)
default FWHM	(1 1/cm - .014411 um)	(1 1/cm - .014411 um)	(1 1/cm - .014411 um)	(1 1/cm - .014411 um)
S/L Geometry Type:	Option Azimuth and Zenith Angle	Option Azimuth and Zenith Angle	Option Azimuth and Zenith Angle	Option Azimuth and Zenith Angle
Aerosol Phase Function	MIE Generated	MIE Generated	MIE Generated	MIE Generated
Day of year	236	236	236	236
Azimuth Angle at Observer (UTC 21)	177.75	177.75	177.75	177.75
Solar Zenith Angle (UTC 21)	37.46	37.46	37.46	37.46

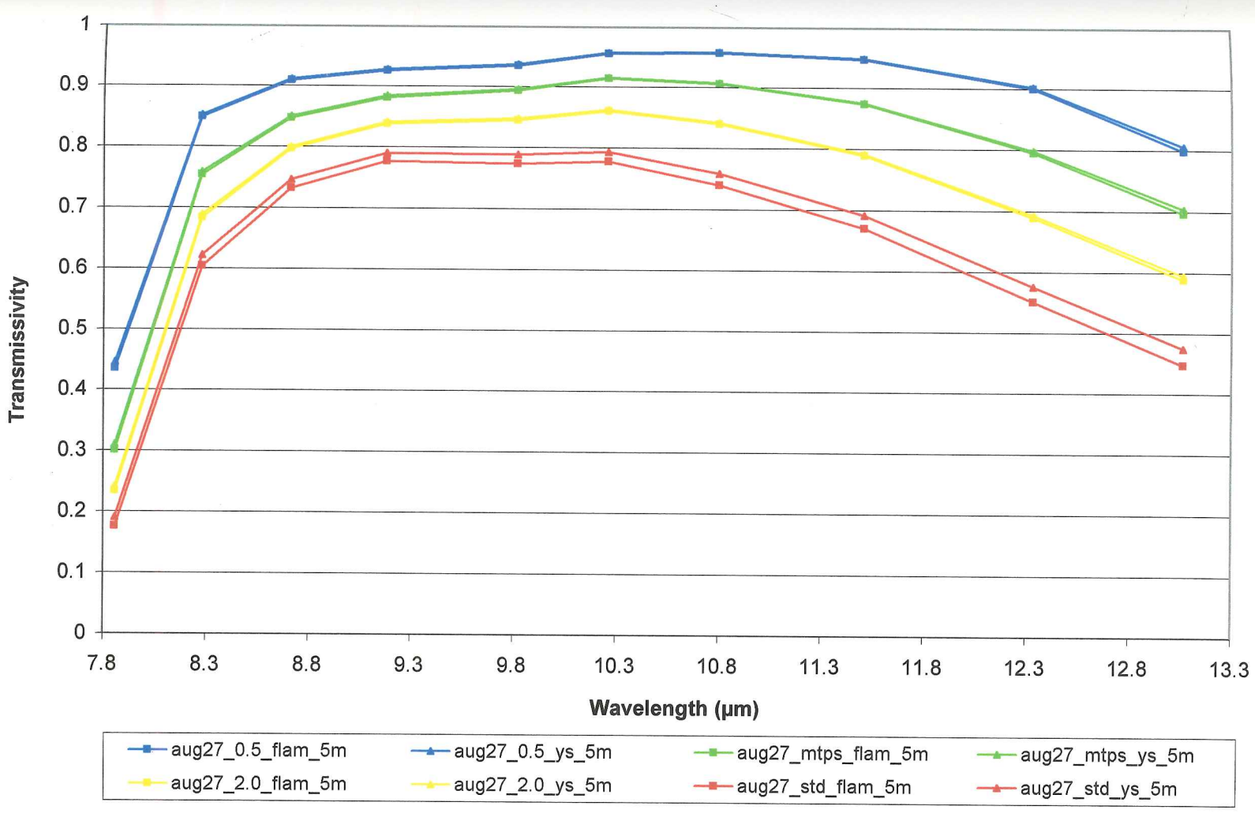

Appendix D. August 27, 2001 - 5m MASTER Transmissivity

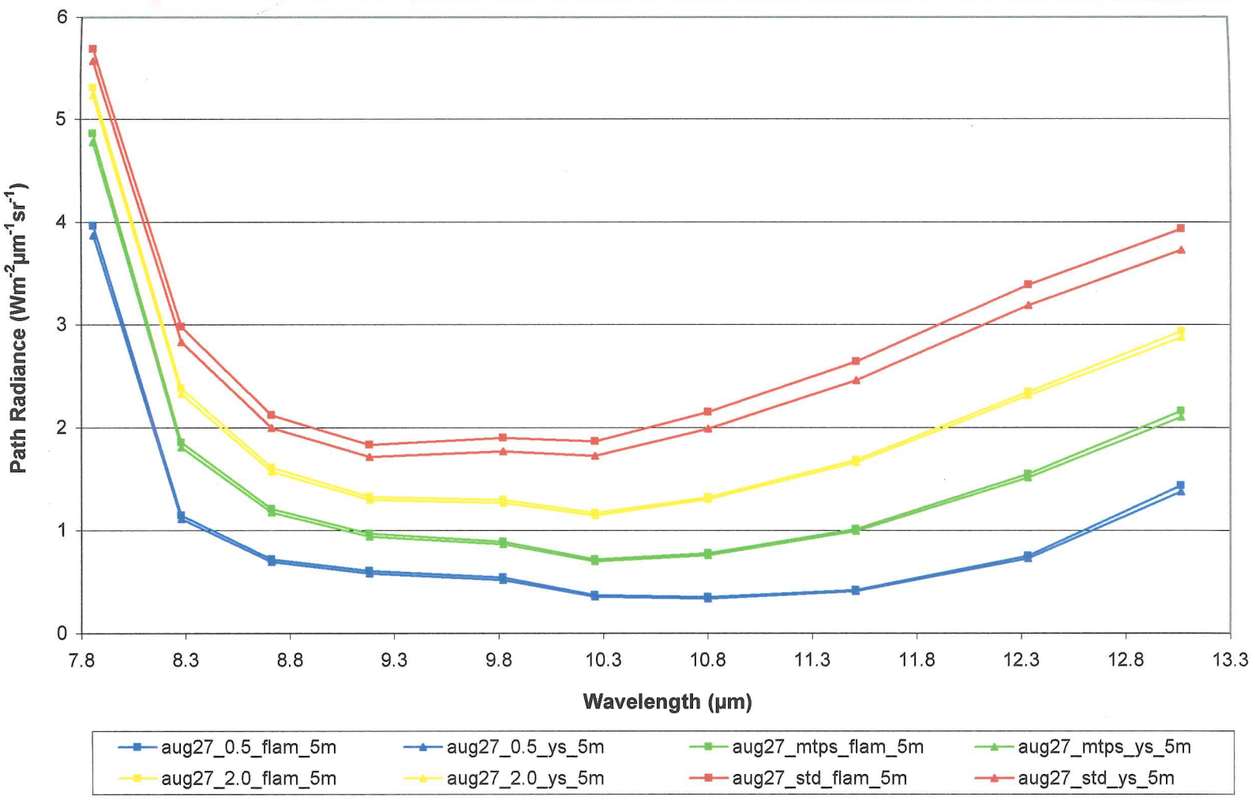

Appendix D. August 27 - 5m MASTER Path Radiance

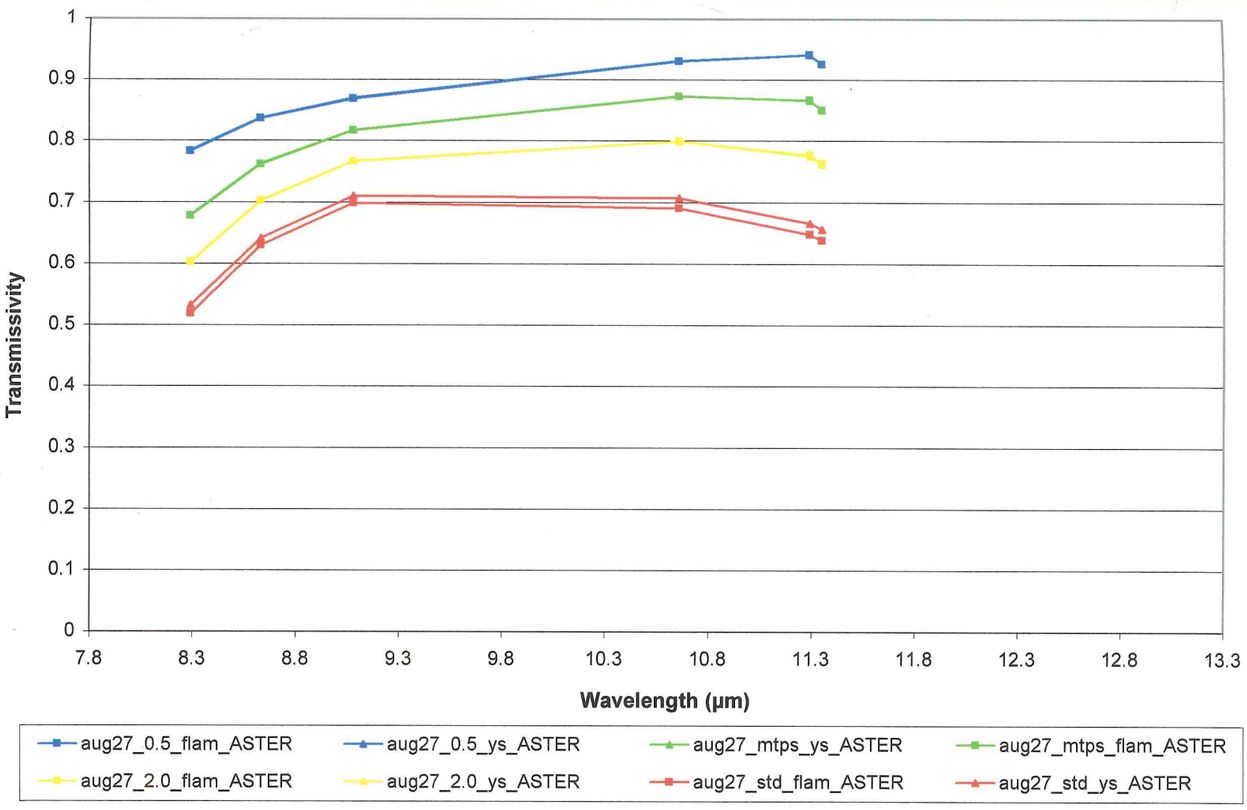

Appendix D. August 27, 2001 - ASTER/Landsat Transmissivity

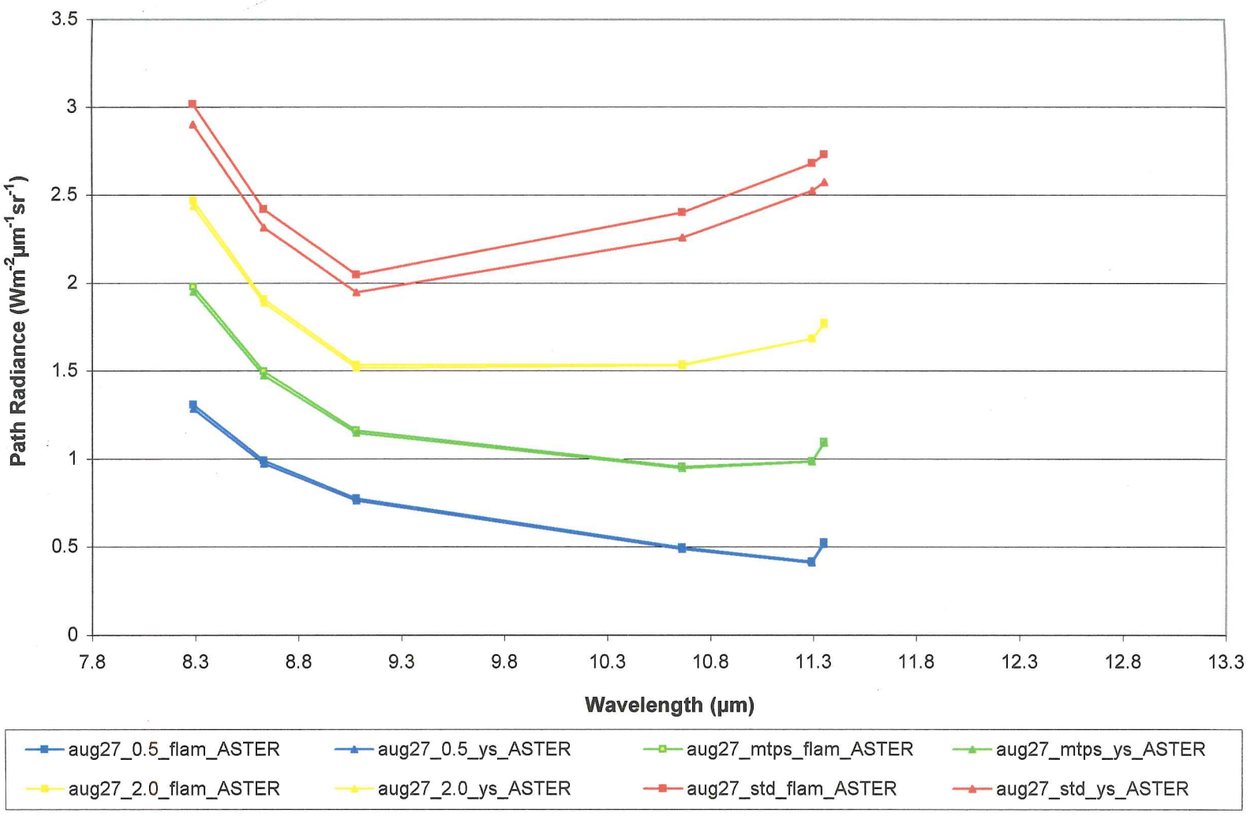

Appendix D. August 27, 2001 - ASTER/Landsat Path Radiance

Appendix A. MODTRAN Runs for Mt. Rainier

Location: MODTRAN output file names	**Louise Lake** radiosonde_louiselake radiosonde_louiselake_20 radiosonde_louiselake_40	**Paradise** radiosonde_paradise radiosonde_paradise_20 radiosonde_paradise_40	**Panorama Point** radiosonde_panpoint radiosonde_panpoint_20 radiosonde_panpoint_40	**Kautz Glacier** radiosonde_kautz radiosonde_kautz_20 radiosonde_kautz_40
MODTRAN Prompt:	**Input:**			
Calculation Option	MODTRAN	MODTRAN	MODTRAN	MODTRAN
Model Atmosphere	User Specified	User Specified	User Specified	User Specified
Type of Atmospheric Path	Slant Path	Slant Path	Slant Path	Slant Path
Mode of Execution	Radiance w/scattering	Radiance w/scattering	Radiance w/scattering	Radiance w/scattering
Execute with Multiple Scattering	MS on Scattering at Observer	MS on Scattering at Observer	MS on Scattering at Observer	MS on Scattering at Observer
Atmospheric Profiles	aug26_rainier.csv	aug26_rainier.csv	aug26_rainier.csv	aug26_rainier.csv
CO_2 concentration	365 ppm	365 ppm	365 ppm	365 ppm
Total Column Water (g/cm^2)	Use default	Use default	Use default	Use default
Use Instrument Filter File	none	none	none	none
Scattering algorithm	modtran 2	modtran 2	modtran 2	modtran 2
Temperature at First Boundary	0	0	0	0
Surface Albedo Flag	Surface Albedo Value	Surface Albedo Value	Surface Albedo Value	Surface Albedo Value
Surface Albedo	0.02	0.02	0.02	0.02
Atmospheric Parameters - do not scale TOA irradiance File Sun 2				
Aerosol Model Used	Rural - VIS 23km	Rural - VIS 23km	Rural - VIS 23km	Rural - VIS 23km
Seasonal Modification	Spring-Summer	Spring-Summer	Spring-Summer	Spring-Summer
Upper Atmosphere Aerosols	Background Stratospheric	Background Stratospheric	Background Stratospheric	Background Stratospheric
GRNDALTABOVE SEALEVEL	1.4	1.645	2	2.438
Observer Height	9.5	9.5	9.5	9.5
Final Height (km)	1.4	1.645	2	2.438
Zenith Angle	0°, 20°, 40°	0°, 20°, 40°	0°, 20°, 40°	0°, 20°, 40°
Wavelength Coverage	from 0.4 to 13.5 micrometers	from 0.4 to 13.5 micrometers	from 0.4 to 13.5 micrometers	from 0.4 to 13.5 micrometers
default frequency increment	(1 1/cm .00048um)	(1 1/cm .00048um)	(1 1/cm .00048um)	(1 1/cm .00048um)
default FWHM	(1 1/cm - .014411 um)	(1 1/cm - .014411 um)	(1 1/cm - .014411 um)	(1 1/cm - .014411 um)
Solar/Lunar Geometry Type	Option Azimuth and Zenith Angle	Option Azimuth and Zenith Angle	Option Azimuth and Zenith Angle	Option Azimuth and Zenith Angle
Aerosol Phase Function	MIE Generated	MIE Generated	MIE Generated	MIE Generated
Day of year	237	237	237	237
Solar Zenith Angle	37	37	37	37
Azimuth Angle at Observer	-164	-164	-164	-164

Appendix A Cont. MODTRAN Runs for Mt. Rainier

Location	**Camp Muir**	**Sunset Ampitheater**	**Summit**
MODTRAN output file names	radiosonde_muir radiosonde_muir_20 radiosonde_muir_40	radiosonde_sunsetamp radiosonde_sunsetamp_20 radiosonde_sunsetamp_40	radiosonde_summit radiosonde_summit_20 radiosonde_summit_40
MODTRAN Prompt:	**Input:**		
Calculation Option	MODTRAN	MODTRAN	MODTRAN
Model Atmosphere	User Specified	User Specified	User Specified
Type of Atmospheric Path	Slant Path	Slant Path	Slant Path
Mode of Execution	Radiance w/scattering	Radiance w/scattering	Radiance w/scattering
Execute with Multiple Scattering	MS on Scattering at Observer	MS on Scattering at Observer	MS on Scattering at Observer
Atmospheric Profiles	aug26_rainier.csv	aug26_rainier.csv	aug26_rainier.csv
CO_2 concentration	365 ppm	365 ppm	365 ppm
Total Column Water (g/cm^2)	Use default	Use default	Use default
Use Instrument Filter File	none	none	none
Scattering algorithm	modtran 2	modtran 2	modtran 2
Temperature at First Boundary	0	0	0
Surface Albedo Flag	Surface Albedo Value	Surface Albedo Value	Surface Albedo Value
Surface Albedo	0.02	0.02	0.02
Atmospheric Parameters - do not scale TOA irradiance File Sun 2			
Aerosol Model Used	Rural - VIS 23km	Rural - VIS 23km	Rural - VIS 23km
Seasonal Modification	Spring-Summer	Spring-Summer	Spring-Summer
Upper Atmosphere Aerosols	Background Stratospheric	Background Stratospheric	Background Stratospheric
GRNDALTABOVE SEALEVEL	3.105	3.72	4.393
Observer Height	9.5	9.5	9.5
Final Height (km)	3.105	3.72	4.393
Zenith Angle	0°, 20°, 40°	0°, 20°, 40°	0°, 20°, 40°
Wavelength Coverage	from 0.4 to 13.5 micrometers	from 0.4 to 13.5 micrometers	from 0.4 to 13.5 micrometers
default frequency increment	(1 1/cm .00048um)	(1 1/cm .00048um)	(1 1/cm .00048um)
default FWHM	(1 1/cm - .014411 um)	(1 1/cm - .014411 um)	(1 1/cm - .014411 um)
Solar/Lunar Geometry Type	Option Azimuth and Zenith Angle	Option Azimuth and Zenith Angle	Option Azimuth and Zenith Angle
Aerosol Phase Function	MIE Generated	MIE Generated	MIE Generated
Day of year	237	237	237
Solar Zenith Angle	37	37	37
Azimuth Angle at Observer	-164	-164	-164

MODTRAN OUTPUT

Path Thermal Radiance ($Wm^{-2}sr^{-1}(cm^{-1})^{-1}$)
radiance emitted by the path constituents (atmospheric gases, as well as aerosols) that is seen at the observer

Total Transmissivity
total path transmission from the observer to the start of the path

Appendix B. MODTRAN Runs for August 11, 2001 TIR Data (ASTER/Landsat 7)

MODTRAN output name	aug11_0.5_flam	aug11_0.75_flam	aug11_mtps_flam	aug11_2.0_flam	aug11_std_flam
MODTRAN OPTION:					
Calculation Option	MODTRAN	MODTRAN	MODTRAN	MODTRAN	MODTRAN
Model Atmosphere	Mid-Latitude Summer	Mid-Latitude Summer	Mid-Latitude Summer	Mid-Latitude Summer	Mid-Latitude Summer
Type of Atmospheric Path	Slant Path	Slant Path	Slant Path	Slant Path	Slant Path
Mode of Execution	Radiance w/scattering	Radiance w/scattering	Radiance w/scattering	Radiance w/scattering	Radiance w/scattering
Execute with Multiple Scattering	MS on Scattering at Observer	MS on Scattering at Observer	MS on Scattering at Observer	MS on Scattering at Observer	MS on Scattering at Observer
Atmospheric Profiles	Default to Model	Default to Model	Default to Model	Default to Model	Default to Model
WaterVapor Column Choices	0.5 - gm/cm^2	1 - gm/cm^2	1.08 gm/cm^2- microtops	2 - gm/cm^2	Use Default water vapor column
Ozone default ozone column	Use Default ozone column	Use Default ozone column	Use Default ozone column	Use Default ozone column	Use Default ozone column
Use Instrument Filter File	none	none	none	none	none
Carbon Dioxide	365	365	365	365	365
Scattering Algorithm	Modtran 2	Modtran 2	Modtran 2	Modtran 2	Modtran 2
Temperature at First Boundary	293	293	293	293	293
Surface Albedo Flag	Surface Albedo Value	Surface Albedo Value	Surface Albedo Value	Surface Albedo Value	Surface Albedo Value
Surface Albedo	0	0	0	0	0
Solar Irradiance Source	File Sun 2	File Sun 2	File Sun 2	File Sun 2	File Sun 2
Top of Atmopshere Parameters	Do not scale TOA irradiance	Do not scale TOA irradiance	Do not scale TOA irradiance	Do not scale TOA irradiance	Do not scale TOA irradiance
Triangular Filter Width	5	5	5	5	5
Aerosol Model Used	Rural - VIS 23km	Rural - VIS 23km	Rural - VIS 23km	Rural - VIS 23km	Rural - VIS 23km
Seasonal Modification to Aerosol	Spring-Summer	Spring-Summer	Spring-Summer	Spring-Summer	Spring-Summer
Upper Atmosphere Aerosols	Background Stratospheric	Background Stratospheric	Background Stratospheric	Background Stratospheric	Background Stratospheric
Surface Range for Boundar Layer	0	0	0	0	0
GNDALT (Alititude above sea level)	0.056	0.056	0.056	0.056	0.056
all rest default					
Path Type: Observer, Zenith < and Final					
Observer Height (km) - detector	0	0	0	0	100
Final Height (km) - surface elevation	0.056	0.056	0.056	0.056	0.056
Zenith Angle - Note: 180=nadir	180	180	180	180	180
Wavelength Coverage	from 0.4 to 13.5 micrometers	from 0.4 to 13.5 micrometers	from 0.4 to 13.5 micrometers	from 0.4 to 13.5 micrometers	from 0.4 to 13.5 micrometers
default frequency increment	(1 1/cm .00048um)	(1 1/cm .00048um)	(1 1/cm .00048um)	(1 1/cm .00048um)	(1 1/cm .00048um)
default FWHM	(1 1/cm - .014411 um)	(1 1/cm - .014411 um)	(1 1/cm - .014411 um)	(1 1/cm - .014411 um)	(1 1/cm - .014411 um)
S/L Geometry Type:					
Aerosol Phase Function	MIE Generated	MIE Generated	MIE Generated	MIE Generated	MIE Generated
Day of year	222	222	222	222	222
Azimuth Angle at Observer (UTC 21)	175.82	175.82	175.82	175.82	175.82
Solar Zenith Angle (UTC 21)	32.27	32.27	32.27	32.27	32.27

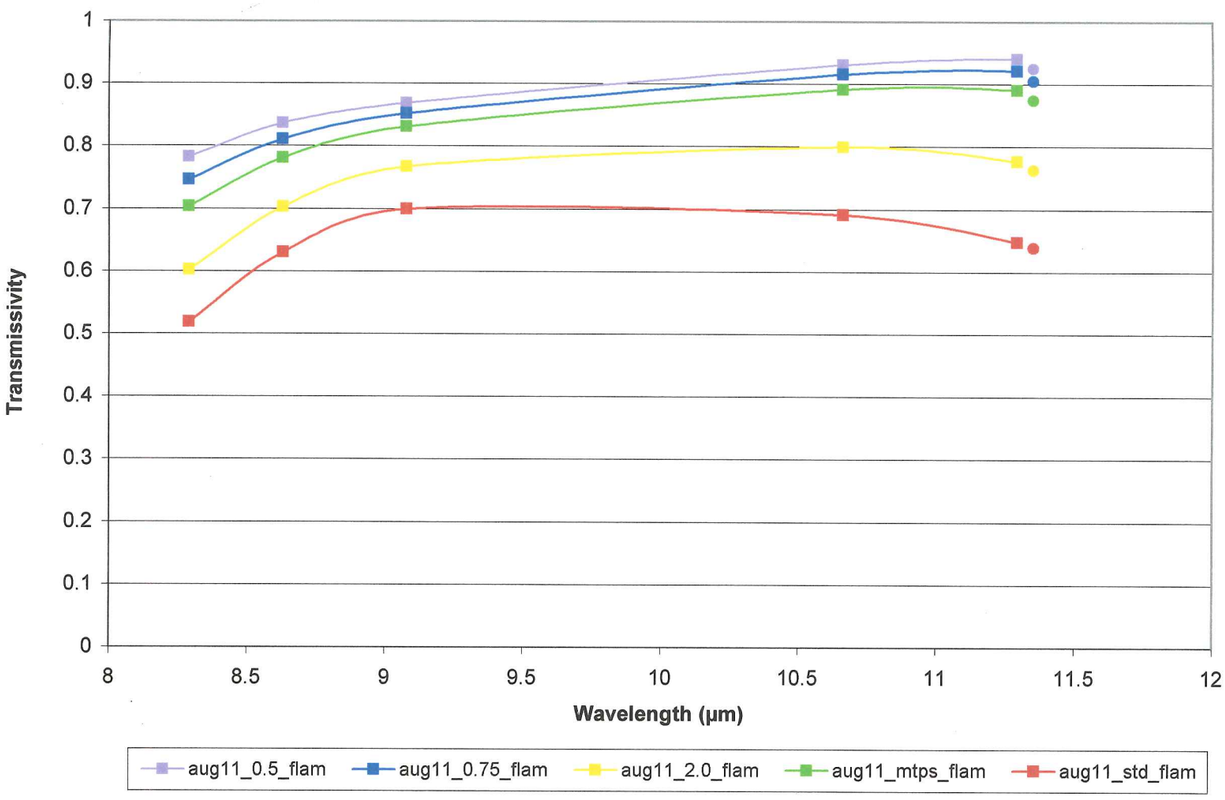

Appendix B. August 11, 2001 ASTER/Landsat 7 Transmissivity

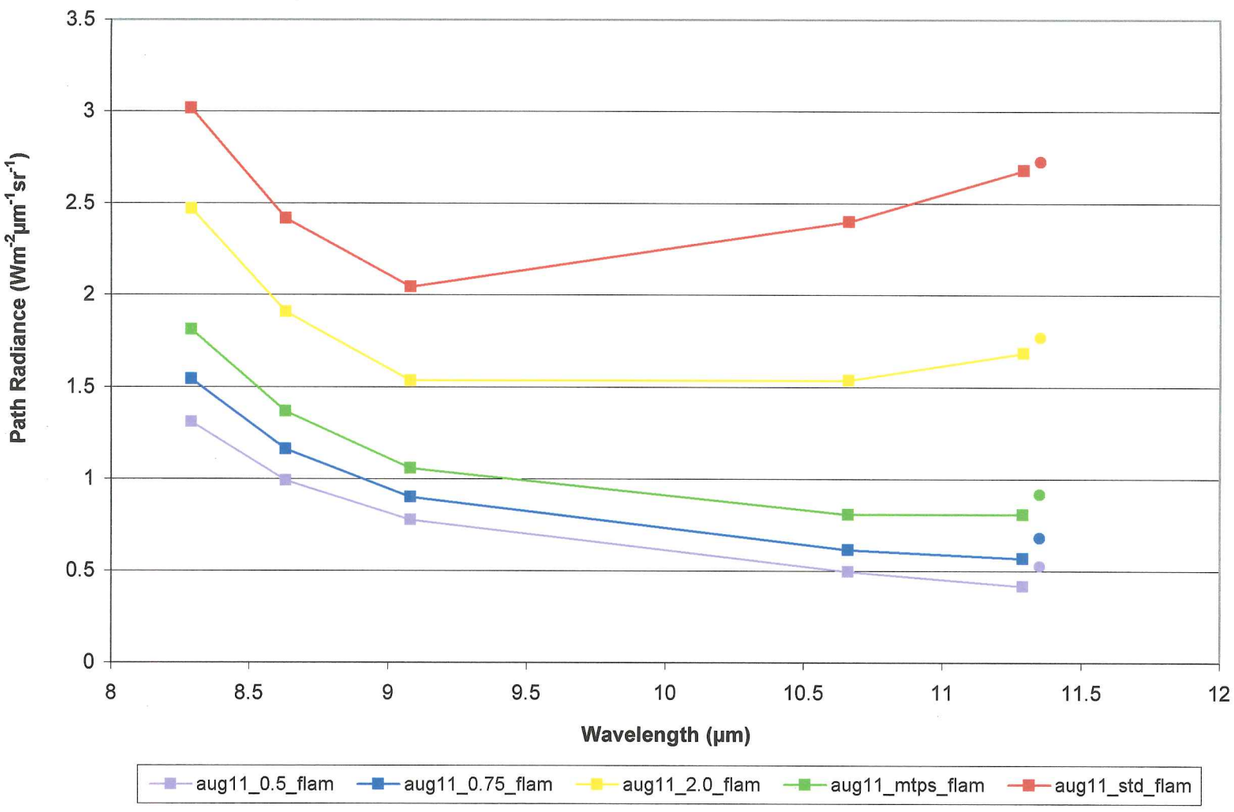

Appendix B. August 11, 2001 ASTER/Landsat 7 Path Radiance

Appendix C. MODTRAN runs for MASTER August 25, 2001 data

MODTRAN output name (plus 6m or 15m)	**aug25_0.6_flam** **aug25_0.6_ys**	**aug25_mtps_flam** **aug25_mtps_ys**	**aug25_2.0_flam** **aug25_2.0_ys**	**aug25_mm5_flam** **aug25_mm5_ys**	**aug25_std_flam** **aug25_std_ys**
MODTRAN OPTION:					
Calculation Option	MODTRAN	MODTRAN	MODTRAN	MODTRAN	MODTRAN
Model Atmosphere	Mid-Latitude Summer	Mid-Latitude Summer	Mid-Latitude Summer	Mid-Latitude Summer	Mid-Latitude Summer
Type of Atmospheric Path	Slant Path	Slant Path	Slant Path	Slant Path	Slant Path
Mode of Execution	Radiance w/scattering	Radiance w/scattering	Radiance w/scattering	Radiance w/scattering	Radiance w/scattering
Execute with Multiple Scattering	MS on Scattering at Observer	MS on Scattering at Observer	MS on Scattering at Observer	MS on Scattering at Observer	MS on Scattering at Observer
Atmospheric Profiles	Default to Model for all profiles	Default to Model for all profiles	Default to Model for all profiles	Default to Model for all profiles	Default to Model for all profiles
WaterVapor Column Choices	0.5 - gm/cm^2	1.2 gm/cm^2- microtops	2 - gm/cm^2	Default to Model for all profiles	Use Default water vapor column
Ozone default ozone column	Use Default ozone column	Use Default ozone column	Use Default ozone column	Use Default ozone column	Use Default ozone column
Use Instrument Filter File	none	none	none	aug25_greenmm5.csv	none
Carbon Dioxide	365	365	365	365	365
Scattering Algorithm	Scattering algorithm - modtran 2	Scattering algorithm - modtran 2	Scattering algorithm - modtran 2	Scattering algorithm - modtran 2	Scattering algorithm - modtran 2
Temperature at First Boundary	296	296	296	296	296
Surface Albedo Flag	Surface Albedo Value	Surface Albedo Value	Surface Albedo Value	Surface Albedo Value	Surface Albedo Value
Surface Albedo	0	0	0.02	0.02	0
Solar Irradiance Source	File Sun 2	File Sun 2	File Sun 2	File Sun 2	File Sun 2
Top of Atmopshere Parameters	Do not scale TOA irradiance	Do not scale TOA irradiance	Do not scale TOA irradiance	Do not scale TOA irradiance	Do not scale TOA irradiance
Triangular Filter Width	5	5	5	5	5
Aerosol Model Used	Rural - VIS 23km	Rural - VIS 23km	Rural - VIS 23km	Rural - VIS 23km	Rural - VIS 23km
Seasonal Modification to Aerosol	Spring-Summer	Spring-Summer	Spring-Summer	Spring-Summer	Spring-Summer
Upper Atmosphere Aerosols	Background Stratospheric	Background Stratospheric	Background Stratospheric	Background Stratospheric	Background Stratospheric
Surface Range for Boundar Layer	0	0	0	0	0
GNDALT (Alitltude above sea level)	0.1524 OR 0.056	0.1524 or 0.056	0.1524 or 0.056	0.1524 or 0.056	0.1524 or 0.056
all rest default					
Path Type: Observer, Zenith < and Final					
Observer Height (km) - detector	1.98 OR 6.331	1.98 OR 6.329	1.98 OR 6.333	1.98 OR 6.330	1.98 OR 6.328
Final Height (km) - surface elevation	0.1524 OR 0.059	0.1524 OR 0.057	0.1524 OR 0.061	0.1524 OR 0.058	0.1524 OR 0.056
Zenith Angle - Note: 180=nadir	160	180	180	180	180
Wavelength Coverage	from 0.4 to 13.5 micrometers	from 0.4 to 13.5 micrometers	from 0.4 to 13.5 micrometers	from 0.4 to 13.5 micrometers	from 0.4 to 13.5 micrometers
default frequency increment	(1 1/cm .00048um)	(1 1/cm .00048um)	(1 1/cm .00048um)	(1 1/cm .00048um)	(1 1/cm .00048um)
default FWHM	(1 1/cm - .014411 um)	(1 1/cm - .014411 um)	(1 1/cm - .014411 um)	(1 1/cm - .014411 um)	(1 1/cm - .014411 um)
S/L Geometry Type:	Option Azimuth and Zenith Angle	Option Azimuth and Zenith Angle	Option Azimuth and Zenith Angle	Option Azimuth and Zenith Angle	Option Azimuth and Zenith Angle
Aerosol Phase Function	MIE Generated	MIE Generated	MIE Generated	MIE Generated	MIE Generated
Day of year	234	234	234	234	234
Azimuth Angle at Observer (UTC 21)	-158.4	-158.4	-158.4	-158.4	-158.4
Solar Zenith Angle (UTC 21)	38.5	38.5	38.5	38.5	38.5

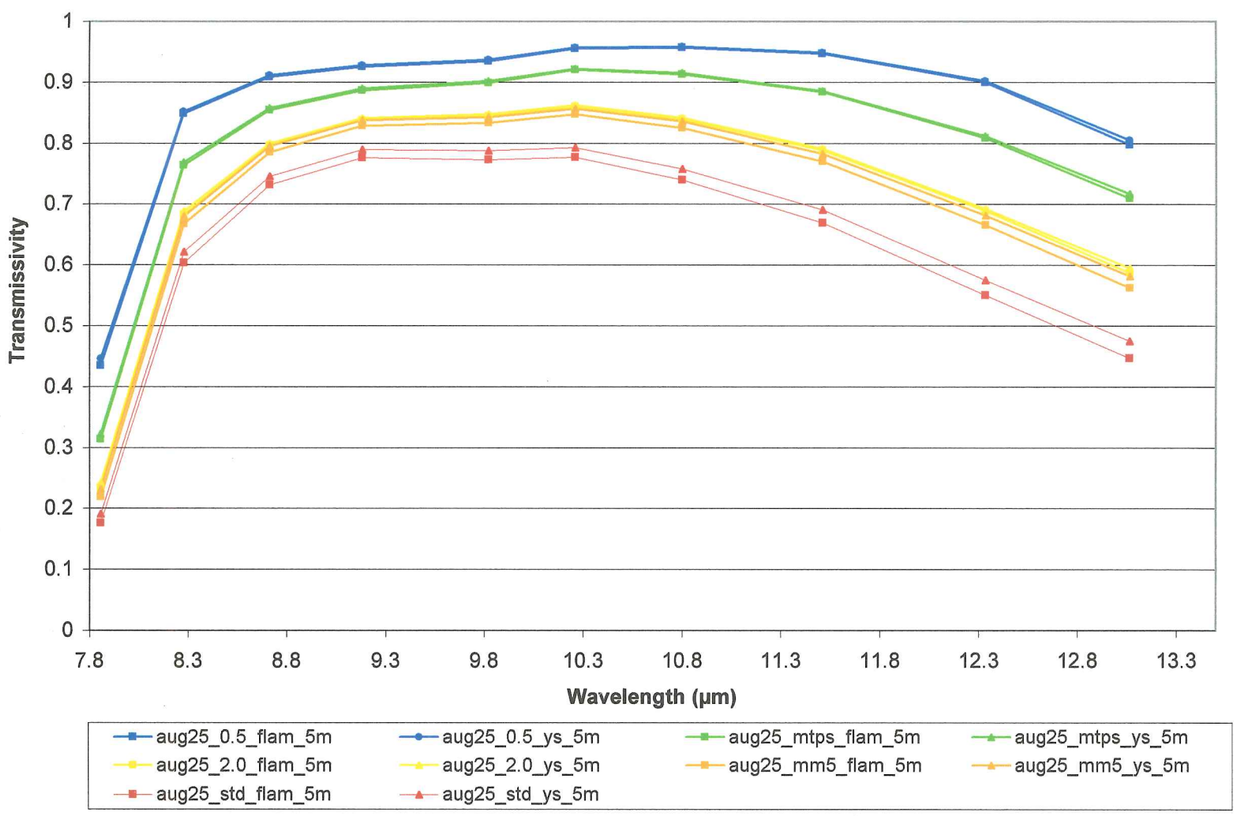

Appendix C. August 25, 2001 - 5m MASTER Transmissivity

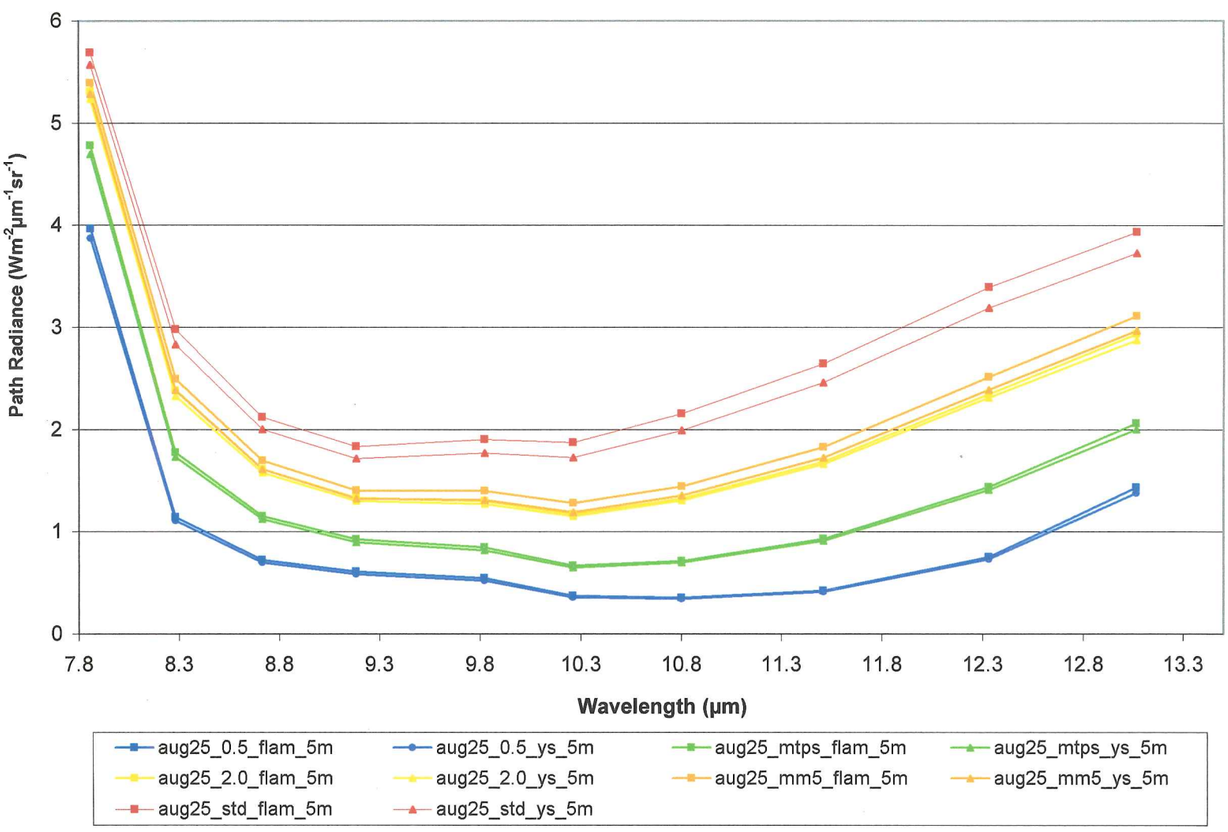

Appendix C. August 25, 2001 - 5m MASTER Path Radiance

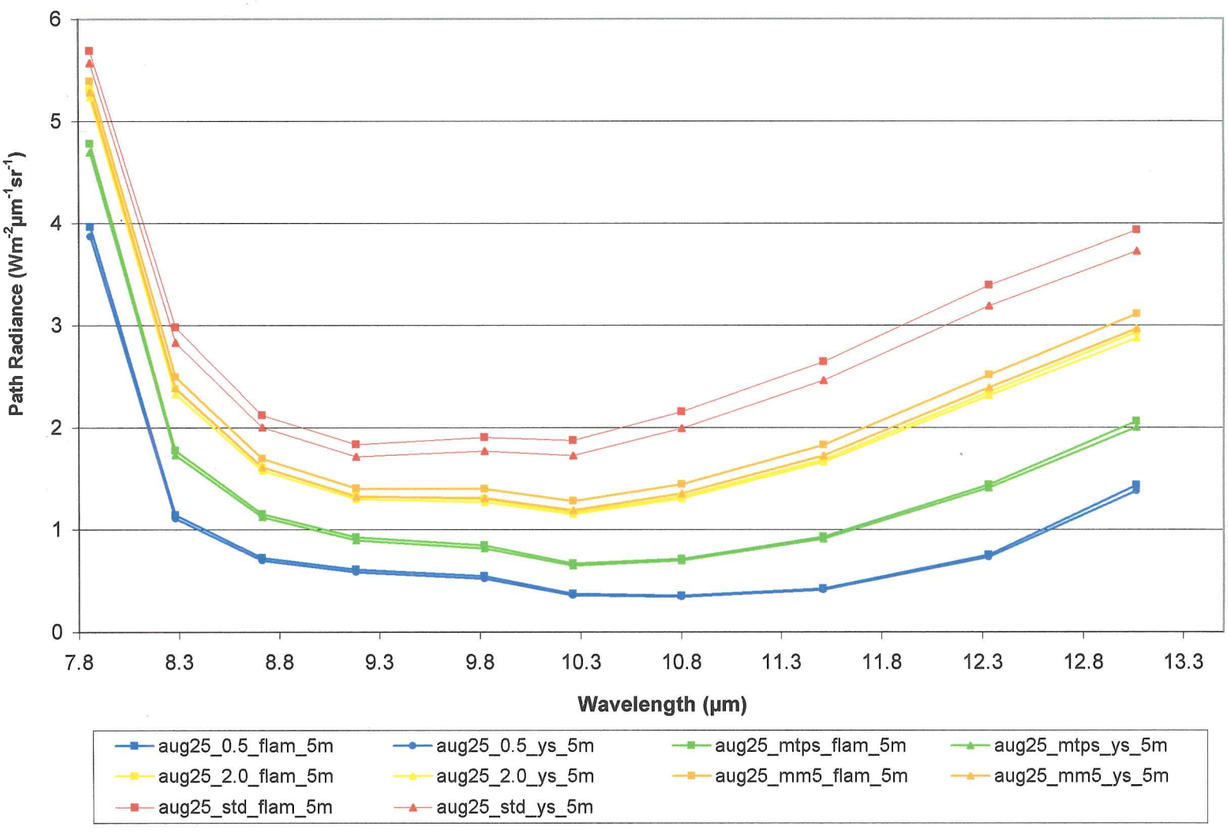

Appendix C. August 25, 2001 - 5m MASTER Path Radiance

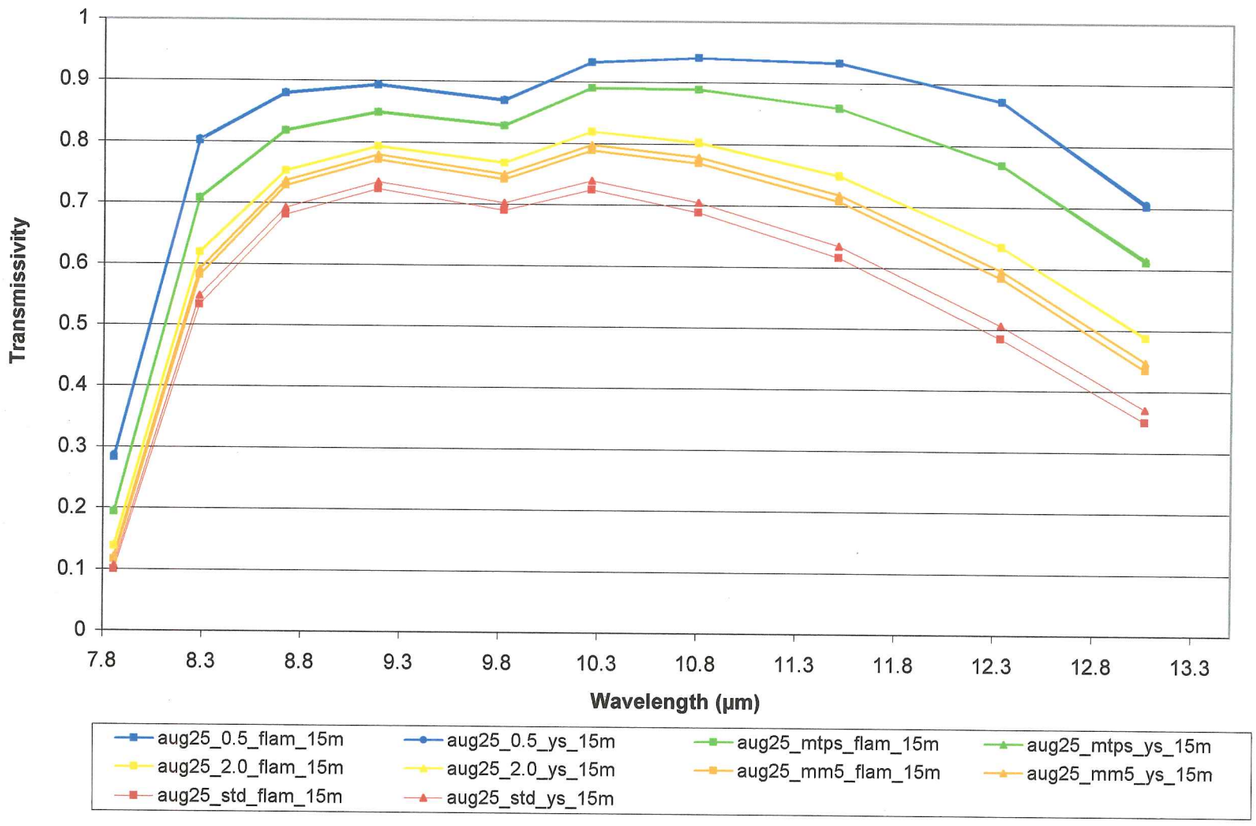

Appendix C. August 25, 2001 - 15m MASTER Transmissivity

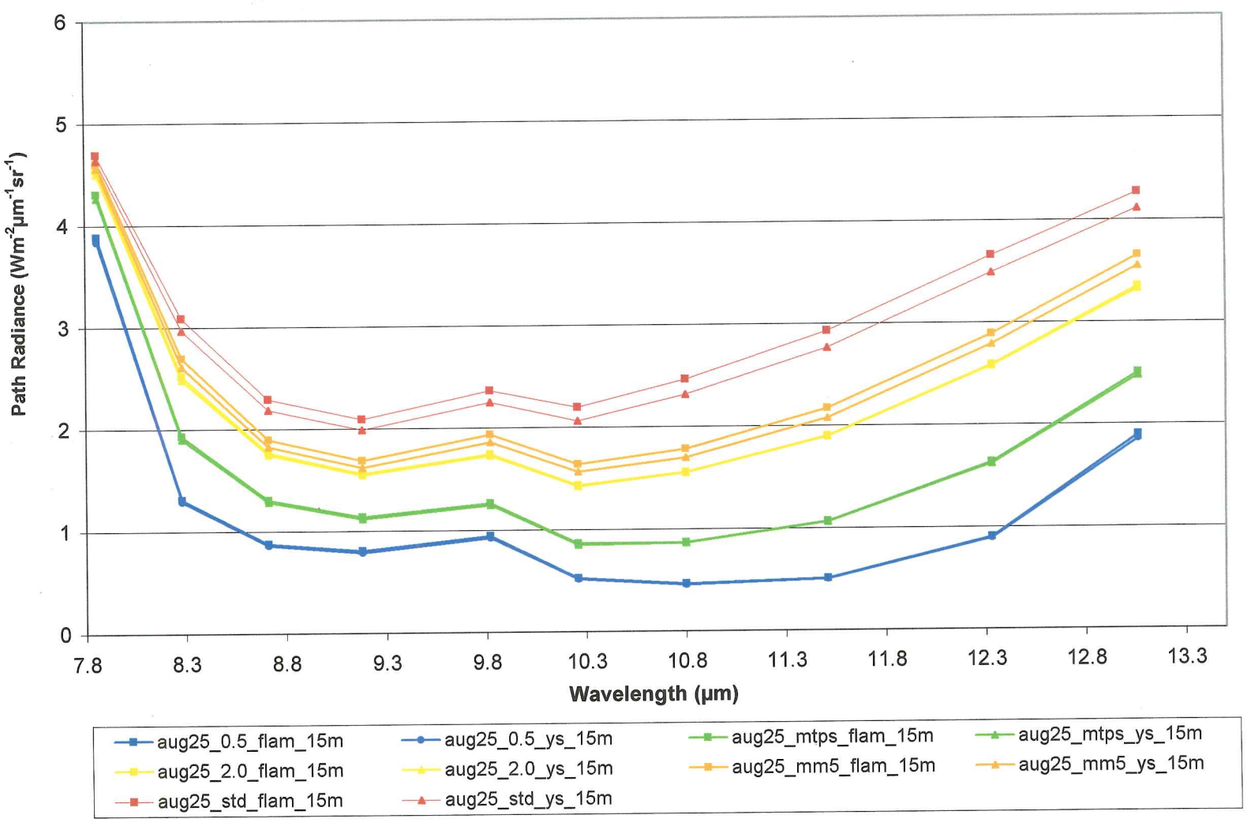

Appendix C. August 25, 2001 - 15m MASTER Path Radiance

Appendix D. MODTRAN runs for MASTER August 27, 2001 data

MODTRAN output name (_5m or _ASTER)	**aug27_0.5_ys aug27_0.5_flam**	**aug27_mtps_ys aug27_mtps_flam**	**aug27_2.0_ys aug27_2.0_flam**	**aug27_std_ys aug27_std_flam**
MODTRAN OPTION:				
Calculation Option	MODTRAN	MODTRAN	MODTRAN	MODTRAN
Model Atmosphere	Mid-Latitude Summer	Mid-Latitude Summer	Mid-Latitude Summer	Mid-Latitude Summer
Type of Atmospheric Path	Slant Path	Slant Path	Slant Path	Slant Path
Mode of Execution	Radiance w/scattering	Radiance w/scattering	Radiance w/scattering	Radiance w/scattering
Execute with Multiple Scattering	MS on Scattering at Observer	MS on Scattering at Observer	MS on Scattering at Observer	MS on Scattering at Observer
Atmospheric Profiles	Default to Model for all profiles	Default to Model for all profiles	Default to Model for all profiles	Default to Model for all profiles
WaterVapor Column Choices	0.5 - gm/cm^2	1.3 gm/cm^2- microtops	2 - gm/cm^2	Use Default water vapor column
Ozone default ozone column	Use Default ozone column	Use Default ozone column	Use Default ozone column	Use Default ozone column
Use Instrument Filter File	none	none	none	none
Carbon Dioxide	365	365	365	365
Scattering Algorithm	Scattering algorithm - modtran 2	Scattering algorithm - modtran 2	Scattering algorithm - modtran 2	Scattering algorithm - modtran 2
Temperature at First Boundary	293	293	293	293
Surface Albedo Flag	Surface Albedo Value	Surface Albedo Value	Surface Albedo Value	Surface Albedo Value
Surface Albedo	0	0	0.02	0
Solar Irradiance Source	File Sun 2	File Sun 2	File Sun 2	File Sun 2
Top of Atmopshere Parameters	Do not scale TOA irradiance	Do not scale TOA irradiance	Do not scale TOA irradiance	Do not scale TOA irradiance
Triangular Filter Width	5	5	5	5
Aerosol Model Used	Rural - VIS 23km	Rural - VIS 23km	Rural - VIS 23km	Rural - VIS 23km
Seasonal Modification to Aerosol	Spring-Summer	Spring-Summer	Spring-Summer	Spring-Summer
Upper Atmosphere Aerosols	Background Stratospheric	Background Stratospheric	Background Stratospheric	Background Stratospheric
Surface Range for Boundar Layer	0	0	0	0
GNDALT (Alititude above sea level)	0.056	0.056	0.056	0.056 or 0.1524
all rest default				
Path Type: Observer, Zenith < and Final				
Observer Height (km) - detector	1.98 OR 100	1.98 OR 100	1.98 OR 100	1.98 OR 100
Final Height (km) - surface elevation	0.056	0.056	0.056	0.056
Zenith Angle - Note: 180=nadir	160	180	180	180
Wavelength Coverage	from 0.4 to 13.5 micrometers	from 0.4 to 13.5 micrometers	from 0.4 to 13.5 micrometers	from 0.4 to 13.5 micrometers
default frequency increment	(1 1/cm .00048um)	(1 1/cm .00048um)	(1 1/cm .00048um)	(1 1/cm .00048um)
default FWHM	(1 1/cm - .014411 um)	(1 1/cm - .014411 um)	(1 1/cm - .014411 um)	(1 1/cm - .014411 um)
S/L Geometry Type:	Option Azimuth and Zenith Angle	Option Azimuth and Zenith Angle	Option Azimuth and Zenith Angle	Option Azimuth and Zenith Angle
Aerosol Phase Function	MIE Generated	MIE Generated	MIE Generated	MIE Generated
Day of year	236	236	236	236
Azimuth Angle at Observer (UTC 21)	177.75	177.75	177.75	177.75
Solar Zenith Angle (UTC 21)	37.46	37.46	37.46	37.46

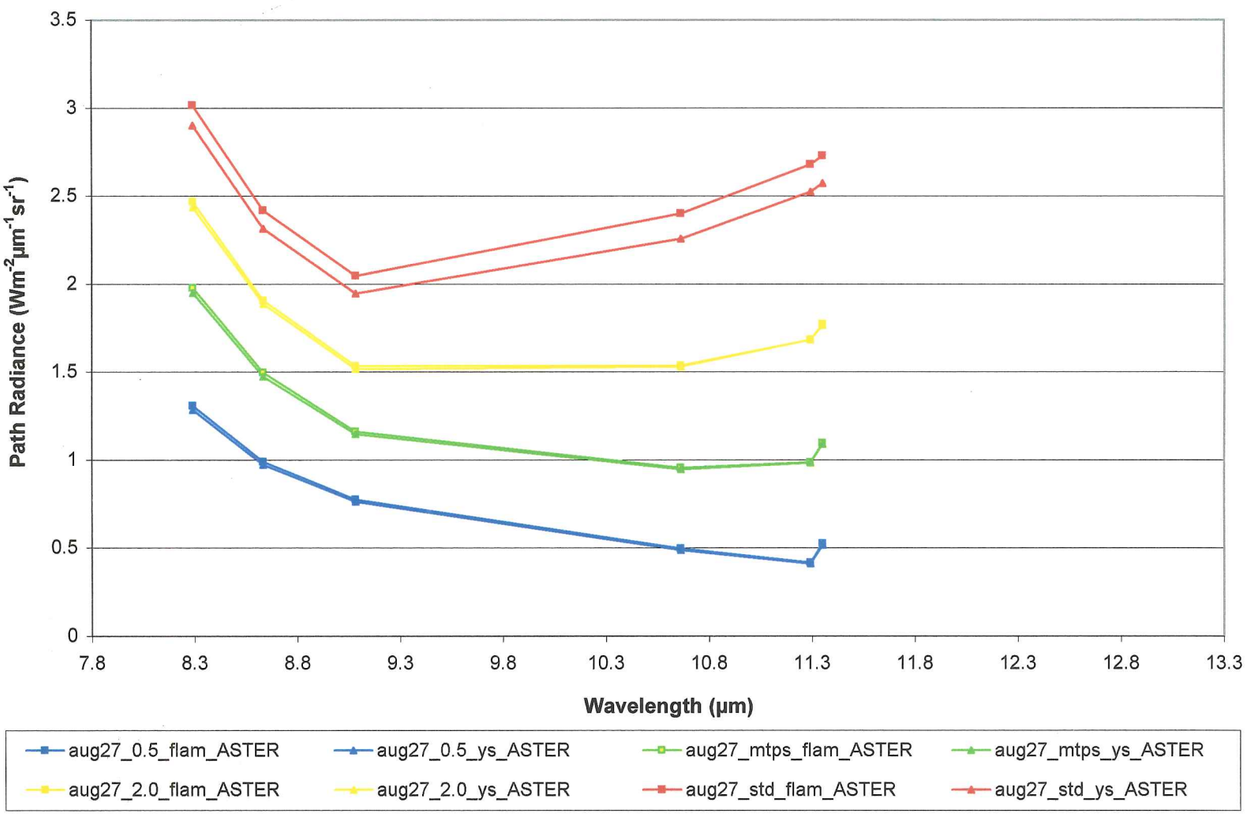

Appendix D. August 27, 2001 - ASTER/Landsat Path Radiance

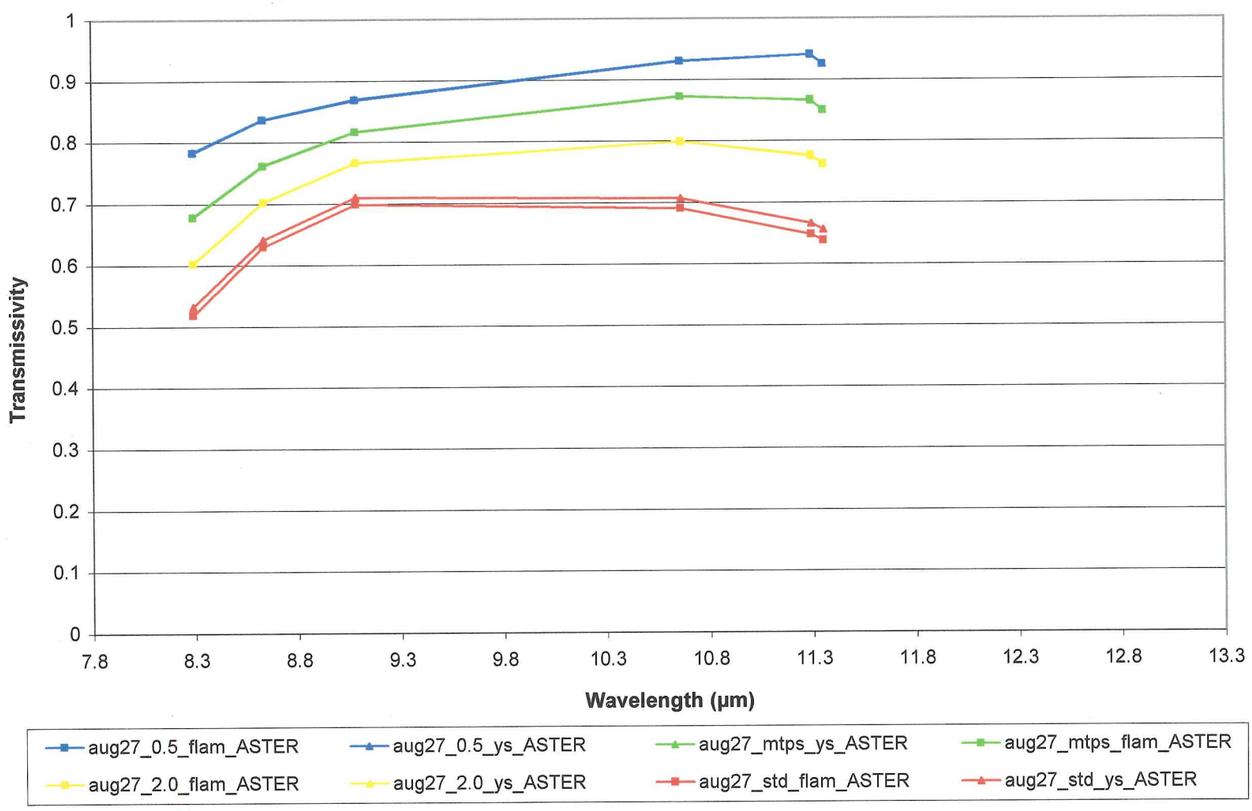

Appendix D. August 27, 2001 - ASTER/Landsat Transmissivity

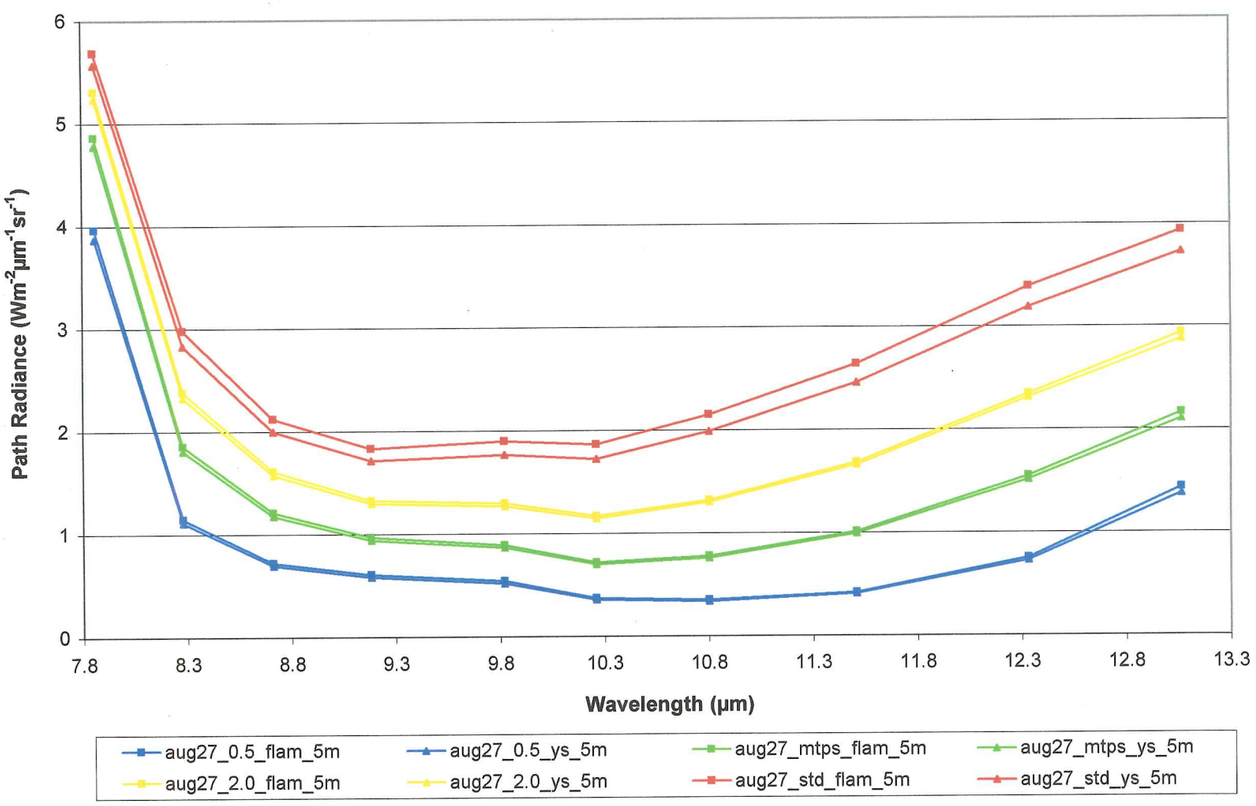

Appendix D. August 27 - 5m MASTER Path Radiance

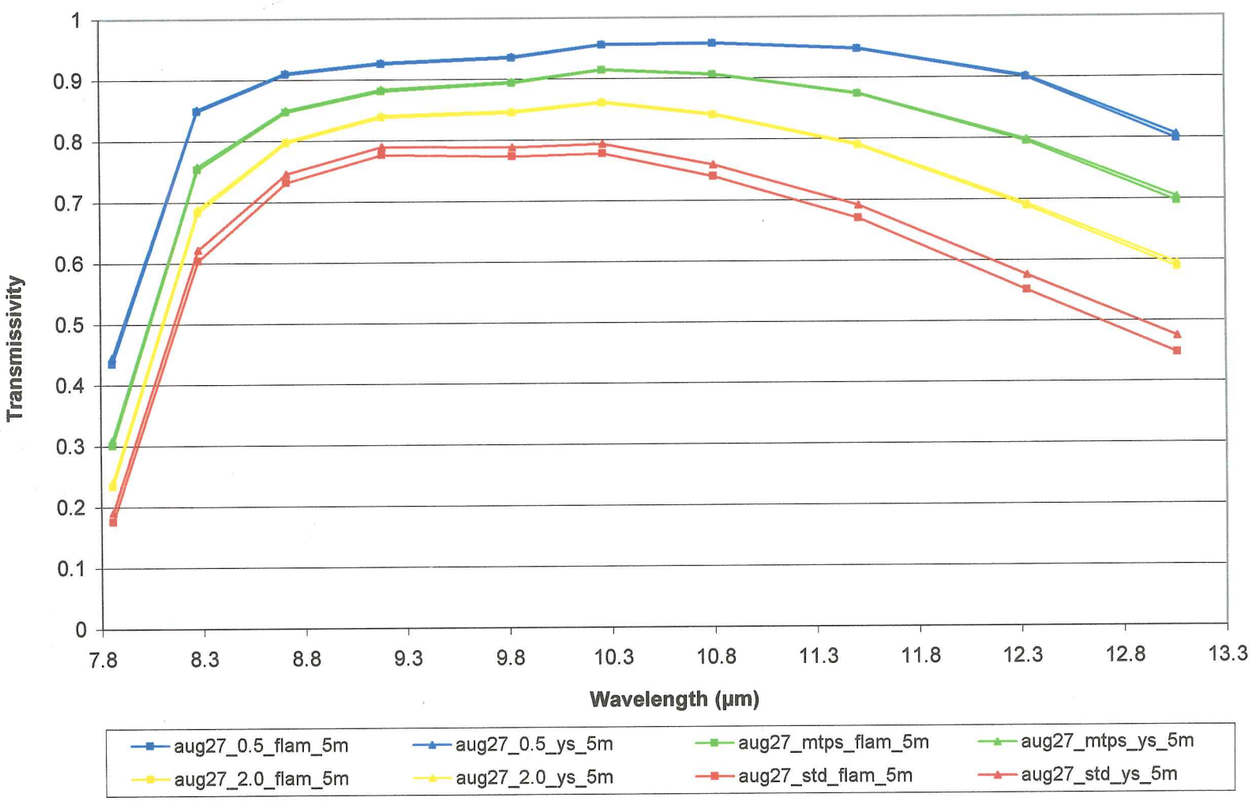

Appendix D. August 27, 2001 - 5m MASTER Transmissivity